UNIVERSITY OF CALIFORNIA SAN DIEGO

Parametric Process on Silicon Microchip Mixer

A dissertation submitted in partial satisfaction of
the requirements for the degree Doctor of Philosophy
in

Electrical Engineering (Photonics)

by

Motohiko Eto

Committee in charge:

Professor Stojan Radic, Chair
Professor Leonid Butov
Professor Miroslav Kristic
Professor Yu-Hwa Lo
Professor George C. Papen

2021

The Dissertation of Motohiko Eto is approved, and it is acceptable in quality and form for publication on microfilm and electronically.

University of California San Diego

2021

DEDICATION

To my family for their support

TABLE OF CONTENTS

DISSERTATION APPROVAL PAGE……. iii

DEDICATION……iv

TABLE OF CONTENTS……..……. v

LIST OF FIGURES…….…….……. ix

LIST OF TABLES…….……..….... xiii

LIST OF ABBREVIATIONS…… xiv

ACKNOWLEDGEMENTS…….…….…….. xvi

VITA……...……...…… xviii

ABSTRACT OF THE DISSERTATION……...……...……...…xix

Chapter 1 Introduction ……...……..…1

1.1 Motivation ……..……...… 1
1.2 Dissertation overview……..……. 3

Chapter 2 Parametric process and device characterization for silicon mixer …… 5

2.1 Nonlinear effects in dielectric medium …… 5

2.1.1 Four wave mixing ……. 6

2.1.2 Chromatic dispersion …… 8

2.1.3 Two photon absorption (TPA) …….. 9

2.1.4 Nonlinear parameters …….. 10

2.2 Micro ring mixer mechanics …….. 11

2.2.1 Nonlinear Schrödinger equation ……. 11

2.2.2 Transmission and phase matching …….. 12

2.2.3 Coupling in a ring ……...… 13

2.2.4 Q factor and finesse ……...…. 15

Chapter 3 Mixer characterization and design for comb generation ……. 18

3.1 Device characterization …….…..… 18

3.1.1 Dispersion engineering ……...… 19

3.1.2 Length of ring ……. 21
3.1.3 Coupling ratio ……. 24
3.1.4 PIN structure ……..…..... 25
3.1.5 Avoid additional loss from PIN structure ……...…… 28
3.2 Comb simulation ……...…….... 32
3.2.1 Simulation procedure …….. 33
3.2.2 Multiple tone pump ……. 34
3.3 Design review and fabrication ……...…… 35
3.3.1 Design review ……..... 36
3.3.2 Layout generation ……...…… 37
3.3.3 Fabrication process…….. 38
3.4. Device performances ……...…. 40
3.4.1 Overview ……..… 40
3.4.2 Waveguide loss ……41
3.4.3 Coupling ratio ……..… 43
3.4.4 FSR ……..……...… 46
3.4.5 Q factor ..……..……...… 46
3.5 Chapter summary ……..…. 49
Chapter 4 Frequency comb generation in silicon ring mixer ……...… 50
4.1 Introduction……...….. 50
4.2 Principle of comb generation with multiple tone pump with silicon ring mixer. ……... 51
4.3 Setup and procedure ……...…… 54

4.3.1 Setup ……...…… 55

4.3.2 Procedure …….……...…… 56

4.4 Experimental demonstration: Single pump ……..... 57

4.5 Experimental demonstration: Two pump ……...…… 59

4.6 Experimental demonstration: Multiple pump ……..... 60

4.6 Chapter summary ……...……..... 66

Chapter 5 Dispersion dependence of comb generation ……..... 67

5.1 Introduction ……..... 67

5.2 Theory and implementation ……...……...…. 68

5.3 Experimental procedures and post-processing ……... 69

5.4 Dispersion measurement for SMF-28 ……..... 71

5.4.1 Interference measurement ……...…… 71

5.4.2 Conversion from time-domain to frequency-domain ……. 73

5.4.3 Dispersion calculation ……. 75

5.5 Dispersion measurement for silicon waveguide ……..... 75

5.6 Dispersion dependence for comb generation ……. 77

5.7 Chapter summary ……...……..... 80

Chapter 6 Low-Noise frequency comb generation in silicon ring mixer ……. 82

6.1 Introduction …… 82

6.2 FWM from Fiber based comb source ……..... 83

6.2.1. Introduction ……..... 83

6.2.2 Setup ……..……. 83

6.2.3 Experimental results …… 84

6.3 Phase noise ……..87

6.3.1 introduction ……..……...… 87

6.3.2 setup ……...……...….. 87

6.3.3 experiment results ……...… 88

6.4 Chapter summary ……...……..... 90

Chapter 7 Conclusion……..…….. 91

7.1 Dissertation Summary……...…….……. 91

7.2 Future directions ……..…….……. 92

7.2.1 Broad spectrum source: cascaded ring mixer ……. 93

7.2.2 Miniaturizing comb system on a silicon chip ……. 94

Bibliography …… 95

LIST OF FIGURES

Figure 1.1 Global internet traffic growth in 2016-2023…..……..... 1

Figure 2.1 Degenerate Four wave mixing. ……. 7

Figure 2.2 Two tone parametric process based on degenerate FWM. ……...… 8

Figure 2.3 Example of the relationship between dispersions. ……...…… 9

Figure 2.4 Band diagram of two photon absorption. ……...… 10

Figure 2.5 Transmission and coupling in a ring mixer. …...……..... 13

Figure 2.6 Coupling condition and trends. ……...… 15

Figure. 2.7 Trends in Q factor and finesse for ring mixer (a) Q factor (b) Finesse. ...… 17

Figure 3.1 Dispersion of silicon waveguide with variation of width. Waveguide height H is 275nm, slab height h is 55nm, and variation of width W is between 350 and 500nm with 10nm step. ……...……..... 20

Figure 3.2 Example of quasi-single mode waveguide. (a) cross section and modes, (b) dispersion curve, and (c) effective index for each mode. ……...……. 21

Figure 3.3 efficiency of parametric amplification. ……...…...… 22

Figure 3.4 simulation of loaded Q factor and finesse along length of ring (a) Q factor, and (b) finesse along length of the ring. Here, waveguide loss is 1.5dB/cm, and group index (n_g)is set as n_g: 4.1186.……..……...… 23

Figure 3.5 Transmission of the ring with different coupling constant. The variation of the length of rings are (a) 1cm, (b) 2cm, and (c) 3cm. The device parameters are simultaneous as Figure 3.3. Here, waveguide loss is 1.5dB/cm. ……...…… 24

Figure 3.6 Power splitting ratio with different cross section. (a) W = 450nm, and (b) W = 500nm. …..……...… 25

Figure 3.7 Silicon waveguide with reverse bias PIN structure. …...…… 26

Figure 3.8 Relationship between deviation of slab height and carrier lifetime.……..... 28

Figure 3.9 Simulation of optical loss from via against waveguide (a) distance against via D_D shown in (b). (b) cross section of waveguide and via. .....…….. 30

Figure 3.10 Spectrum of comb generation in different cross section to compare effect of chromatic dispersion. D = ~ -200(ps.nm/km) (a) measurement (b) simulation……..…. 32

Figure 3.11 Flowchart of procedure to simulate comb generation. ..……..…… 34

Figure 3.12 Spectrum of comb generation in different cross section to compare effect of chromatic dispersion. (a) W = 460nm, D = -70(ps.nm/km) (b) W -500nm, D = -70 (ps.nm/km). ……...……...…… 35

Figure 3.13 Design review for silicon ring mixer (a) Top view of the device. The expansion is for the optical directional coupler. (b) Cross section at middle of the coupler. ……. 37

Figure 3.14 The illustration of fabrication layer for the MPW process (a) Si layer fabrication, and (b) Full stack of layer. ……..... 39

Figure 3.15 Example of fabricated silicon ring mixer. (a) Top view (b) Crosse section of the optical coupler. ...……..……..…… 40

Figure 3.16 Total loss for the waveguide between different lots. …...……..… 42

Figure 3.17 Waveguide spectrum of straight waveguide. ...……. 43

Figure 3.18 Coupling ratio for the waveguide between different lots. ...……..… 44

Figure 3.19 Measurement and simulation data of coupling ratio between different lots … ……45

Figure 3.20 Simulation data of coupling ratio considering variation of thickness of wafer or slab. (a) simulation considering thickness of wafer (b) simulation considering thickness of slab ……..……. 46

Figure 3.21 Simulation data of coupling ratio considering variation of thickness of wafer and slab. ……..……..46

Figure 3.22 Experimental data for the transmission and FSR of the ring mixer. (a)Transmission, (b) FSR with comparison with simulation. ……...…48

Figure 3.23 Resonance spectrum from silicon ring mixer. Resolution of OSA is 2pm... 49

Figure 4.1 Principle of multiple tone pump (a) first round trip, and (b) after first trip.... 52

Figure 4.2 FWM for comb generation, with multiple tones. (a) Two tone input. (b) Multiple tones input). …...…… 54

Figure 4.3 Experimental setup for multiple tone with silicon mixer. (a) Setup schematics, (b) picture of the setup, (c) picture of the silicon mixer on the stage with electrode probe for PIN and heater. ..…..……..…… 56

Figure 4.4 Procedure for multiple pump. ..……..……. 57

Figure 4.5 Example of spectrum of single pump. ……...……..……...… 58

Figure 4.6 Spectrum of two pump with different RF frequency (a) RF: 25.225GHz with conversion efficiency of 14dB (b) RF: 25.255GHz with conversion efficiency of 17dB, and (c) RF: 25.275GHz with conversion efficiency of 18dB. …...…….. 60

Figure 4.7 Spectrum of two pump with different FSR separation of pump (a) 2FSR, (b) 4FSR, and (c) 5FSR. …...…..……... 60

Figure 4.8 Example of filtering input tones by POS (a) 30 tones before filtering ~25GHz for spacing, (b) 15 tones after filtering for ~50GHz spacing. ...…….. 61

Figure 4.9 Example of filtering of input tones for 15 tones with 50GHz, with comparison before/after phase tuning. The deviation of peak is suppressed less than 2dB, and its sidebands are generated by phase-by-phase tuning. ……..... 62

Figure 4.10 Output spectrum of the silicon mixer. The tuning condition is input power is 21dBm, RF frequency is 25.250GHz (i.e., Output frequency is 50.5GHz), and center frequency is 1549.4420nm. ……..… 64

Figure 4.11 Comparison of different RF frequency for comb generation. (a) RF: 25.217GHz, (a) RF: 25.250GHz, (c) RF: 25.255GHz, and (d) RF: 25.275GHz. …… 66

Figure 5.1. Setup of the measurement. ….……..…. 70

Figure 5.2. Flowchart of the measurement. …...……...……...… 71

Figure 5.3. Output signals of interference measurement for SMF-28 with setup illustrated in Figure 5.2. (a) Output signals. From the top, reference of k-clock, λ-reference, two interferograms from MZI, and corrected signals derived from the two signals from MZI. (b) Expanded area from (a) with green-flamed areas from single sweep with plotted as red. ……...… 72

Figure 5.4. Unwrapped phase from the corrected interferogram for SMF-28. …… 73

Figure 5.5. The relationship between time-domain and frequency domain which described as wavelength in the measurement. ……..……... 74

Figure 5.6. Unwrapped phase for SMF-28 with conversion from time-domain into frequency-domain and plot along wavelength. ……..…... 74

Figure 5.7. Dispersion for SMF-28. ……..… 75

Figure 5.8. Dispersion for Si waveguides. ……76

Figure 5.9 Output spectrum of comb generation for different devices according to chromatic dispersion D and power splitting ratio k at 1550nm. (a) Output from 15 tones input comb. (b) simulation for 15 tones. (c) Output from 7 tones input comb. (d) simulation for 7tones. ……..……...…….. 79

Figure 5.10 -20 bandwidth for 15 tones in Figure. 5.9. ..……..……... 80

Figure 6.1 Setup of the measurement. …...…….. 84

Figure 6.2 Output spectrum from parts of the setup for output from HNLF input to the chip (a) spectrum between 1540-1580nm. (b) spectrum between 1550-1570 for expansion. …… 86

Figure 6.3 Input/Output spectrum from chip. …….. 86

Figure 6.4 Output spectrum from the chip (a) comparison of spectrum between different RF. (b) expansion of input tones in the best effort in the (a) (red circled). ...…….. 87

Figure 6.5 Setup for phase noise measurement. …….. 88

Figure 6.6 PSD for mixing signal for different tones between 1st and 2nd (a) bandwidth until 1GHz, (b) bandwidth until 300MHz. ……... 89

Figure 6.7 SNR of carrier frequency in Figure 6.6. ……..... 90

Figure 7.1 Example of a setup for cascaded ring mixer. ……...…. 94

LIST OF TABLES

Table 2.1 Nonlinear coefficient and energy gap of nonlinear materials. ……...…….. 11

Table 3.1 waveguide loss for the waveguide between different lots from Figure 3.14. .. 42

LIST OF ABBREVIATIONS

AOM acousto-optic modulator

BF band-pass filter

BOX Buried oxide

CAGR compound annual growth

CMOS Complementary metal oxide semiconductor

DRC Design rule check

EDFA erbium doped fiber amplifier

FCA free carrier absorption

FCD free carrier dispersion

FWM four wave mixing

FWHM full width at half maximum

FSR free spectral range

MPW multiple project platform

MZM Mach Zehnder modulator

MZI Mach Zehnder interferometer

NLSE Nonlinear Schrödinger equation

OSA optical spectrum analyzer

PC polarization controller

PDK process design kit

PIC photonic integrated circuit

PM phase modulator

POS programmable optical processor

SEM scanning electron microscope

SiN silicon nitride

SNR signal to noise ratio

SiO_2 silicon dioxide

SOI silicon on insulator

SSB single sideband

TPA two photon absorption

VOA variable optical attenuator

WDM wavelength division multiplexing

ACKNOWLEDGEMENTS

I would like to thank to all the people who offered help and inspiration.

First and foremost, I would like to appreciate to my advisor, Prof. Stojan Radic, for his support on research in UCSD. His insights, knowledges, and experiences motivated me to explore research work in photonics. In addition, I must thank his continuous support in my entire PhD course. I would also like to thank all my committee members: Professor Miroslav Kristic, Professor Leonid Butov, Professor George Papen, Professor Yu-Hwa Lo, for their discussions and contributions into this dissertation.

I would like to express my special gratitude to Dr. Bill Ping-Piu Kuo, for his insight on research topics and help with my project with his depth knowledge and experiences.

I would like to thank all my colleagues in Photonics Systems Laboratory, to Dr. Liangshun Han and Dr. Ana Pejkic, with their extensive knowledge and help for the projects. I also thank for the help from all the past and present members of the lab: Dr. Nikola Alic, Dr. Andreas, O. J. Wiberg, Dr. Evgeny Myslivets Dr. Vahid Ataie, Dr. Lan Liu, Dr. Daniel Esman, Dr. Eduardo Temprana, Dr. Kevin Young, Dr. Yun Gao, Dr. Huan Hu, Dr. Jin Zhang, Elham Serahati, Nanzhe Hu, and Jason Leng.

Finally, I would like to thank my family with their supports and understanding for my decision to pursue PhD degree in UCSD.

Chapter 3, and Chapter 4, in part is currently being prepared for submission for publication of the material. Motohiko Eto, Bill Ping-Piu Kuo, and Stojan Radic. The dissertation author was the primary investigator and author of this material.

Chapter 5, in part has been submitted for publication of the material. Motohiko Eto, Bill Ping-Piu Kuo, and Stojan Radic. The dissertation author was the primary investigator and author of this paper.

Chapter 6 is in parts currently being prepared for submission for publication of the material. Motohiko Eto, Bill Ping-Piu Kuo, and Stojan Radic. The dissertation author was the primary investigator and author of this material.

VITA

2002-2006 Bachelor of science in Physics,

Konan University, Japan

2006-2008 Master of science, in Physics,

Osaka University, Japan

2008-2014 Industrial R&D engineer,

Mitsubishi Electric Corporation, Japan

2014-2021 Doctor of Philosophy in Electrical Engineering (Photonics)

University of California San Diego, USA

Publications

Journal Articles:

Motohiko Eto, Bill P-P. Kuo, and Stojan Radic. **“**Measurement method to determine chromatic dispersion for short length optical waveguides” (submitted)

Motohiko Eto, Bill P-P. Kuo, and Stojan Radic. **“**Frequency comb generation in c-band with silicon ring mixer” (in preparation)

Conference proceedings:

Han, Liangshun, Bill P-P. Kuo, **Motohiko Eto**, Ana Pejkic, Jin Zhang, Nikola Alic, and Stojan Radic. "Silicon Photonic 50GHz Wavelength (De) Multiplexer with Low Crosstalk and Flat Passband." In CLEO: Science and Innovations, pp. STu4B-3. Optical Society of America, 2018.

ABSTRACT OF THE DISSERTATION

Parametric Process on Silicon Microchip Mixer

by

Motohiko Eto

Doctor of Philosophy in Electrical Engineering (Photonics)

University of California San Diego, 2021

Professor Stojan Radic, Chair

Optical parametric process, such as four wave mixing (FWM) is attracted to applications for comb generation in Wavelength-Division-Multiplexing (WDM) systems based on fiber-optic systems. The other aspect in these years is the technology based on Photonic Integrated Circuit (PIC) with Complementary Metal Oxide semiconductor

(CMOS) technology, which enhanced the integration of optical components for optical parametric processing is called Silicon photonics. In the current status, most studies on optical parametric processing in telecommunication band is studied in Silicon nitride, due to its lower optical loss (linear loss) and low two-photon absorption (TPA) as a nonlinear loss. However, for the integration of the optical components into the well -developed CMOS process, it is highly desired to generate comb lines with Silicon-based mixers. In this dissertation, we introduce a new track to generate frequency combs through parametric process through silicon mixer. As a result of this approach, wide spectral bandwidth with dense comb lines with coherence is obtained and stabilized from the accessible manner.

As a study of mechanism and design aspect, dispersion engineering, phase-matching condition and TPA effect on the silicon mixer are investigated. For the effective FWM, elaborate design for waveguide cross-section and coupling loss composed, and enhanced PIN structure with reverse bias is applied to the system. To wrap up, this dissertation includes the design and experiment of the parametric mixers based on CMOS compatible silicon devise to demonstrate broadband low-noise frequency comb with dense lines.

Chapter 1

Introduction

1.1 Motivation

In the internet era, the global data center traffic is forecasted to be growth 3.2-fold by every year between 2016 and 2023, with compound annual growth (CAGR) of 26% (Figure 1.1) [1]. It is expected to reach 502 exabytes in 2023. This rapid growth of internet traffic demands low-loss broad bandwidth in communication networks, such as wavelength division multicasting (WDM, and most optical network is constructed by fiber-optic components. However, the increase of channel and accordingly increase of components demands higher energy consumption. To address this, low consumption optical components that compatible current device/systems is highly desired.

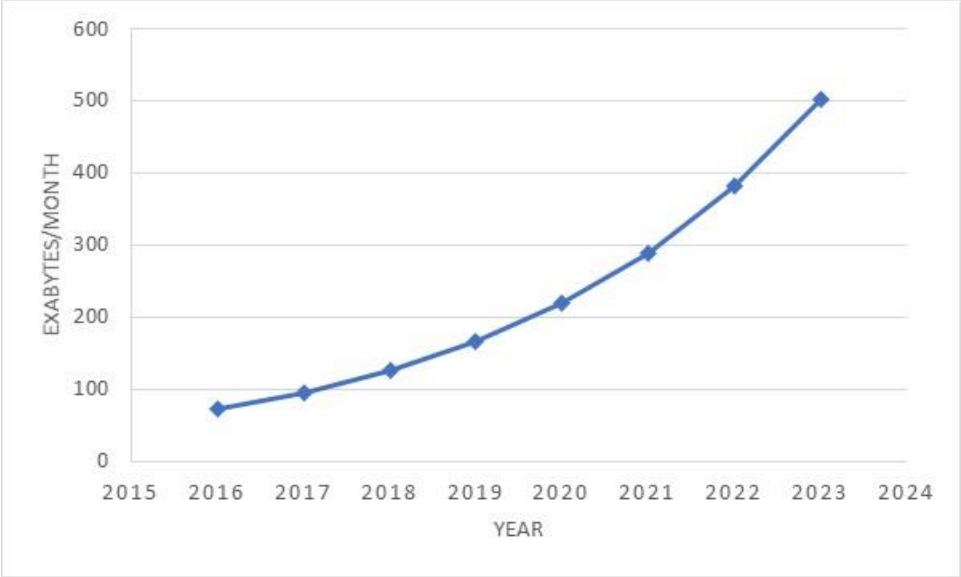

Figure 1.1 Global internet traffic growth in 2016-2023

Optical frequency comb can be used as wavelength channels in communication, such as WDM [2]. After the invention of optical frequency comb, this equally spaced lines in frequency-domain. The first and most popular scheme is using laser system, typically mode-locked laser. The optical frequency combs generated by these systems can be applied to the various fields, such as telecommunications [3], molecular spectroscopy [4], optical clock [5] and LIDAR [6].

The other up-coming trend is an integration of optical devices into a silicon chip, in the field area of "silicon photonics "[7-14]. In the field of electronics, the fabrication technology for silicon chip is developed for a long time and matured. Therefore, the development of optical components on a silicon chip is studied and succeeded in both of research and industrial level, except for the laser sources, named photonic integrated circuit (PIC). Back to optical frequency combs, its generation method is mainly relying on laser technology, such as mode-locking in cavity. However, it is unrealistic to fabricate optical cavity in the microchip, due to its larger size (~10m in length) for GHz order for telecommunication application. There is the other technique to generate frequency a comb, that called four wave mixing (FWM), and is applicable for a chip material such as, silicon nitride (SiN), or silica [15-17]. As an application for coherent communications [18-20], frequency comb generation with FWM on silicon-based ring resonators in telecommunication band is highly desired, due to its compatibility to complementary metal-oxide-semiconductor (CMOS) process. Nonetheless, optical loss derived from strong free carrier absorption (FCA) originated in two photon absorption (TPA) in telecommunication band prevents its application from comb generation except

for infrared region [21-23]. Recently, comb generation in a silicon ring resonator modulator was studied, but its mechanism is based on electro-optic modulation in a silicon ring modulator [24].

This circumstance stimulates the work in this dissertation to generate multiple tones with silicon mixer, which potentially applicable for the source for the application discussed above.

1.2 Dissertation overview

This Dissertation demonstrates the theoretical framework, design, and experimentation and application experiment of silicon mixer. The theoretical backgrounds of parametric processing in engineering, coupling constant, and phase matching, are discussed in Chapter 2.

The parametric process for silicon mixer is studied in Chapter 3. With silicon mixer, which designed based on the discussion in Chater2, conversion efficiency and TPA effect are investigated in simulation and experiment. In the Four Wave Mixing (FWM), which is the mechanism for comb generation for silicon mixer, conversion efficiency and TPA effect are critical to achieve multiple tones in optical frequency comb.

According to the investigation of the efficiency of FWM in the silicon mixer, system setup and condition to generate optical frequency comb is studied in Chapter 4. In this system, input into the silicon mixer is set as multiple tone, is investigated, due to the limit of peak power, and the tuning process using phase shifter. From the systematic point of view, these are essential elements for enhanced comb generation. Theoretical

investigation is described upon the system, and experimental demonstration is following to enhanced comb generation.

In Chapter 5, the relationship between chromatic dispersion and FWM efficiency is more investigated in detail. For chromatic dispersion, it defines the efficiency of FWM, and sensitive in the fabrication process for silicon mixer. The effect on the relationship of different dimension and efficiency is studied in simulation and experimentally. For the chromatic dispersion, interference measurement setup with swept-source is constructed and verified its accuracy with measurement for SMF.

As a source for telecommunication, coherence of the generated is comb is important. In Chapter 6, the experiment to measure phase noise of comb is implemented. The input setup is revised to decrease phase noise from the system, and as a result, broad spectrum between 1525-1600m, at -75 dBm noise floor is also performed.

In conclusion, the dissertation is summarized with the work and future work in Chapter 7.

Chapter 2

Parametric process and device characterization for silicon mixer

To investigate the mechanism for comb generation in the mixer based on ring structure, it is important to introduce the phenomenon related to nonlinear optics and structure of ring mixer. For the nonlinear optics, it is crucial to discuss χ_3 order of nonlinearity and four wave mixing as a primary mechanism for comb generation in this dissertation. Accordingly, chromatic dispersion and two photon absorption is discussed due to its effect on the efficiency of comb generation. In addition, as micro ring mixer structures, nonlinear Schrödinger equation is discussed to study wave propagation in the waveguide with nonlinear medium. Other characteristics, such as coupling, Q factor and finesse are also discussed to achieve efficient mixing in the ring structure.

2.1 Nonlinear effects in dielectric medium

In the nonlinear medium, including silicon, polarization is described with nonlinearity as following [25],

$$P(t) = \varepsilon_0[\chi_1 E((t) + \chi_2 E_2((t) + \chi_3 E_3((t) + \ldots] \quad (2.1)$$

Where ε_0 is the permittivity in free space, χ_1 is the linear susceptibility, χ_2 and χ_3 is the linear susceptibilities. For the materials those have crystal symmetry, including silicon or silicon dioxide (SiO_2), the nonlinear effect originate in χ_2 is annihilates. Therefore, for these materials, third order nonlinearity originated from is applied for nonlinear effects.

In this nonlinear medium that exists χ_3 in a term in (2.1), input signal causes spontaneous emission, that distribute photon in the medium, as white noise. Its distribution follows Poisson distribution. The white noise in the χ_3 medium is the origin of optical parametric process.

2.1.1. Four wave mixing

Four wave mixing is the process that to generate output signals by interaction between input pumps and signals. The photon generated in spontaneous emission can be the signal in this process. Four wave mixing is divided into two types that degenerate and nondegenerate FWM. In degenerate FWM, the input signal and pump generate another frequency, called idler as following (Figure.2.2),

$$\omega_s = \omega_p + \omega_p - \omega_i \tag{2.2}$$

where ω_s , ω_p , and ω_i are the frequencies for signal, pump, and idler. As shown in the energy diagram in Figure. 2.2, electron is pumped to excite state via virtual state, and emitted as idler frequency. For nondegerate FWM, there are multiple pump frequency. For degenerate FWM, in the case of two pumps are incident into the nonlinear medium, they generate two idlers, as following (Figure.2.2),

$$\omega_{i2} = \omega_{p1} + \omega_{p2} - \omega_{i1}$$

$$\omega_{i1} = \omega_{p1} + \omega_{p1} - \omega_{p2} \tag{2.3}$$

$$\omega_{i2} = \omega_{p2} + \omega_{p2} - \omega_{p1}$$

In comparison to the degenerate FWM, two pumps have function of pump and idler for each other in this case, and the two idlers appear on both sides of the two pumps. In the case of multiple pumps, based on this two pump case, each pump has the function of pump and idler, and generates side bands as idlers. Furthermore, in the case of those idlers have enough power as pumps, other idlers are generated as cascaded sidebands. This cascaded degenerate FWM is the essential concept to generate multiple tones in a silicon mixer, whose medium has relatively low efficiency as a nonlinear medium. In this dissertation, efficiency and cascaded generate FWM are discussed later.

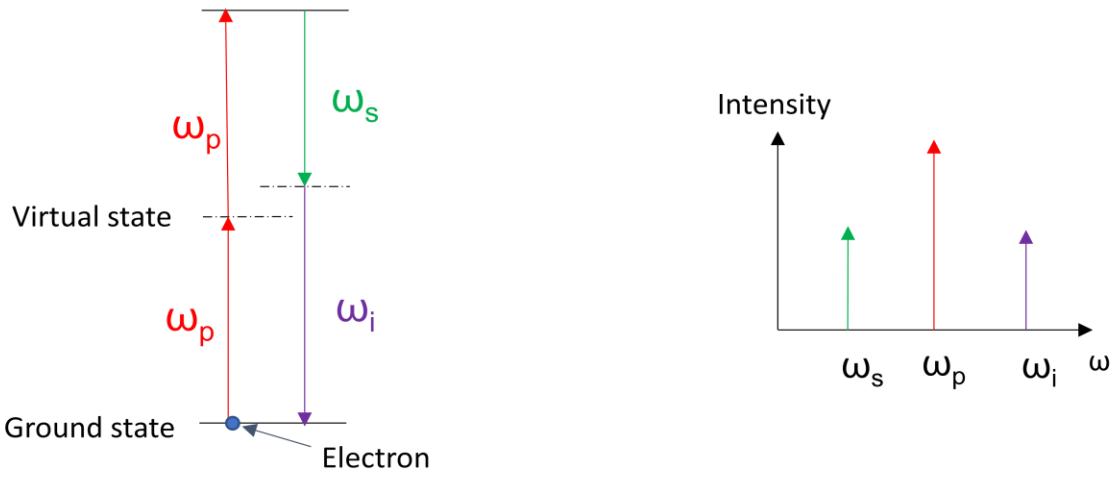

Figure. 2.1 Degenerate Four wave mixing

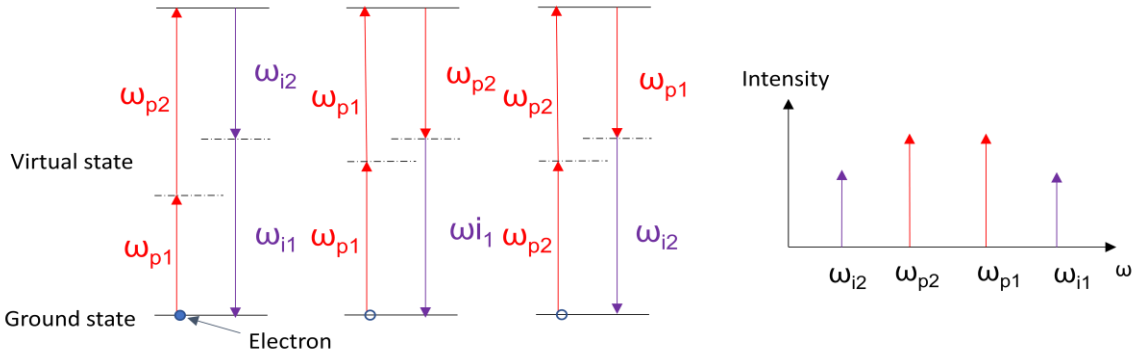

Figure. 2.2 Two tone parametric process based on degenerate FWM.

2.1.2 Chromatic dispersion

As another effect in nonlinear medium, different frequency components in an optical wave have different delays, named as chromatic dispersion. Because different frequencies have different refractive index, it causes delay in the nonlinear medium. This is called material dispersion. In addition, cross-section of the waveguide affects the total dispersion, and this is called as waveguide dispersion (Figure 2.3). Subsequently, total dispersion is described in wavelength-domain as,

$$D = \underbrace{-\frac{1}{c\lambda}\left(\lambda^2\frac{\partial^2 n}{\partial\lambda^2}\right)}_{\text{Material dispersion}} + \underbrace{\frac{1}{c\lambda}\left(\lambda^2\frac{\partial^2 n_{eff}}{\partial\lambda^2}\right)}_{\text{Waveguide dispersion}} \quad (2.4)$$

where n is a refractive index, n_{eff} is an effective refractive index depends on the cross-section of a waveguide. This total dispersion indicates that the dispersion is controllable for applications.

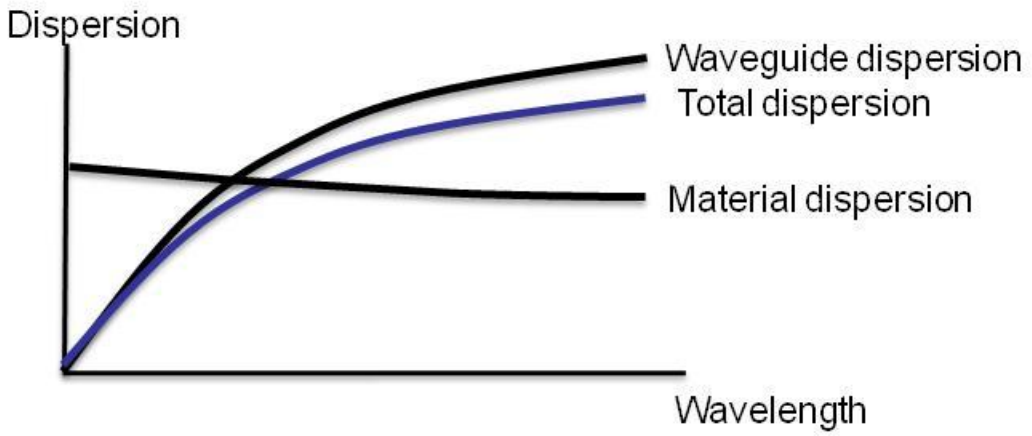

Figure. 2.3 Example of the relationship between dispersions

2.1.3 Two photon absorption (TPA)

Two photon absorption is the process that two photons are absorbed to excite electron to the excited state in high intensity of light [26]. For silicon, its energy gap (Eg) is ~1.12eV in telecommunication band, and this is larger than energy in TPA with 1.6eV (Figure.2.4) [27]. Then, excited electron and hole in variance band work as free carriers and cause recombination on the surface or interface of a waveguide. This phenomenon degrades the efficiency of optical parametric process, such as FWM. To decrease generation of free carriers reversed bias on PIN structure in the silicon waveguide, is introduced. Its structure is discussed with detail later in Chapter 3.

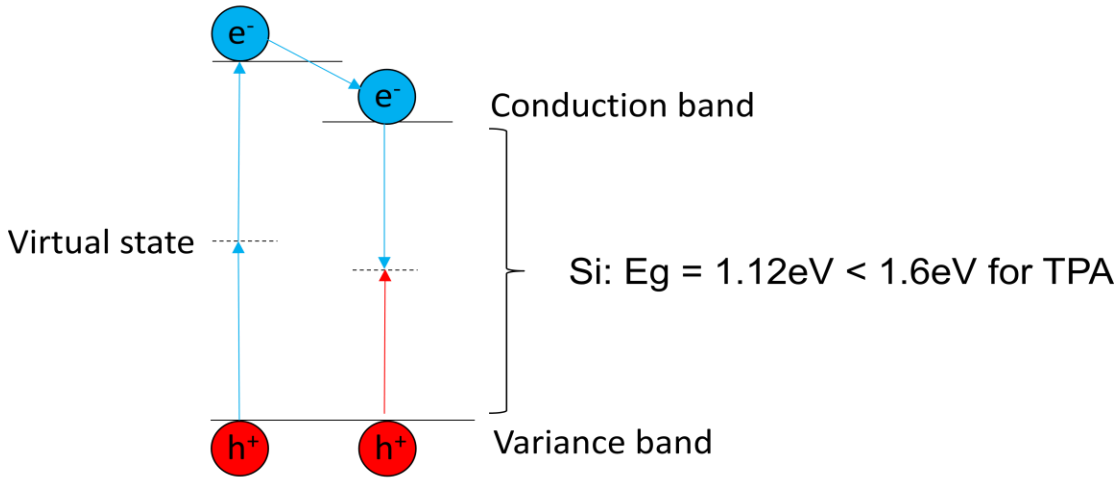

Figure. 2.4 Band diagram of two photon absorption

2.1.4 Nonlinear parameters

For parametric optical amplification including FWM, the gain is evaluated by the nonlinear coefficient defined as following,

$$\Upsilon = \frac{2\pi}{\lambda}\frac{n_2}{A_{eff}^{(3)}} \tag{2.5}$$

where n_2 is the nonlinear coefficient and A_{eff} is an effective index calculated by the cross section of a waveguide. Table 2.1 shows the nonlinear coefficient and energy gap of the nonlinear materials. Silicon has high nonlinear coefficient, and it potentially has high nonlinear gain defined by (2.5). However, due to its smaller band gap than that of TPA, actual gain is not high as expected; especially the experiment with high intensity of light is introduced into a waveguide, such as silicon waveguide in PIC. To overcome this

hindrance, PIN structure is introducing in the rib waveguide and diligent management of peak power and number of tones, are introduce in this dissertation.

Table 2.1 Nonlinear coefficient and energy gap of nonlinear materials [28]

	n_2 @ 1.5 μm [m^2/W]	E_g [eV]
Si	~$4 \cdot 10^{-18}$	1.14 (<1.6 for TPA)
SiN	$0.24 \cdot 10^{-18}$	~5 (>>1.6 for TPA)

2.2 Micro ring mixer mechanics

In this dissertation, the structure of mixer is based on mirroring resonator, which has the coupler between bus and ring, and a part of the wave from bus waveguide couples into the ring and propagate, and couples again in the coupler. As an advantage of adopting this structure, comparing to a FWM in a straight waveguide, it is possible to curtail insertion loss in the system. Because typical silicon waveguide loss is ~2dB/cm and has free carrier loss from TPA in high intensity of light, a long waveguide does not necessarily guarantee high conversion efficiency in FWM. For the design of silicon mixer, there are topics to discuss in the following sections.

2.2.1 Nonlinear Schrödinger equation

Nonlinear Schrödinger equation (NLS) models electromagnetic wave propagation in a waveguide. For the field propagates in the nonlinear medium is described as [29],

$$\frac{\partial E(z,t)}{\partial z} = -\frac{\alpha}{2}E - \frac{\sigma}{2}(1+i\mu)N_c E + ik_0 n_2(1+ir)|E|^2 E \quad (2.6)$$

where,

$$r = \frac{\beta_{TPA}}{2k_0 n_2} \quad (2.7)$$

and Nc is described in a rate equation as,

$$\frac{\partial N_c}{\partial t} = -\frac{N_c(z,t)}{\tau_c} + \frac{\beta_{TPA}}{2h\nu_0}|E(z,t)|^4 \quad (2.8)$$

Here, in (2.7), β_{TPA} is TPA induced propagation parameter. In (2.8), N_c is TPA induced free carrier concentration, and μ is TPA induced free carrier dispersion (FCD). Accordingly, (2.6) includes TPA effect and effect of free carrier absorption originated in TPA. This NLS equation is solved with split-step Fourier method discussed in the references [30].

2.2.2 Transmission and phase matching

For transmission of a mirroring with an amplitude defended by $a^2 = \exp(-\alpha L)$ with attenuation coefficient α [1/cm], self-coupling constant t is introduced, and the transmission of a ring is described as (Figure. 2.5) [31,32],

$$T_n = \frac{I_{pass}}{I_{input}} = \frac{a^2 - 2t^* a\cos\emptyset + t^{*2}}{1 - 2at^*\cos\emptyset + (t^* a)^2} \quad (2.9)$$

Where, ϕ is a phase of propagation wave, and intuitively it has a condition that it is equal to the multiple of 2π, ring mixer does not transmit the wave ($T_n = 0$). Then, related to the ring structure, there is a phase matching condition for a wavelength λ_0 and length of a ring as,

$$\phi\ (\lambda_0) = n_{eff}\ (\lambda_0)L\ . \qquad (2.10)$$

Therefore, this is related to the multiple integers of 2π for no transmission.

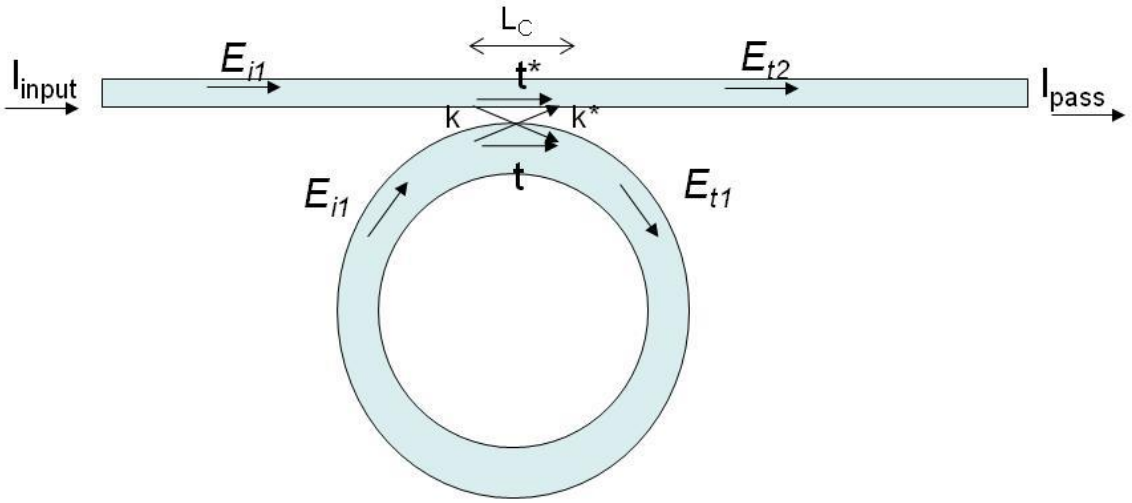

Figure. 2.5 Transmission and coupling in a ring mixer

2.2.3 Coupling in a ring

For coupling in the ring mixer is described as matrix elements,

$$\begin{pmatrix} E_{t1} \\ E_{t2} \end{pmatrix} = \begin{pmatrix} t & k \\ -k^* & t^* \end{pmatrix} \begin{pmatrix} E_{i1} \\ E_{i2} \end{pmatrix} \qquad (2.11)$$

where k is a coupling constant and t is a self-coupling constant, and E_{t1} and E_{t2} are the fields for bass waveguide and ring, after the coupling in the ring mixer. These have the relationship in the case that there is not coupling loss,

$$k^2 + t^2 = 1. \tag{2.12}$$

When these coupled waves satisfy phase matching condition (2.10), the ring mixer holds resonance. For the spacing between the resonances is called free spectral range (FSR) with defined as,

$$FSR = \frac{\lambda^2}{n_g L} \tag{2.13}$$

Depending on the relationship between self-coupling constant t and amplitude a, there are coupling conditions with FSR. In Figure. 2.6, there are the trends of transmission, energy diagram, and pulse propagation for each coupling condition. In this figure, first, t* > a is a under coupling that power coupling in the ring is less than bus waveguide. Then traveled power circulated in the ring. Second, t* = a is a under coupling that resonance wavelength λ_0 cannot come out from the ring, hence extinction ratio is the highest in the coupling conditions. Finally, t* < a is over coupling that power coupled into the ring is larger than bus waveguide. Then traveled power circulated in the ring. Because it is possible to change coupling constant with changing coupling length, it is crucial to optimize coupling constant for efficient FWM in the ring mixer.

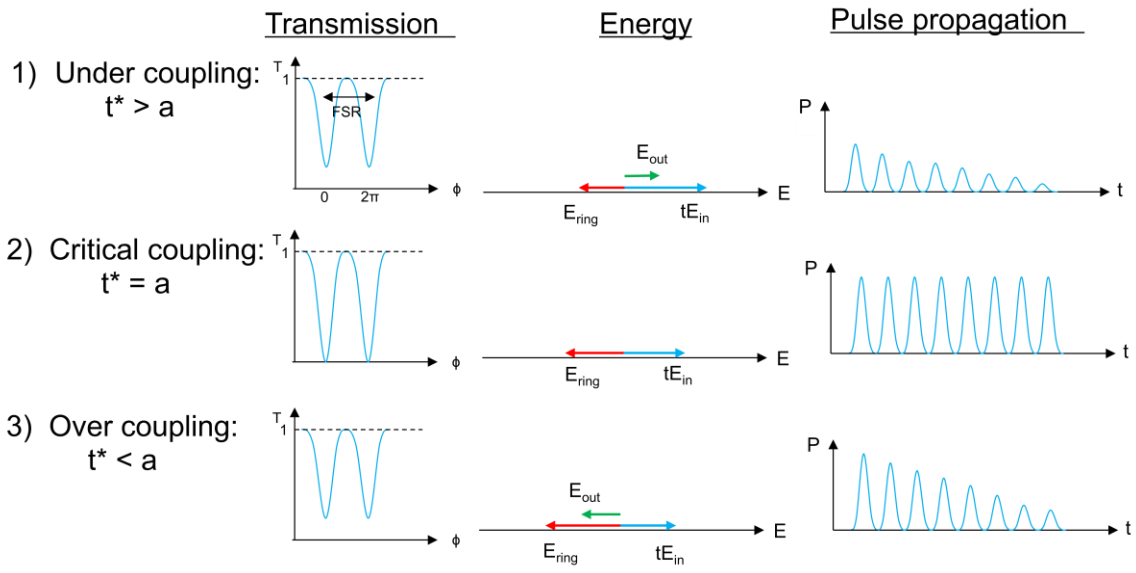

Figure. 2.6 Coupling condition and trends

2.2.4 Q factor and finesse

To characterize resonance in a ring mixer, Q factor and finesse are introduced. For Q factor, which defends shape of resonance, is described as both in experimentally and theoretically,

Experiment:

$$Q = \frac{\lambda_{res}}{FWHM} \tag{2.14}$$

Theory:

$$Q = \frac{\pi n_g L \sqrt{t^* a}}{\lambda_{res}(1 - t^* a)} \tag{2.15}$$

where, λ_r is a resonant wavelength, and FWHM is full width at half maximum of resonance width. For finesse, it is also defined as,

Experiment:

$$Finesse = \frac{FSR}{FWHM} \tag{2.16}$$

Theory:

$$Finesse = \frac{\pi\sqrt{t^* a}}{(1 - t^* a)}. \tag{2.17}$$

In Figure. 2.8, there are trends for Q factor and finesse, for Q factor is related to the sharpness of the resonance, and in high Q factor indicates sensitive and low energy loss, and low Q factor indicates vice versa. For finesse, high finesse indicates sensitive with wide FSR, and low energy loss, and low finesse indicates vice versa. Accordingly, it is crucial to choose appropriate Q factor and finesse by selecting parameters in (2.15) and (2.17) in device characterization.

(a)

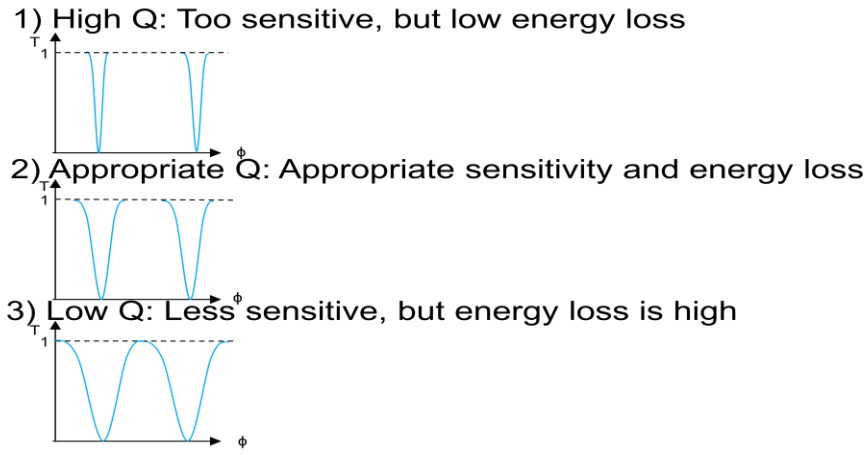

(b)

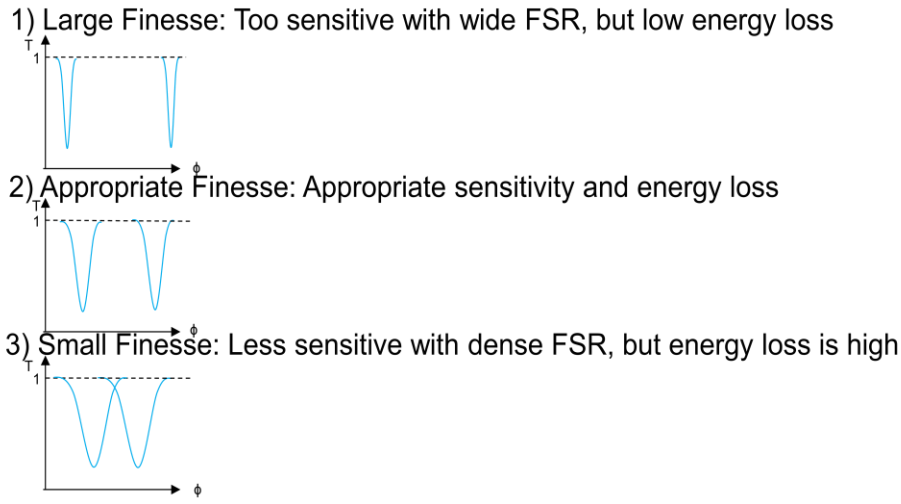

Figure. 2.7 Trends in Q factor and finesse for ring mixer (a) Q factor (b) Finesse

Chapter 3

Mixer characterization and design for comb generation

As discussed in chapter 2, it is essential to choose appropriate parameters to design silicon ring mixer, for efficient FWM. In this chapter, the design and performance of mixer is demonstrated via theoretically and experimentally. In the first half of the sections, each factor discussed in chapter 2 is investigated to determine the structure of silicon ring mixer. In the later section, there is a simulation of comb generation via FWM, based on NLS equation discussed in chapter 2. In the simulation, the structure of the mixer is originated from the device characterization, and its performance is securitized beforehand device fabrication. Finally, there is a review of silicon mixer design and fabrication process through CMOS-compatible multiple project platform (MPW) platform.

3.1 Device characterization

For the mechanism of the comb generation on silicon mixer, device characterization has an important role to explore appropriate design based on theoretical investigation discussed in chapter 2. Here, the primal parameters, such as dispersion of length, length of ring, coupling ratio, and reverse biased PIN structure, are analyzed, based on simulation and experimentation for the fabricated device.

3.1.1 Dispersion engineering

In the device characterizing for silicon mixer, dispersion engineering has the priority, because it affects the other multiple parameters as length of ring and coupling length. As discussed last chapter, dispersion is consisting of material and waveguide dispersion, and the material is fixed in silicon in this dissertation. Therefore, the procedure is executed for design of waveguide cross section. For the waveguide structure, it is a slab waveguide for PIN structure. In the case that the thickness fixed as H is 275m and slab height as h is 55nm, dispersion changes as its width. Figure. 3.1 shows the dispersion along with variety of widths. In the figure, the dispersion curve increases as the width wider.

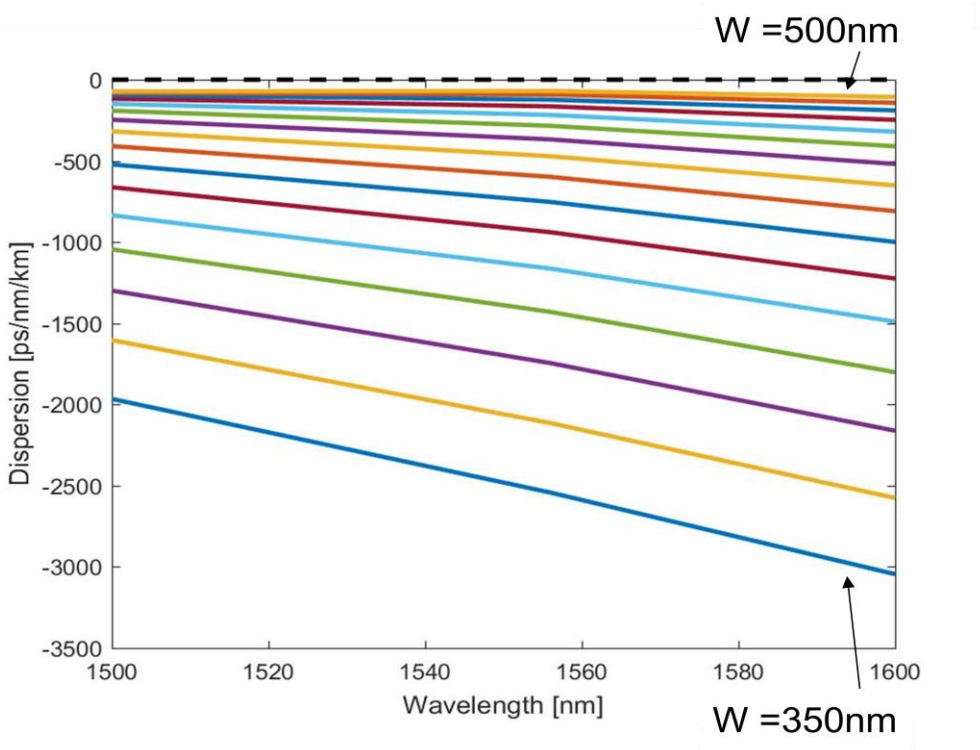

Fig.3.1 Dispersion of silicon waveguide with variation of width. Waveguide height H is 275nm, slab height h is 55nm, and variation of width W is between 350 and 500nm with 10nm step.

To achieve high efficiency in FWM, it is critical to avoid phase mismatch, and it is described as [33],

$$\Delta\beta = \frac{2\pi\lambda^2}{c}(f_i - f_k)(f_j - f_k)\left[D(\lambda) - \frac{\lambda^2}{c}\left(\frac{f_i + f_j}{2} - f_{ijk}\right)\frac{dD(\lambda)}{d\lambda}\right]. \quad (3.1)$$

Then, to decrease phase mismatch, for dispersion terms, D and its 1st derivative should be close zero. Therefore, in the variation of width, wider width is appropriate. However, there is another restriction for the width, due to the necessity to avoid mode crossing of the wave propagating in a waveguide. For this reason, w =460nm is chosen an example for the design. Figure.3.2 shows its optical confinement and dispersion. In this cross

section, a quasi-single mode that there is TE1 in (b), and there is not mode crossing shown in (c).

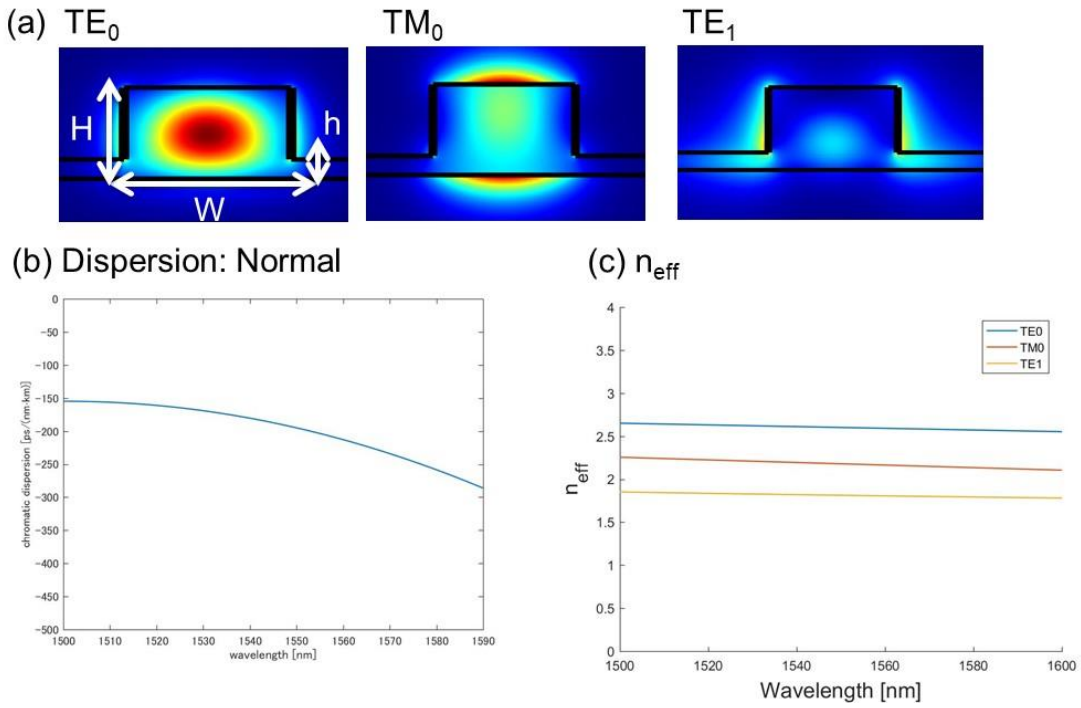

Figure. 3.2 Example of quasi-single mode waveguide. (a) cross section and modes, (b) dispersion curve, and (c) effective index for each mode.

3.1.2 Length of ring

As discussed in chapter 2, ring length affects the efficiency of FWM, and parameters related resonance as Q factor and finesse. For the efficiency of parametric process is defined as,

$$\eta = \gamma P L_{eff} \tag{3.2}$$

where, γ is nonlinear length defined as,

$$\gamma = \frac{kn_2}{A_{eff}}, \tag{3.3}$$

and L_{eff} is effective length as following,

$$L_{eff} = \frac{1 - e^{-\alpha L}}{\alpha}. \tag{3.4}$$

Figure.3.3 shows the efficiency of parametric generation described depends on the length of ring. Because the effective length saturates in longer length, it is shown that the efficiency saturates about L = 6cm in this setting. Accordingly, as a device parameter, it is enough to set the length less than about 6cm. However, from the point of view for device fabrication, it is also affected by waveguide loss that is susceptible to surface roughness in device fabrication. Then, in the case of the waveguide loss is worse than the 1.5dB, the appropriate length is less than this setting.

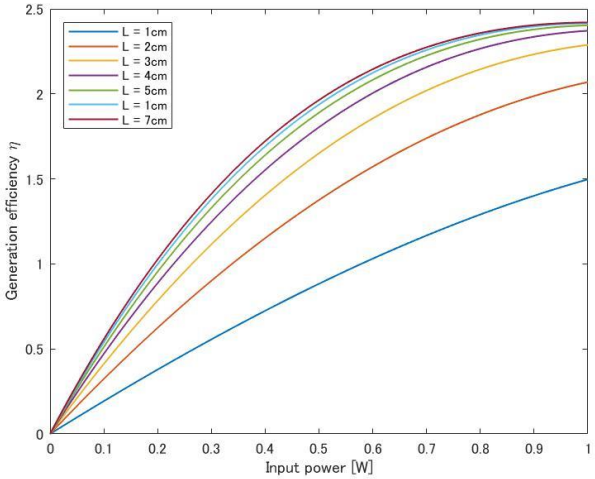

Figure 3.3 Efficiency of parametric amplification. Device parameters are, waveguide loss = 1.5(dB/cm), pump wavelength = 1550nm, nonlinear refractive index $n_2 = 4.0^{-18}$, effective area $A_{eff} = 6.955^{-14}(m^2)$, Pump power P = ~1W (30dBm).

For the other factors, there is Q factor and finesse, which related to the resonance. Figure 3.4 shows Q factor and finesse along length of ring. As these figures show, both Q factor and finesse decrease as the length is longer, i.e., Q factor suggests less sensitive and higher energy loss in the ring, and finesse suggests also less sensitivity with dense FSR and higher energy loss. However, these changes are relatively smaller comparing to their absolute values. Thus, as a factor to design length of the ring, generation efficiency is the primal in from these discussions.

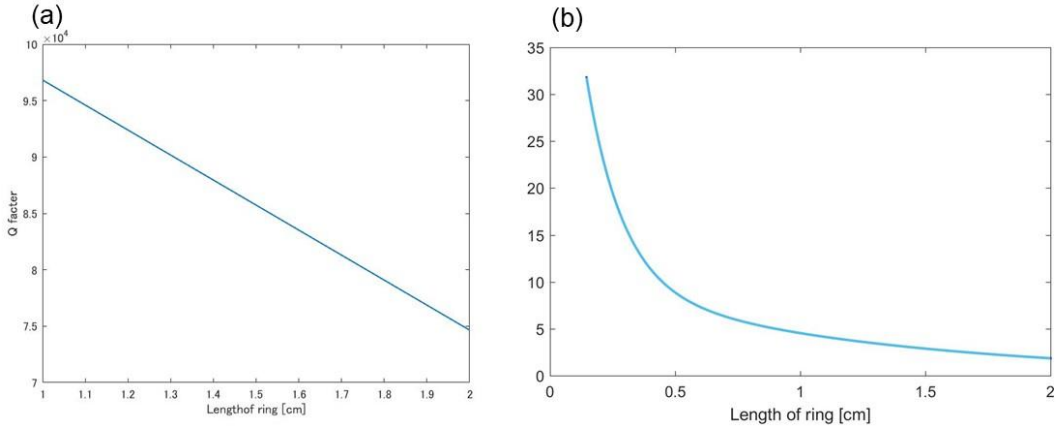

Figure 3.4 simulation of loaded Q factor and finesse along length of ring (a) Q factor, and (b) finesse along length of the ring. Here, waveguide loss is 1.5dB/cm, and group index (n_g)is set as n_g: 4.1186.

Related to loaded Q factor and finesse, Figure 3.5 shows the transmission in the ring with different coupling constant. In the figure, there is a variation of length of the ring between 1 and 3cm. As the length increases, the resonance is less sensitive as discussed in Q factor. Also, in the longer length, it is difficult to achieve critical coupling

and accordingly transmission is in high loss. From this point of view, the appropriate length of the ring will not succeed in these lengths.

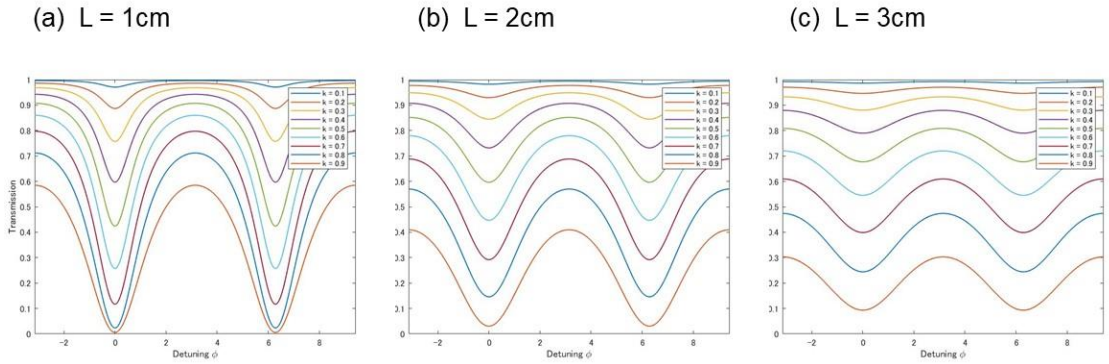

Figure 3.5 Transmission of the ring with different coupling constant. The variation of the length of rings are (a) 1cm, (b) 2cm, and (c) 3cm. The device parameters are simultaneous as Fig.3.3. Here, waveguide loss is 1.5dB/cm.

3.1.3 Coupling ratio

As discussed in section 3.1.2, it is ideal for efficient FWM to achieve critical coupling with appropriate length of the ring. Figure 3.6 shows power splitting ratio based on different coupling constant k. the power splitting ratio is defined as k^2. For both cases, the power splitting ratio increases as the coupling length lc increases due to the mode coupling. The slopes are originated in nonlinearity of coupling modes. In (b) that width W is 500nm, it is difficult to achieve k^2 over 0.5, i.e., k is nearly 0.7. Then, for this cross section, it is difficult to achieve critical coupling as mentioned in the last section, except for the gap is shortened. However, shortening the gap can be a hindrance in the

fabrication process. On the other hand, in (b) that width W is 460nm, it is achievable to critical coupling about coupling length lc is 40μm. Then, this is the appropriate design for the direction coupler in the silicon mixer.

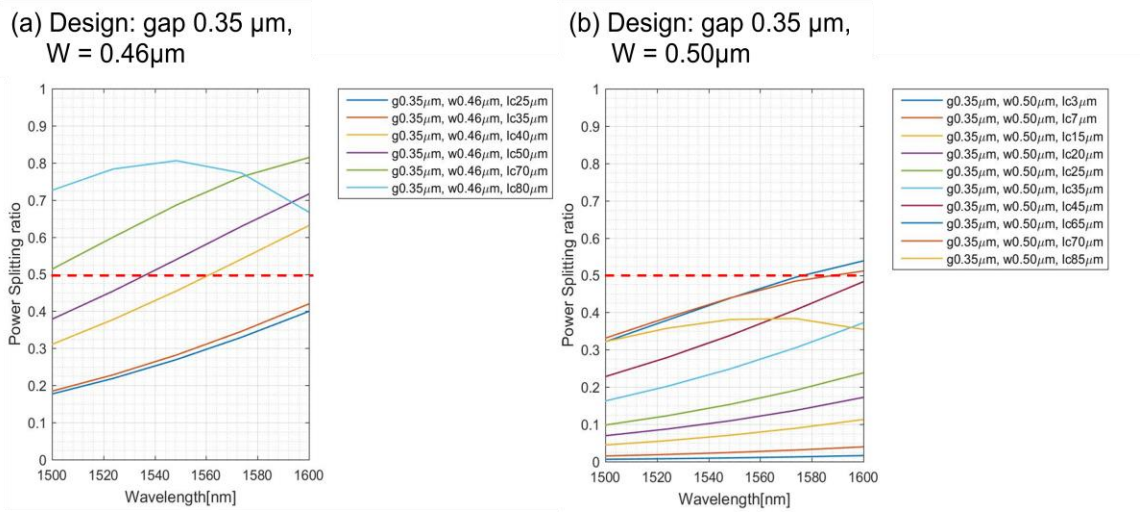

Figure 3.6 Power splitting ratio with different cross section. (a) W = 450nm, and (b) W = 500nm

3.1.4 PIN structure

In the silicon mixer, to sweep out the carriers, PIN structure is adopted to the silicon rib waveguide. Figure 3.7 shows the structure and application of PIN structure in the silicon waveguide. In this structure, in each end of slab waveguide, N type dopant and P type dopant is doped, and reverse bias is applied through the doping region. By applying reverse bias voltage on the PIN structure, carriers that consist of electron and hole, are sweep out from the intrinsic region where the wave propagating. Therefore, the

scattering in the region is decreases and as a result, the optical loss can also be decreased. Furthermore, this carrier generation is proportional to the intensity of light as in the case in this dissertation. It is critical to sweep those carriers for efficient FWM.

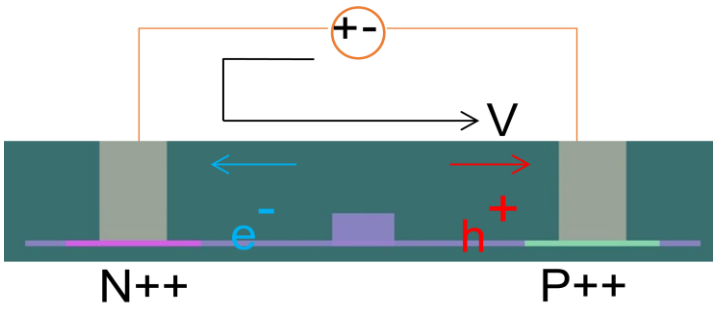

Figure 3.7 Silicon waveguide with reverse bias PIN structure

The efficiency of reverse bias PIN structure is evaluated with carrier lifetime. Average carrier lifetime is defined as following [34],

$$\tau_{avg} = \left(\frac{\tau_e + \tau_h}{2v_{e,h}}\right), \tag{3.5}$$

where, carrier lifetime is,

$$\tau_{e,h} = \frac{w}{2v_{e,h}}, \tag{3.6}$$

Here, the carrier velocity is defined, with carrier mobility $\mu_{e,h}$ and electric field E as following ,

$$v_{e,h} = \mu_{e,h} \cdot E \tag{3.7}$$

Then, the simulated carrier lifetime on the characterized silicon rib waveguide in the former sections are shown in Figure 3.8. This Figure shows in higher voltage carrier lifetime is decreased. This suggests that the generated carriers are swept out from the intrinsic region swiftly. With considering device fabrication, it is important to mention the deviation of the slab and carrier lifetime, because the slab thickness affects carrier lifetime, and its deviation is inevitable in such a thin layer of order less than 100nm. Figure 3.8 shows the deviation of slab height h and carrier lifetime with following effective carrier lifetime and slab height [34],

$$\frac{1}{\tau_{eff}} = \frac{1}{\tau_b} + \frac{S}{H} + \frac{W + 2(H - h)}{WH} S' + 2\frac{h}{H}\sqrt{\frac{D}{W^2}\left(\frac{1}{\tau_b} + \frac{S+S'}{h}\right)} \tag{3.8}$$

where, τ_b is bulk recombination lifetime S is interface recombination velocity, S' is surface recombination velocity, and D is diffusion factor defined by carrier mobility(μ); $D = \mu(kT/e)$. In this figure, there is 10% deviation for both waveguide height H and rib height h. This figure shows the trend that about 50nm thickness of height, the carrier lifetime decreases rapidly, and saturates in thick rib height. This also demonstrates thicker rib guarantees lower carrier lifetime. However, thin in the thin slab thickness, screening effect that the thin slab region performs as a register to decrease electric field in the core region. In addition, considering optical confinement, rib thickness should be as

less as possible, ideally a rib waveguide. With these considerations, in this dissertation, rib thickness is set as h = 55nm.

In an experiment of FWM of the ring mixer, current from PIN structure can be monitored to investigate the state of resonance, because in the resonance mode of a ring, more photons are accumulated in the ring than that of out of resonance. Accordingly, in resonance, generated photons cause more electrons and holes due to TPA effect discussed above and cause more current flow (TPA current) than out of resonance.

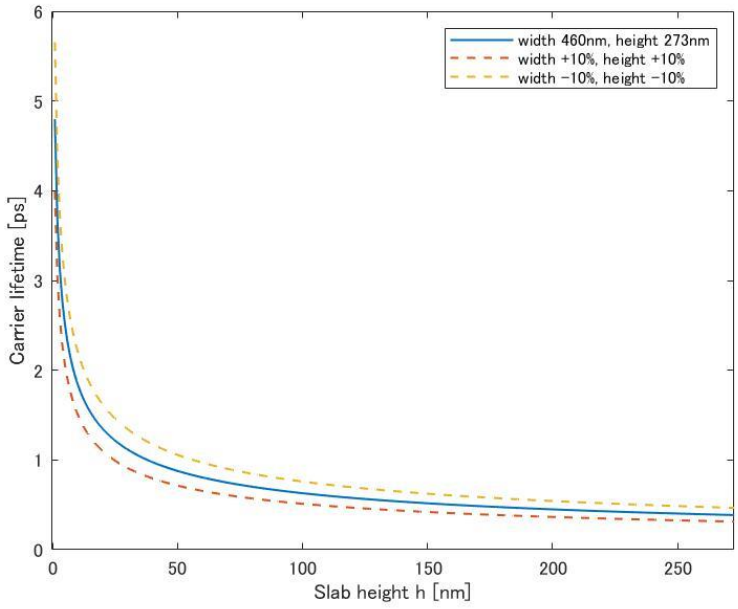

Figure 3.8 Relationship between deviation of slab height and carrier lifetime.

3.1.5 Avoid additional loss from PIN structure

As discussed in above section, PIN structure is useful to reduce PIN structure with applying reverse biased voltage, and to suppress the optical loss from TPA effect, its depletion region should be as less as possible, such as PN structure and distance between the cathode and anode should be as close as possible to strengthen the electric field to suppress. However, those distances affect optical loss in case that they are close enough to interfere electromagnetic field of optical waveguides. Figure 3.9 illustrates the simulation of optical loss against the distance between centers of a waveguide designed above and via D_D, made of Aluminum, that used in the parameter in design in PDK. Here, via width is fixed to 2μm, and waveguide width is 460nm, then the actual distance between the two is D_D – 1.23μm. The simulation indicates as close as the distance between a waveguide and via, more optical loss in the waveguide causes, especially less than 2μm. Then in the layout, 2.1μm is chose to compatible between the penalty of optical loss and maximization of field strength for PIN structure to reduce optical loss from TPA effect.

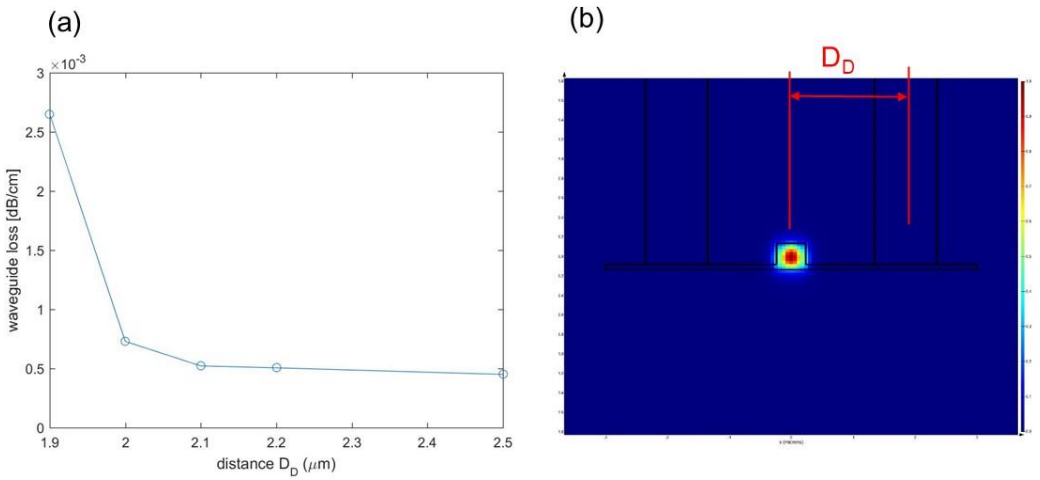

Figure 3.9 Simulation of optical loss from via against waveguide (a) distance against via D_D shown in (b). (b) cross section of waveguide and via.

For doping region, the idea is the same as the discussion above for via, but the effect also depends on the doping concentration of the two dopants, duet to its change of refractive index and loss, that changes in the range of index n between ~10^{-4} and ~10^{-1} for concentration between 10^{17} and 10^{20} [/cm^3] [35]. Here, the dopants are set as Boron as p-type dopant and phosphorous as n-type due to fabrication process. Figure 3.10 shows the three different design of dopant region. Here, design of waveguide and via is fixed discussed above. Figure 3.10 (a), (c), and (e) are design of dopant region with (a) p++ and n++ with concentration of 10^{20} [/cm^3], (b) is in addition to p++ n++ region, p+ and n+ with 10^{18} [/cm^3] is added, and (c) is in addition to (b), p and n with concentration of 10^{17} [/cm^3]. The design is started from (a) with a single set of doping regions with p++/n++, due to its effectiveness for the compatibility of optical loss and sweeping current of TPA effect. Figure 3.10 (b), (d), and (f) show the simulation results of the distance between dependence for optical loss for each design of dopant region described

in Figure 3.10 (a), (c), and (e). Here, it is denoted that the simulated optical loss does not include all factors in optical loss, such as surface roughness, that potentially causes optical loss majorly in measurement. The simulation is begun with Figure 3.10 (a) and (b) with a simple p++/n++ region, because these highest dopant affects compatibility between optical loss and sweeping current to reduce the loss due to TPA. Figure 3.10 (b) shows the distance between edge of waveguide and doping region is in case of less than ~0.9μm, optical loss is dramatically increase. This rapid increase of optical loss from the change of index due to the trend in each dopant level. However, the lower concentration that 10^{17}-10^{18} [/cm^3] causes less change of refractive index or loss, then these lower dopant regions can be designed to closer than higher dopant region, such as 10^{20} [/cm^3]. Comparing to the simulation result (Figure 3.10), the design including p/n and p++/n++ dopant achieves lowest optical loss with minimizing penalty of optical loss due to dopant regions. In this thesis, for fabrication, the design with simple p++/n++ shown in Figure 3.10(a) is chosen, due to dislocation of implantation may cause and avoid penalty of optical loss. However, the design with p+/n+ or p/n shown in Figure 3.10 (c) and (e) has a merit to reduce TPA loss, in the case of the fabrication tolerance is enough to be verified to satisfy these designs.

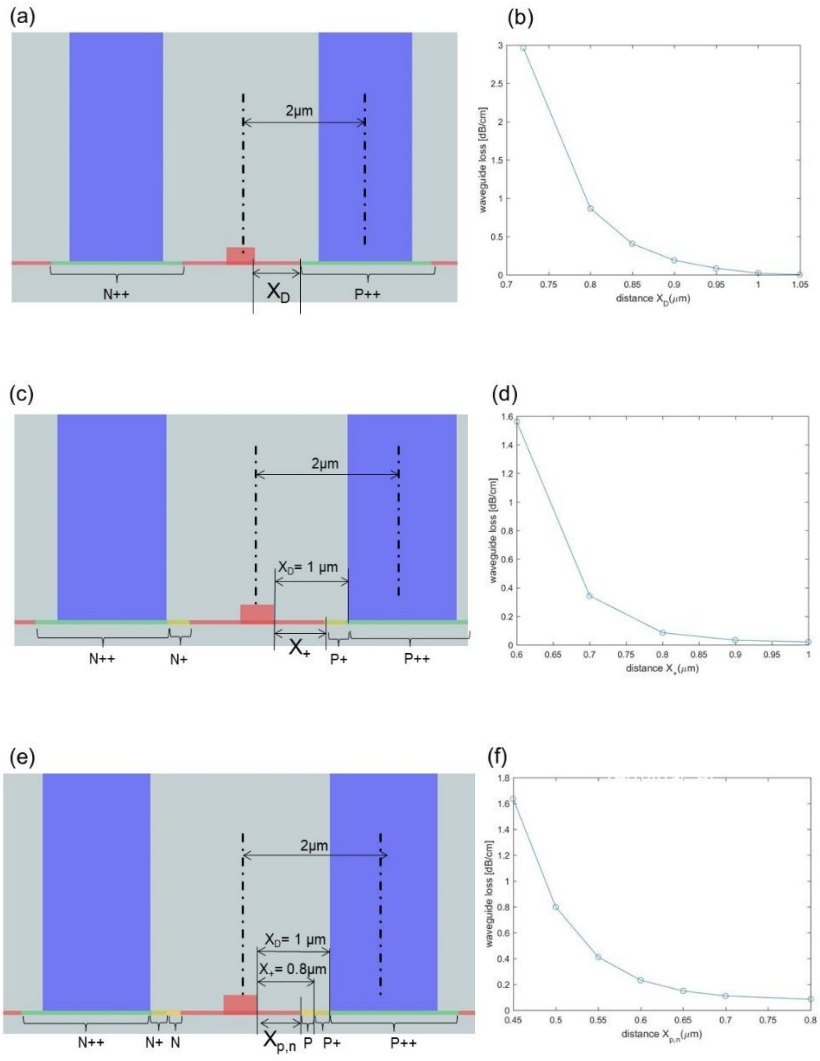

Figure 3.10 Simulation of optical loss from doping region against waveguide (a) cross section of p++/n++, (b) simulation result for (a). (c) cross section of p++/n++ and p+/n+, (d) simulation result for (c). (e) cross section of p++/n++, p+/n+, and p/n, (f) simulation result for (e).

3.2 Comb simulation

Comb simulation is based on nonlinear Schrödinger equation (NLS) with TPA induced FCA as mentioned in the former section. This section clarifies the procedure and

simulation results for optical frequency comb generation with two tone and multiple tone pump.

3.2.1 Simulation procedure

Figure 3.11 illustrates the flowchart of simulation for comb generation. First, initial parameters related to material (refractive index, carrier lifetime, etc.), structure (waveguide, etc.), and pump (power, number of pumps, etc.) are input. Then, simulator calculates the effective area A_{eff} and chromatic dispersion. Following these preparations, coupling mode theory is applied to calculate mixing in the ring. The concise description of mode coupling is described in (2.10). After the coupling, the propagation in the ring mixer is calculated with NLS equation. NLS equation is defined as (2.5). Then, the simulation program iterates these modes coupling and propagation calculation repeat until saturation of the output as a spectrum. This iteration is equivalent to the repetitive roundtrip in the ring mixer.

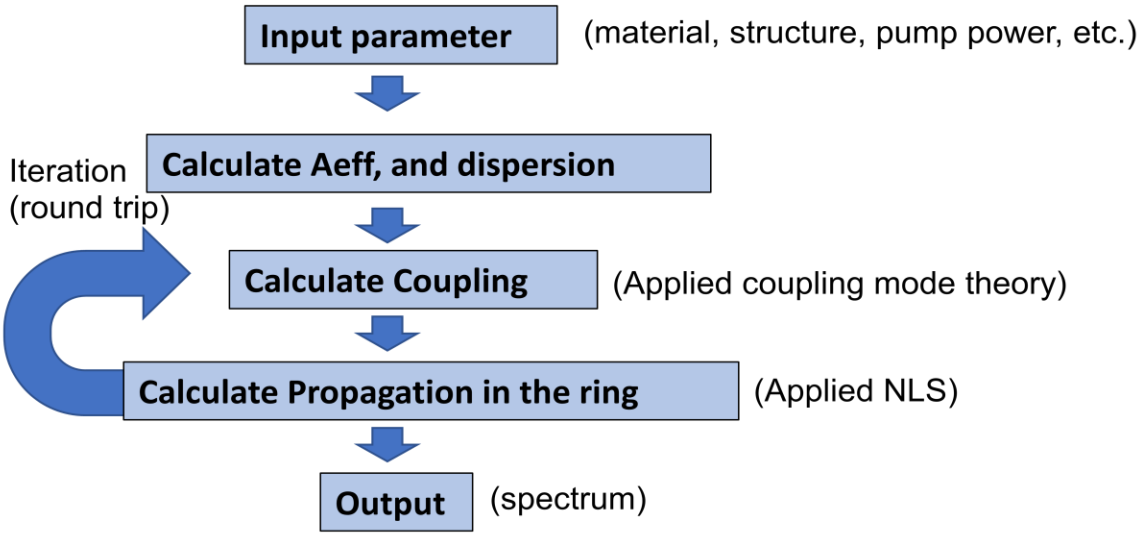

Figure 3.11 Flowchart of procedure to simulate comb generation.

3.2.2 Multiple tone pump

For multiple tone pump, the number of input tones is defined by the total peak power, because the peak power should not exceed the power to burn the coupling (>~20dBm), at the edge coupling between the fiber and silicon chip. For this reason, the number of multiple tones is fixed to sixteen tones in this dissertation. Figure 3.12 demonstrates the simulation and experimental data for the output spectrum for the designed silicon ring mixer with 16 tone pumps with different cross section. Because the difference in the nonlinear coefficient and other parameters are fixed, the output spectrum broadening is different between these output spectrums. Here nonlinear coefficient is defined as,

$$\gamma = \frac{2\pi}{\lambda}\frac{n_2}{A_{eff}}. \tag{3.9}$$

This suggests that wider width provides higher nonlinear coefficient and subsequently, high efficiency in FWM and broadband spectrum, Figure 3.12 shows comparison between measurement (Figure 3.12 (a)) and simulation (Figure 3.12 (b)). The parameters are 21dB, (input to 18dBm), and D = ~ -200(ps/nm/km). The spectrum from measurement and simulation match in bandwidth except for the input spectrum in the input tones, due to its high phase matching possibly occur in the measurement.

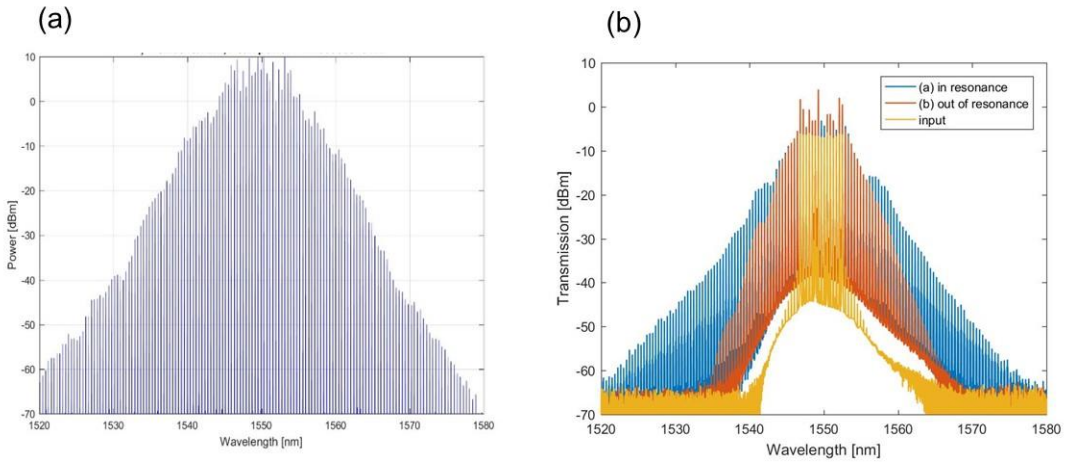

Figure 3.12 Spectrum of comb generation in different cross section to compare effect of chromatic dispersion. (a) simulation. (b) measurement

3.3 Design review and fabrication

Upon these device characterizations, the design of the silicon mixer is established and forward to the fabrication process with MPW. In this section, there is the design

review and explanation for the fabrication process based on CMOS platform for silicon photonics.

3.3.1 Design review

In the silicon photonics, device design is following the Process design kit (PDK) [36], In this thesis, PDK is processed with IPKISS based Python [37]. Figure 3.13 illustrates the design review of the silicon mixer. For the structure, it follows the discussion in the former sections. The ring is consisting of the curves and straight waveguides for the spacing. For the cross section, the distance of doping region whose width is WD, is separated enough to avoid waveguide loss originated in material loss of the dopants. The dopant concentrations are set to expect high efficiency in sweep out function for reverse bias PIN structure. Both end of bus waveguides is consisting of tapered waveguides for the coupling with tapered fiber to improve coupling loss in the system. These designs are following design rules with clearing design rule check (DRC) for foundry services.

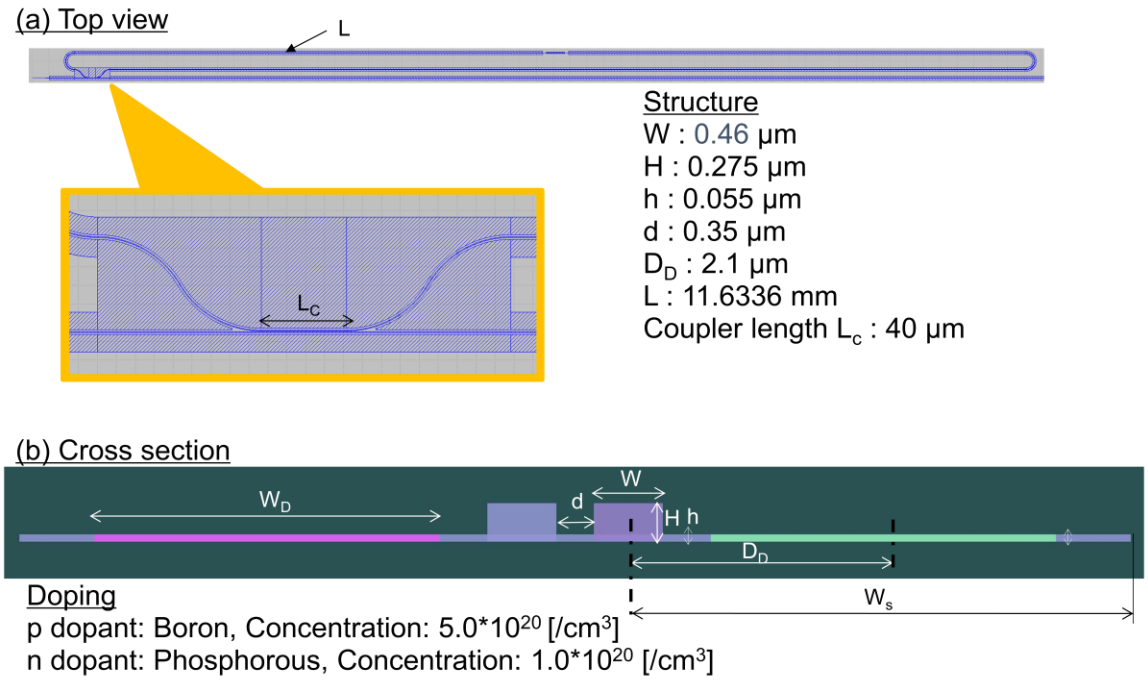

Figure 3.13 Design review for silicon ring mixer (a) Top view of the device. The expansion is for the optical directional coupler. (b) Cross section at middle of the coupler

3.3.2 Layout generation

As discussed in section 3.3.1, layout generation is processed through PDK based on IPKISS. However, the preset code does not have the components for the device in this thesis. Then, the code is developed using IPKISS to generate the devices and layers to follow manufacturing criteria in fabrication services. The developed layer generation code has multiple hierarchy, including main code for the input parameter or choose generate layers, sub code consists of specific devices such as ring mixer, and another sub code to generate specific structure, such as simple waveguide or PIN doping region. The

code also has the function to avoid violation of design rule check (DRC). The device parameters to reflect the design discussed in section 3.3.1 without violation of DRC.

3.3.3 Fabrication process

The fabrication process is compatible to CMOS fabrication process, which widely applied in the semiconductor fabrication process. Furthermore, contemporary MPW service, which fabricates multiple design on a single wafer within the same process, is prominent to slash the cost for the fabrication. In this dissertation, the devices are provided through MPW project from IMEC Singapore with drafting by process design kit (PDK). Figure 3.14 shows the layer stack in the process. On the silicon on insulator (SOI) wafer with 3 μm of buried oxide (BOX), the silicon layer is deposited. Si layer fabricated as 275nm thickness and consists of two different etching processes with 110nm etch and 220nm to characterize two levels of rib waveguides for multiple applications of photonic components (Figure 3.14 (a)). After surface oxidation for smoothing surface of silicon, especially for waveguides to decrease optical loss, SiO_2 cladding is deposited as upper cladding. For the doping region, the aluminum electrodes are built on the region fir the contact to apply voltage.

Figure 3.15 shows the Example of fabricated silicon ring mixer. In the middle of the ring, there is the heater which has the function as a phase shifter to compensate the phase mismatch in the FWM ((Figure 3.15 (a)). Figure 3.15 (b) is the cross section of the optical coupler with doped region, pictured by scanning electron microscope (SEM). The

SEM image contends that the etched gap, that potentially concerned as the origin of deviation of coupling ratio, due to the deviation of thickness.

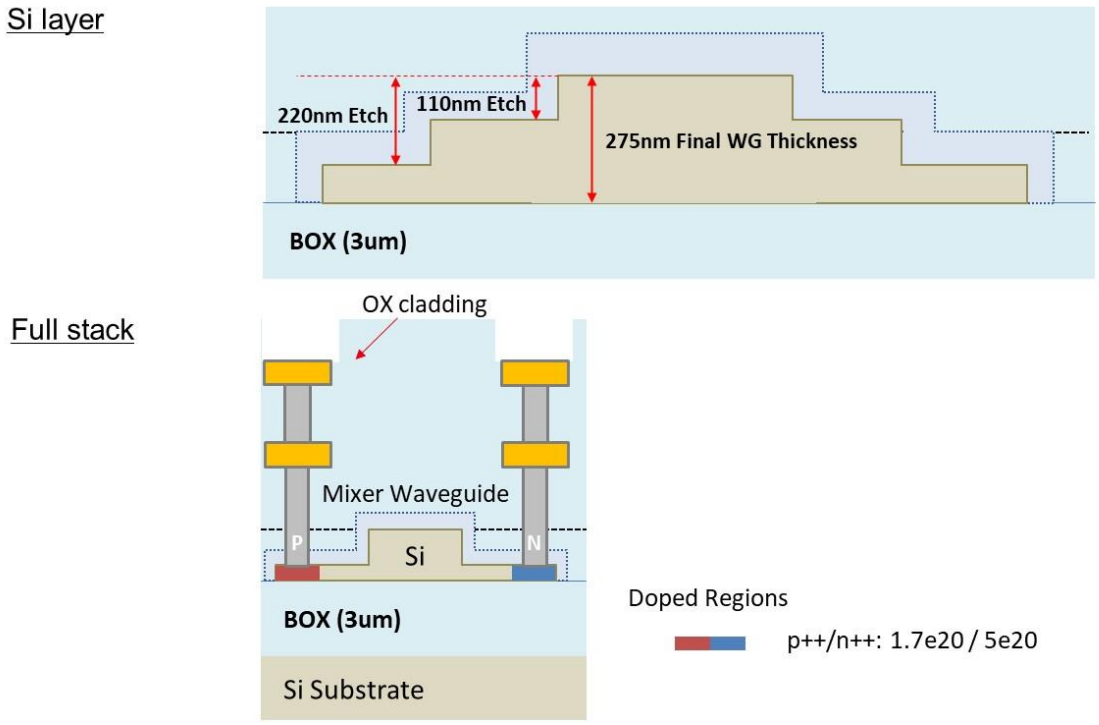

Figure 3.14 The illustration of fabrication layer for the MPW process (a) Si layer fabrication, and (b) Full stack of layer.

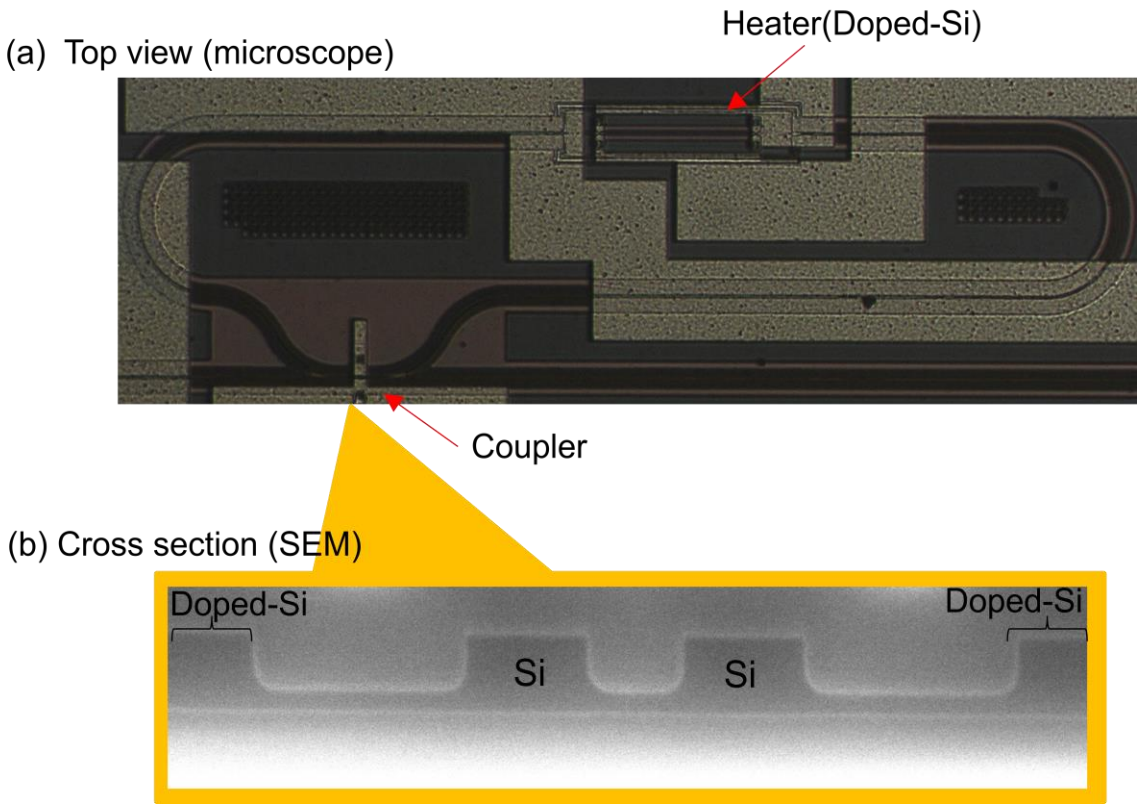

Figure 3.15 Example of fabricated silicon ring mixer. (a) Top view (b) Crosse section of the optical coupler

3.4. Device performances

Following the device fabrication, it is important to check the device performance before moving on the experiment for the comb generation. There are the demonstrations for the device characteristics including waveguide loss and FSR of the fabricated silicon mixer.

3.4.1 Overview

To optimize comb generation in the resonance of the ring for comb generation, we apply DC current with changing voltage into the heater [38]. For π phase shift, ~38 mW is required. Considering coupling loss derived in fabrication tolerance, coupling ratio of the coupler is designed for over-coupling, which is matched to critical coupling determined by round-trip loss. Within simulation, the chromatic dispersion of waveguides is engineered in normal dispersion (~ -200 ps/nm·km) at operation wavelength in our experiment (Figure 3.2 (b)), and the waveguide is quasi- single mode (QSM) to suppress higher order modes in optical spectrum for comb generation, originated in mode crossing [39]. The free spectral range (FSR) of the ring is designed for ~3.125GHz, and this design allows tolerance for phase tuning in our experiment, due to its dense spacing comparing to the frequency spacing of our 50 GHz input. We estimate the loaded Q is ~ 6.0×10^4 [40]. Because the resolution of the OSA with 20 pm (OSA20 (Yenista)), the extinction ratio may higher than that in the measured spectrum. From Figure 3.3 (c), previously, optical comb generation in low normal dispersion is investigated, despite its difficulty to occur Modulation instability (MI) comparing to anomalous dispersion scheme [38, 41, 42]. We consider that coherent two tone or multiple tone pump input enables to generate more tones than single tone input with maintaining its coherence [43].

3.4.2 Waveguide loss

Figure 3.16 shows the experimental data for total loss of the silicon waveguide by cu-off technique. Figure 3.17 shows the waveguide loss from cut back method for the waveguides. From the data, the expected waveguide loss is ~1.35dB. It is denoted that

this difference is originated in multiple factors, such as thickness of wafer, surface roughness, in fabrication processes.

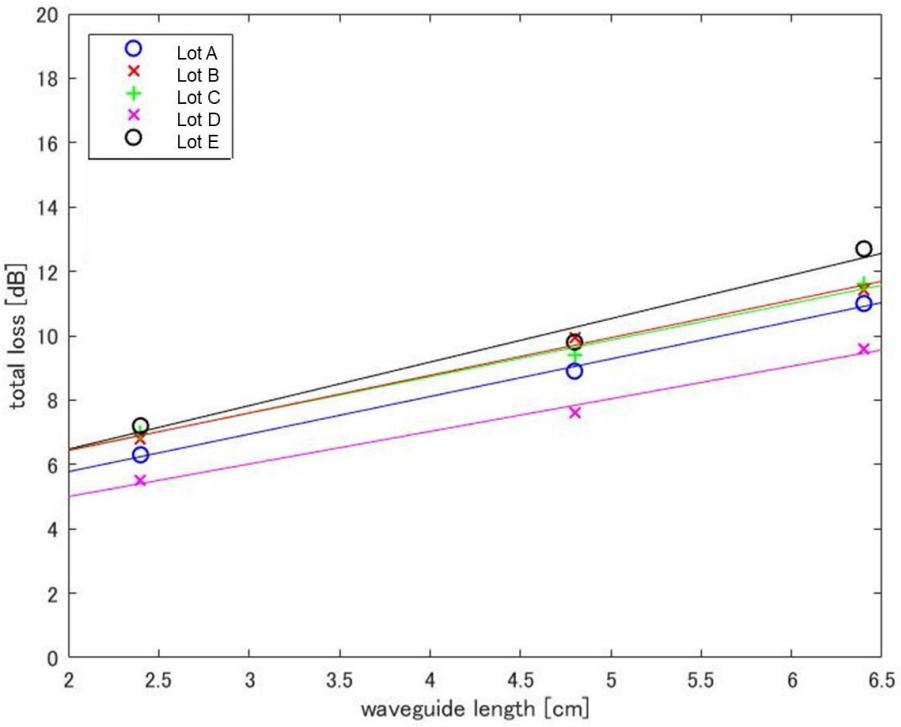

Figure 3.16 Total loss for the waveguide between different lots

Table 3.1 waveguide loss for the waveguide between different lots from Figure 3.17

	Lot A	Lot B	Lot C	Lot D	Lot E
Waveguide loss [dB/cm]	1.35	1.17	1.23	1.14	1.01

For waveguide loss, it has spectrum dependence that fluctuates along the waveguide. Fig. 3.17 illustrates a spectrum represents waveguide loss in measurement.

The measurement is proceeded with noise source in C-L band with cut-buck method. The spectrum shows fluctuation between 1.29±0.0114 with standard deviation. This fluctuation is expected to be deviation of waveguide width, due to interference between the mode from its variation along length mainly in TE mode.

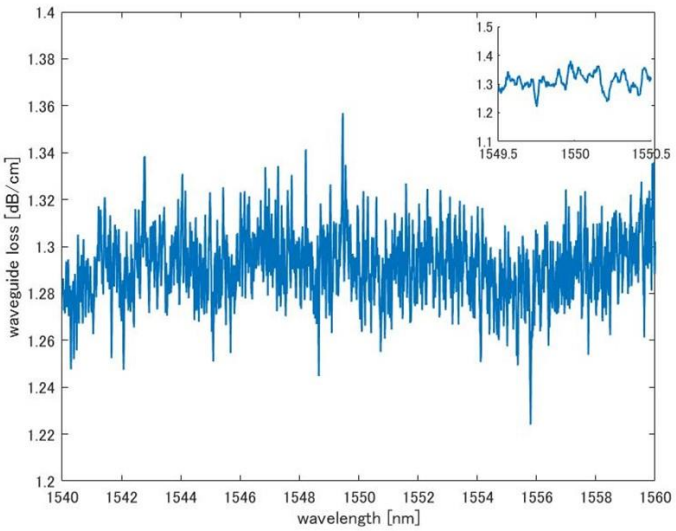

Figure 3.17 Waveguide spectrum of straight waveguide

3.4.3 Coupling ratio

As described in former section in design, coupling ratio is one of the important factors for efficient FWM in a ring mixer. Figure 3.18 and figure 3.19 show the measurement data and simulation of coupling ratio with different length of couplers between lots. In figure 3.18, coupling ratio in measurement dramatically vary between the lots. In figure 3.19, these trends in variation are similar for different length of couplers. To investigate these variations against the simulation, it is expected to be

originated in variation of fabrication, especially thickness of wafer and slab. Figure 3.20 and figure 3.21 show the simulation results with considering variation of thickness of wafer (i.e., waveguide thickness H) or/and slab h. The simulation shows even 10% variations in these parameters are enough to cause difference of coupling ratio, and this number is potentially reasonable to be exist in the fabrication processes.

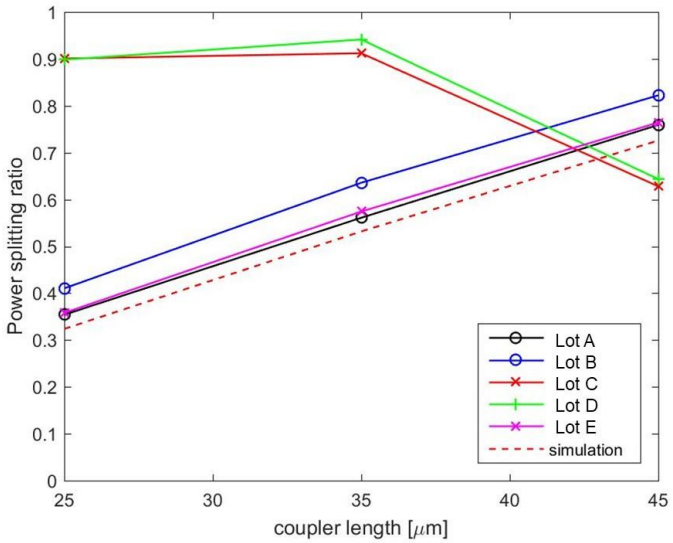

Figure 3.18 Coupling ratio for the waveguide between different lots

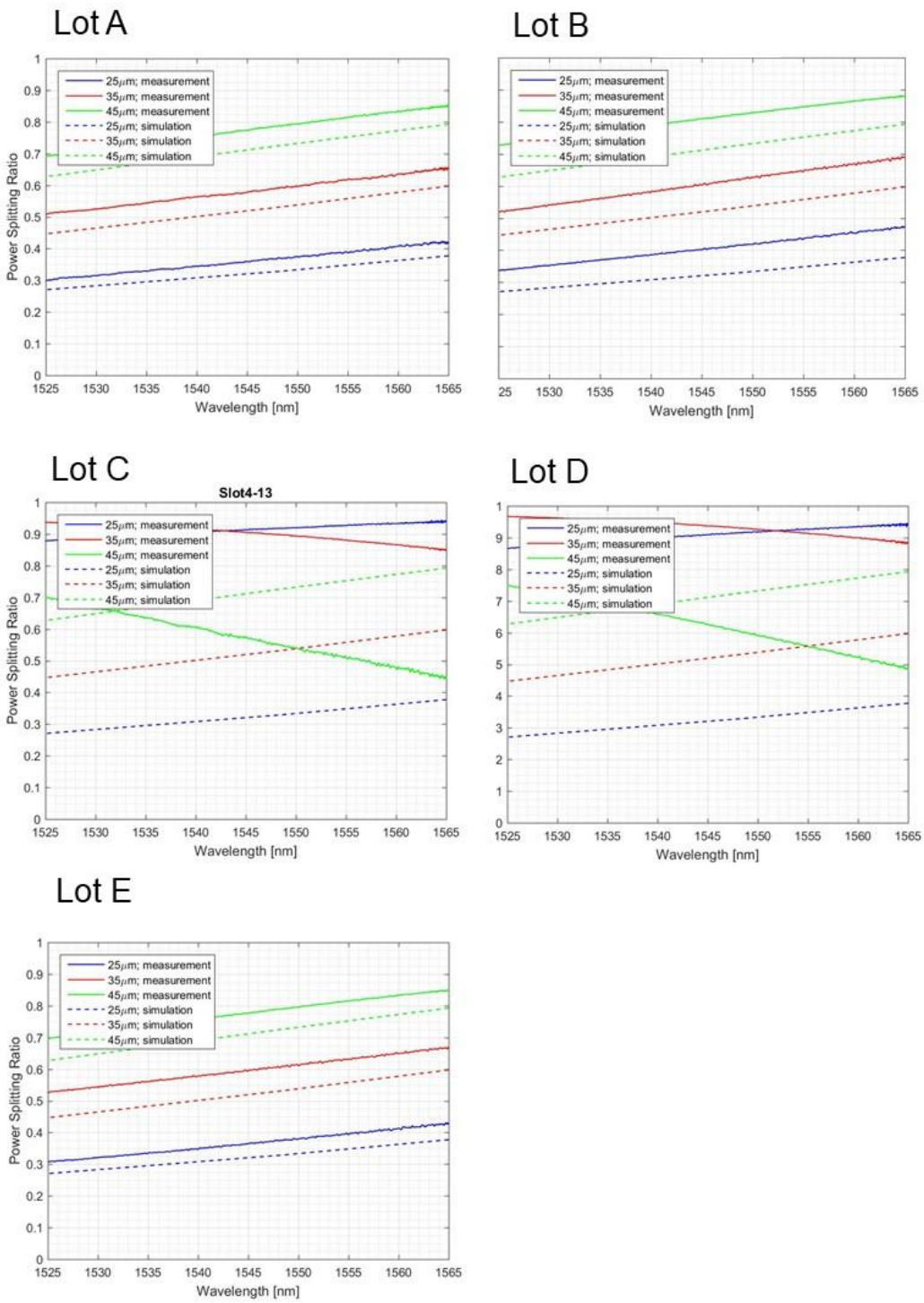

Figure 3.19 Measurement and simulation data of coupling ratio between different lots

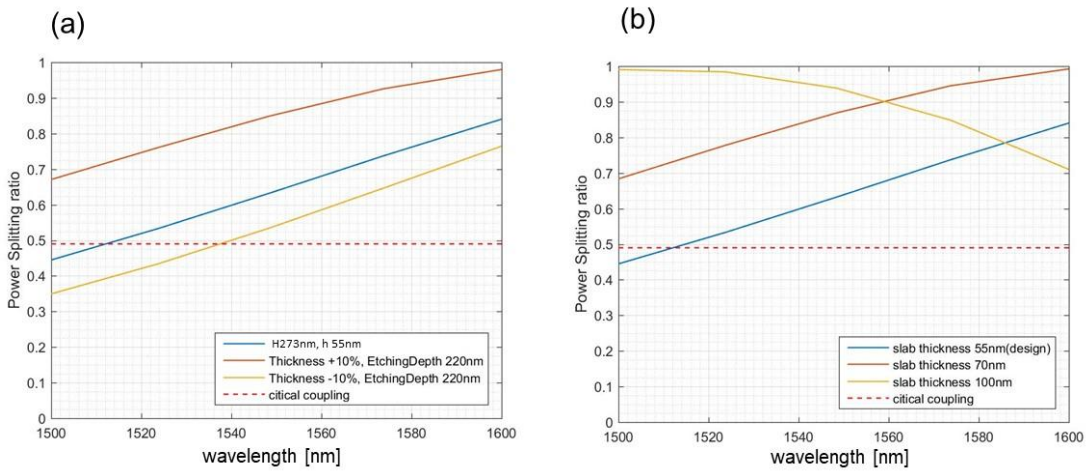

Figure 3.20 Simulation data of coupling ratio considering variation of thickness of wafer or slab. (a) simulation considering thickness of wafer (b) simulation considering thickness of slab

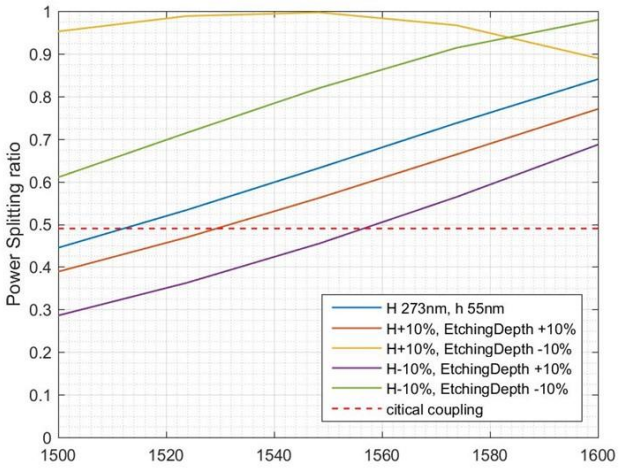

Figure 3.21 Simulation data of coupling ratio considering variation of thickness of wafer and slab.

3.4.4 FSR

Figure 3.22 demonstrates the transmission and FSR from the experiment. (a) shows the transmission and the inset shows the selected band for precise inspection. From

this data, it reveals that the extinction ratio is 1.5dB. However, due to the resolution of the OSA, it is possibly not clarifying the exact extinction ratio. For the extinction ratio, there is another experiment in the later chapter with the experiment for comb generation. (b) shows the FSR of the mixer with comparison for the simulation. In both experimentally and theoretically, the FSR is calculated as,

$$FSR = \frac{\lambda^2}{n_g \bullet L}. \tag{3.10}$$

where, n_g : 4.1186, and length of ring as L : 11.6336 mm. Then, the Figure 3.22(c) illustrates the FSR matches between simulation and experiment, and the simulation shows the trend that the FSR increases gradually along the wavelength due to the nonlinearity in group index. For the experiment, resolution of OSA is 0.02 nm.

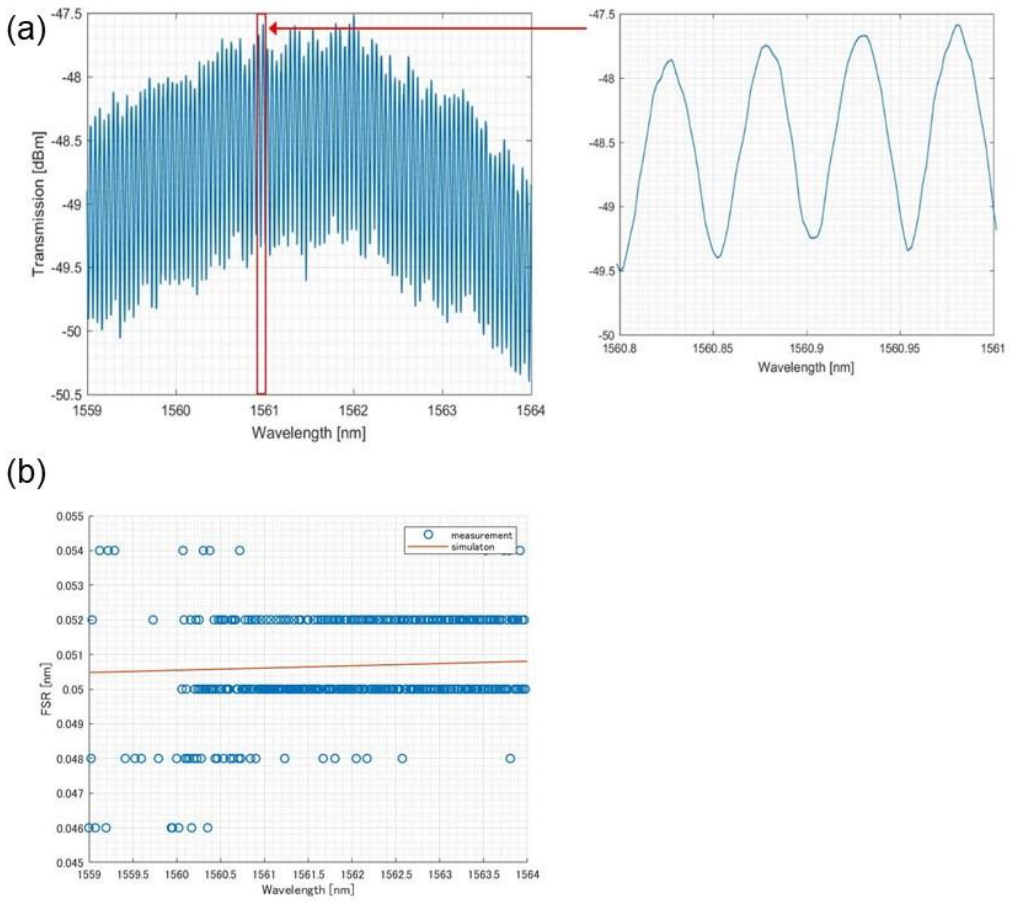

Figure 3.22 Experimental data for the transmission and FSR of the ring mixer. (a)Transmission, (b) FSR with comparison with simulation.

3.4.5 Q factor

From resonance in the spectrum (Figure 3.23), Q factor is calculated from and (2.14) as $Q \sim 5.9 \cdot 10^4$. Due to its dense FSR, resolution is of OSA in this measurement is set as 2pm. FWHM for resonance wavelength is picked for calculation.

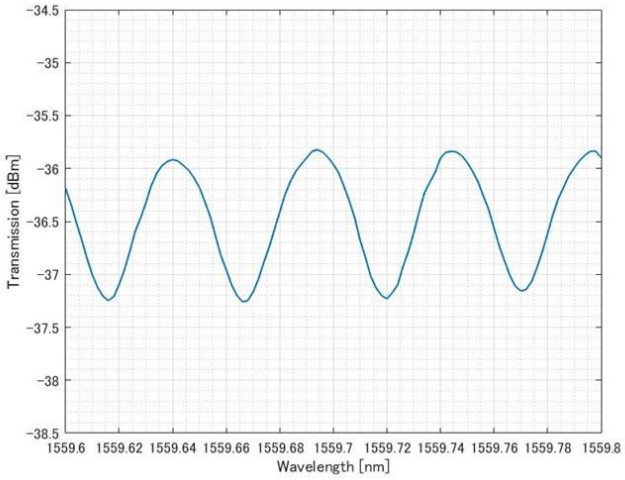

Figure 3.23 Resonance spectrum from silicon ring mixer. Resolution of OSA is 2pm.

3.5 Chapter summary

In this chapter, device parameters are evaluated for FWM in the ring mixer. The discussed characteristics are chromatic dispersion, length of the ring to define FSR, coupling ratio for phase matching, and PIN structure to minimize the penalty nonlinear loss from TPA effect. Comb simulation is also demonstrated based on the evaluated characterization.

Design review and fabrication is also discussed including fabrication process with silicon CMOS process, and fabricated device is evaluated experimentally to verify its performance is following the design that discussed above to achieve FWM in ring mixer demonstrated later next chapters.

Chapter 3, in part, is currently being prepared for submission for publication of the material. Motohiko Eto, Bill Ping-Piu Kuo, and Stojan Radic. The dissertation author was the primary investigator and author of this material.

Chapter 4

Frequency comb generation in silicon ring mixer

Consequent to device characterization in chapter 3, we demonstrate four wave mixing in the silicon ring mixer. As a system to generate frequency comb with silicon ring mixer, the system is composed with an input source with multiple tones and a tuning stage for silicon ring mixer. In this chapter, first, the principle of comb generation with multiple tone pump with silicon ring mixer is explained. Then the setup and procedure to achieve the concept is demonstrated. Accordingly, the experimental results of multiple tone inputs are shown.

4.1 Introduction

Optical frequency comb in telecommunication band is developed by mode locked lasers, electro optic modulation, and four photons mixing (FPM) using ring resonators. In the previous work for high Q-factor ring resonators with based four photon mixing, most of them are studied for silicon nitride (SiN), or silica [44-47]. As an application for coherent communications [48-49], frequency comb generation with FPM on silicon-based ring resonators in telecommunication band is highly desired, due to its compatibility to complementary metal-oxide-semiconductor (CMOS) process. However, optical loss derived from strong free carrier absorption (FCA) originated in two photon absorption (TPA) in telecommunication band prevents its application from comb generation except for infrared region [50-52]. Recently, comb generation in a silicon ring

resonator modulator was studied, but its mechanism is based on electro-optic modulation in a silicon ring modulator [53].

4.2 Principle of comb generation with multiple tone pump with silicon ring mixer

The principle of comb generation is based on FWM, and inherently, it is possible to generate comb from the single tone, such a case is demonstrated in other references. However, for silicon, due to its lower nonlinear coefficient and TPA inhibits efficient comb generation and few tones via silicon modulator in PIC technology, comparing to SiN ring mixer which shown as a successful example even generated an octave bandwidth including telecommunication band. From these points of view, we apply multiple tone as an input source for the silicon ring mixer.

Figure 4.1 illustrates the principle of multiple tone pump. For the concise and intuitive investigation, in this case, the number of inputs is two with separation of Δf on frequency, which is not necessarily equal to FSR, but multiple of FSR of the ring mixer. In the following, the process is explained through (1) to (5).

(1) Input wave travels in the waveguide.
(2) Partial power couples into the ring according to the coupling ratio in the coupler, and the spitted waves travel in the bus waveguide and the ring.
(3) For the wave propagation in the ring, and sidebands are generated by FWM in a single trip in the ring.
(4) Remained power propagates in ring, and cascade FWM generates other sidebands in the ring in the second trip and after.

(5) After enough times of trip, the output spectrum is stable.

For broadband comb generation in this scheme, the setup for multiple tone input and silicon ring mixer with high conversion efficiency are the critical factors. For the following sections, there are the illustrations for the setup and for the silicon ring mixer, its characteristic is already discussed in the former chapters and its conversion efficiency is demonstrated experimentally in this chapter.

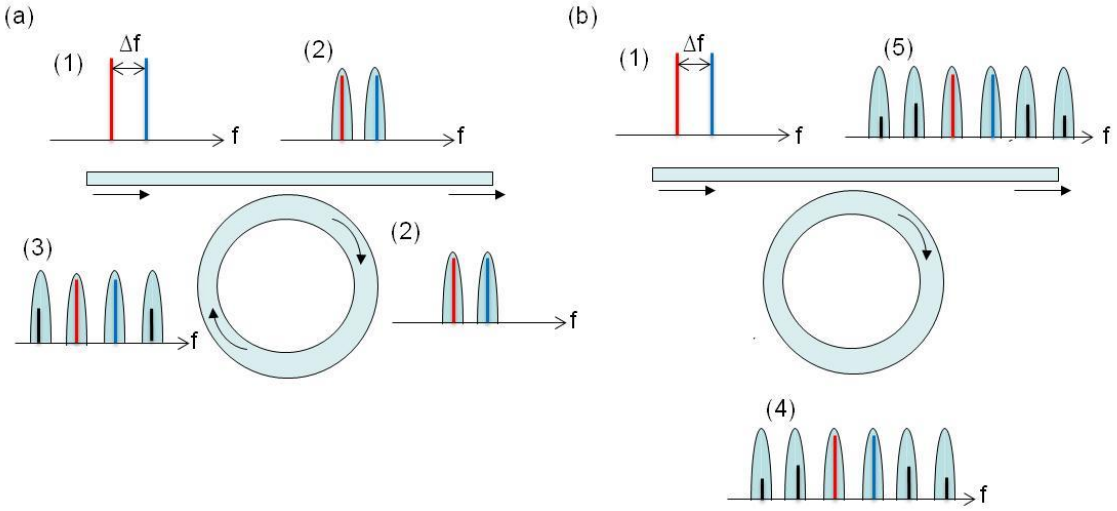

Figure 4.1 Principle of multiple tone pump (a) first round trip, and (b) after first trip

Here, we demonstrate infrared frequency comb in the wavelength between ~1,530-1,570 nm based on a single silicon ring. The initial input is a single continuous wave (CW) laser centered around 1,550 nm, and it generates multiple tones through the two cascaded phase modulators (PM) with phase tuning [54]. The generated tones are filtered with 50 GHz spacing and pulse shaped with spectral processor based on liquid crystal on

silicon (LCoS) chip. Si waveguides have optical loss originated in TPA in telecommunication band, hence we designed p-i-n junction for the waveguide with applying reversed bias to sweep generated free carriers to reduce this optical loss [55]. In the silicon ring resonator, multiple-tone mixing process generates multiple seed tones and maintain energy conservation due to degenerate FPM process [44,56-58]. Figure 4.2 shows the concept of frequency comb generation. For two tone input as simplified case in multiple -tone input, these two input tones, generated with frequency spacing Δ, couple into the ring resonator. Afterwards, output from the ring resonator shows multiple tones with maintaining its spacing as Δ. The two-tone input into the ring resonator for comb generation is studied recently using two isolated tunable lasers [59], or single tunable laser with PM [60]. Besides, varying FSR spacing with integer of FSR of ring is investigated, as our measurement [61]. For these two-tone inputs, the nondegenerate FPM occurs and generate sublines (Figure 4.1 (a)).

$$2\omega_{1-,1+} \longrightarrow \omega_{2-,2+} + \omega_{1+,1-} \tag{4.1}$$

For multiple tone input, the generated tones with frequency spacing Δ also shows the output spectrum through the mixing with same spacing in the ring resonator. For 2N seed photons ($\omega_{N-,\,N+}$, $\omega_{(N-1)-,\,(N-1)+}$, …, $\omega_{1-,\,1+}$) are obliterated to generated frequency tones as two tone input. We believe that these multiple tone input occurs more FPM interaction around center wavelength and generates more sublines as output spectrum (Figure 4.2(b)).

$$2\Sigma\omega_{n-,n+} \longrightarrow \omega_{N-,N+} + 2\omega_{(N-1)-,(N-1)+} + \cdots + \omega_{1+,1-} \tag{4.2}$$

For the multiple tone input, its phase noise affects to the efficiency of the FPM process and output spectrum than two tone input. Accordingly, to maximize generated tones and

their optical signal to noise ratio (OSNR) in the output spectrum, it is important to maintain its coherence by optimization of the phase of each tone to shape high peak power pulse train in the setup, such as spectral processor.

(a) (b)

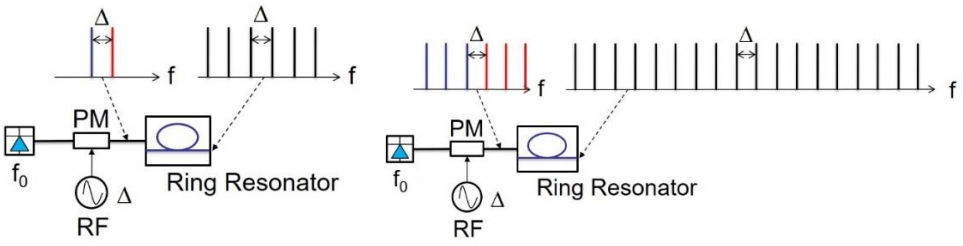

Figure 4.2 FWM for comb generation, with multiple tones. (a) Two tone input. (b) Multiple tones input)

4.3 Setup and procedure

Following the principle discussed in the last section, this section describes the setup and procedure for the multiple tone input with silicon mixer. The key components for the system are the cascaded phase modulators and programmable optical processor to generate coherent and flat-top multiple tone input. For the procedure, the tuning is started from single pump to multiple pumps with meticulous tuning for phase and flat-peak power for the input tones. In addition, for the silicon mixer, phase tuning via heater is also critical for phase-matching in the efficient conversion.

4.3.1 Setup

Figure 4.3 illustrates the experimental setup for multiple tone with silicon mixer. Figure 4.3 (a) shows setup schematics. The tunable laser operated in c-band at λ_0 = 1550nm. The output is optimized polarization to gain maximum power by a polarization controller (PC), and the output is into the cascaded phase modulator consists of Mach Zehnder modulator (MZM) with RF clock whose signal input is ~25GHz, to generate multiple tones. Then, the preamplifier consists of erbium doped fiber amplifier (EDFA). The output from the pre-amplifier is attenuated with variable optical attenuator (VOA), and input into the programmable optical processor (POS) (waveshaper, (Finisar)), for the filtering and tuning phase and peak power of generated tones. Then, the output is amplified with polarization maintained (PM) amplifier and filtered in band-pass filter (BF) to pass the input tones into the chip. Before the input couples into the silicon ring mixer with tapered fiber, its polarization is optimized by another PC. On the silicon mixer chip, the electrodes are contacted to operate the reverse bias PIN structure and heater which has the function as a phase shifter in the operation (Figure 4.3 (c)).

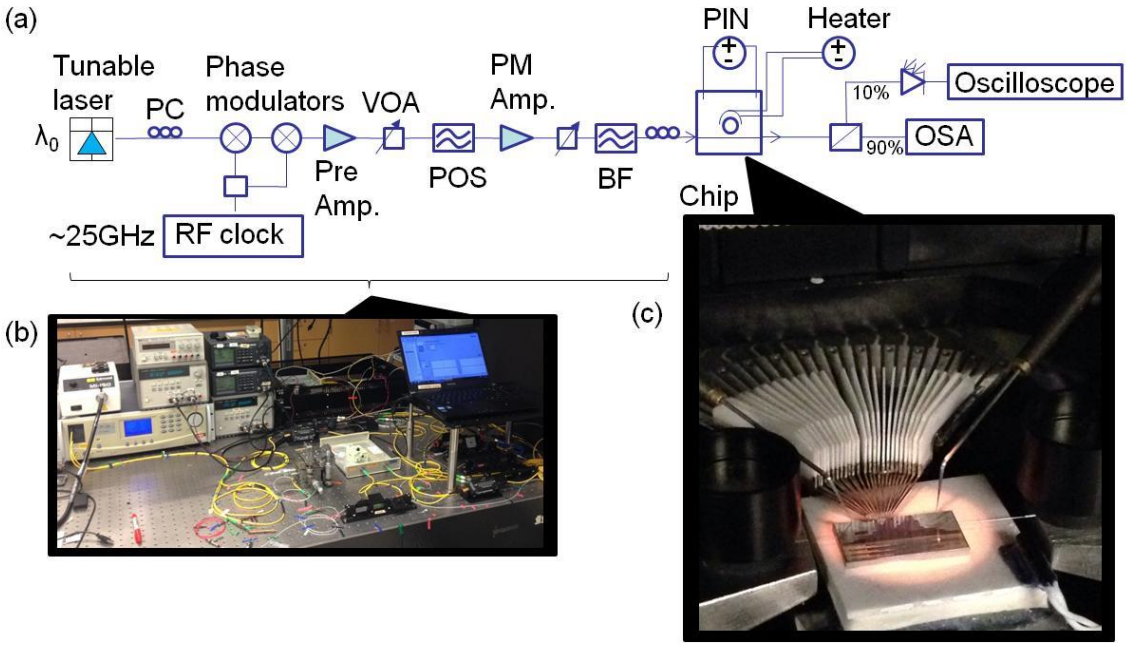

Figure 4.3 Experimental setup for multiple tone with silicon mixer. (a) Setup schematics, (b) picture of the setup, (c) picture of the silicon mixer on the stage with electrode probe for PIN and heater

4.3.2 Procedure

With the setup, the procedure to generate frequency comb is implemented. Figure 4.4 illustrates the procedure for multiple pumps with the setup. First, the single pump is introduced to study the resonance frequency of the ring mixer with tuning the frequency around c band. Also, this single pump experiment has the purpose to investigate extinction ratio of the ring mixer, which is difficult to investigate through transmission discussed in Section 3.4.2. Then, FWM with two pump waves are investigated to show the elemental experiment to analyze the conversion efficiency of FWM. In this two-tone pump scheme, it is important to achieve flat peak and coherent phase by optimization

thorough the POS, to generate bilateral symmetrical output spectrum. For the device side, the heater has the function as a phase shifter and tuned for the phase-matching in the FWM in the ring mixer. After these tuning, RF frequency is optimized to achieve most efficient FWM, until output spectrum is broadest and shows highest signal to noise ratio (SNR). Finally, the multiple tone pump with 16 tones is applied to generate broadband comb in the c-band. For the multiple tone pump, its procedure is similar to the two tone, pump. However, increased number of tones make the tuning of coherence and peaks of the input tones, accordingly it demands precise tuning optimization to achieve high efficiency FWM.

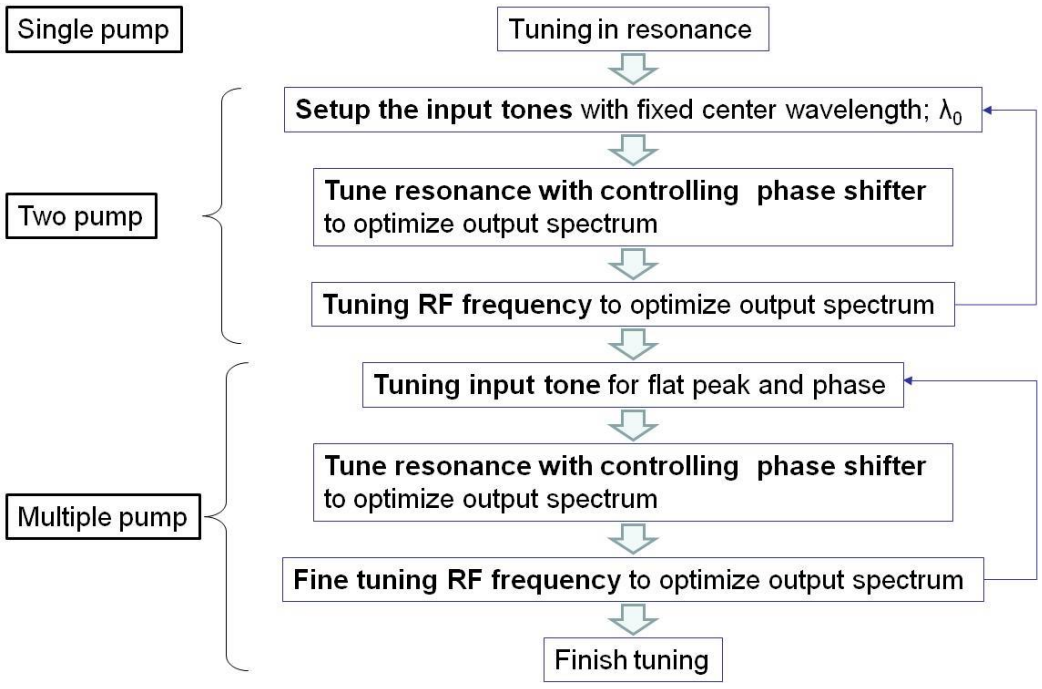

Figure 4.4 Procedure for multiple pump

4.4 Experimental demonstration: Single pump

Figure 4.5 shows example of spectrum of single pump. In this case, the center wavelength is set on ~1561.5nm, in a c-band, with sweeping of wavelength and meticulous tuning of phase shifter on the silicon ring mixer. Due to this tuning, the ring mixer shows the 2dB as an extinction ratio, between the resonance and out of the resonance. In addition, the electrical current in the TPA structure in the silicon ring mixer is simultaneously measured in the experiment, and it demonstrates the increment from out of resonance at 4.0mA to the resonance at 5.3mA. This indicates that the ring mixer is in the resonance that increases the energy circulating the ring. Then, this resonance will contribute the more effective FWM in the ring mixer to generate more tones with high SNR with two pump or multiple pumps discussed in the later sections.

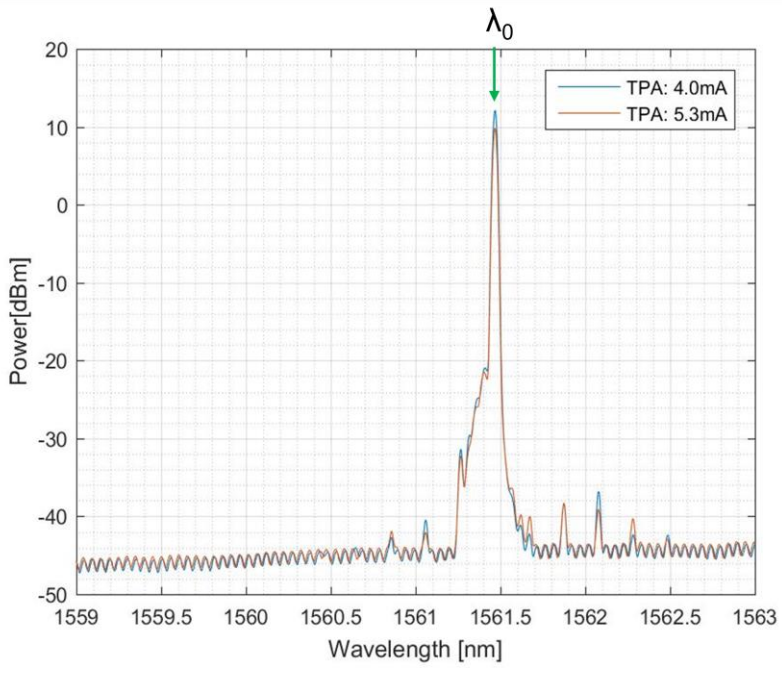

Figure 4.5 Example of spectrum of single pump

4.5 Experimental demonstration: Two pump

Upon the single pump measurement, the two-pump measurement is executed with the procedure discussed in the former sections. Figure 4.6 and Figure 4.7 show the spectrums for the two pumps in different condition of the input source. Figure 4.6 is the comparison of different RF frequency for the cascaded phase modulators. The conversion efficiency, that the difference between the peaks between the two input tones and generated tones as sidebands, is highest as ~14dB at 25.255GHz of RF frequency (Figure 4.6 (b)). For comparison, the conversion efficiency is lower in the other condition that is ~17dB at 25.225GHz of RF frequency (Figure 4.6 (a)) or ~18dB at 25.275GHz of RF frequency (Figure 4.6 (c)). This indicates that the FWM can be shown in each RF frequency, because of the FSR of the ring mixer is less than the separation of the two input tones. However, it is necessary to precise RF tuning to achieve high conversion efficiency in the FWM. Figure 4.7 demonstrates the comparison between different FSR separations of the two pumps. In these figures, the conversion efficiency is highest in the 2FSR ((Figure 4.7 (b)). However, the difference is ~0.1 dB in the other cases that 4FSR ((Figure 4.7 (a)) and 5FSR ((Figure 4.7 (c)). This suggests the separation of the pump is precisely controllable with resolution of its FSR in this silicon ring mixer because this scheme uses the multi FSR with the ring with finer FSR than the operation frequency. This is the unique approach from the other references shown in the comb generation from a ring mixer, which the frequency of the comb is inherently defined as the length of the ring.

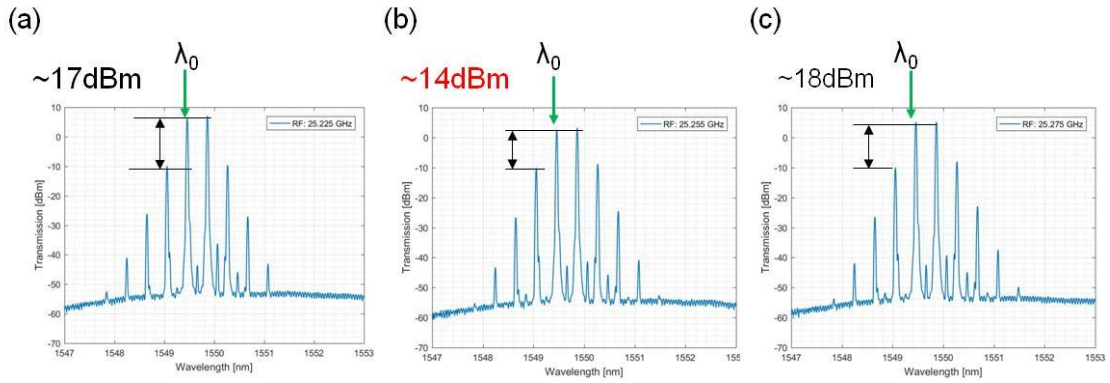

Figure 4.6 Spectrum of two pump with different RF frequency (a) RF: 25.225GHz with conversion efficiency of 14dB (b) RF: 25.255GHz with conversion efficiency of 17dB, and (c) RF: 25.275GHz with conversion efficiency of 18dB

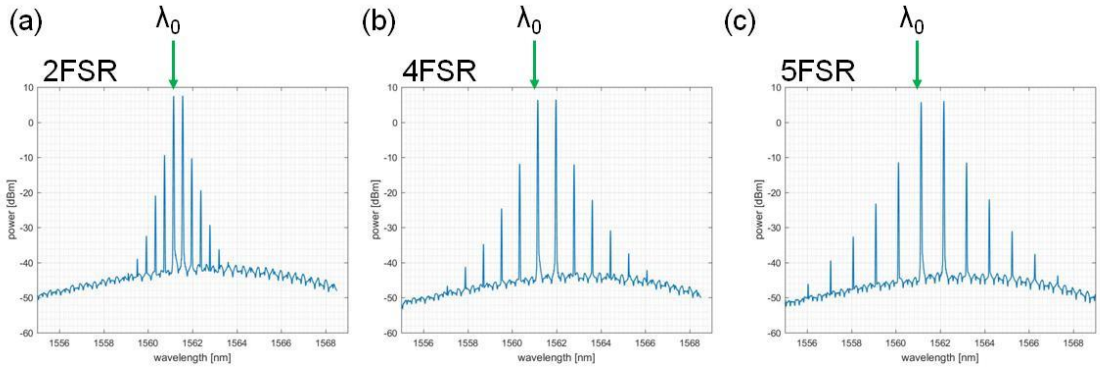

Figure 4.7 Spectrum of two pump with different FSR separation of pump (a) 2FSR, (b) 4FSR, and (c) 5FSR

Conversion efficiency is 14dBm for 2FSR and its difference between the measurement is

0.1dB

4.6 Experimental demonstration: Multiple pump

For multiple pumps, it is based on the tuning condition of two pump discussed in the former section. Due to increase of the number of the tones, the system needs POS to control not only the phase and peak, but also the number of tones with its capability of arbitral filtering. In this dissertation, the procedure to tune the input tones starts from the control number of tones by POS, and tuning phase a amplitude o the controlled number of tones are executed. Figure 4.8 illustrates the filtering of tones from 30 tones (Figure 4.8 (a)) to 15 tones (Figure 4.8 (b)) that POS filters the tones every other. Simultaneously, it changes the frequency of the wave from ~25GHz that original frequency of 30 tones, to ~50GHz that the frequency of filtered 15 tones, by this filtering. Further, from this filtering, the amplitude and phase of the wave is alternated, and those should be tuned after this filtering.

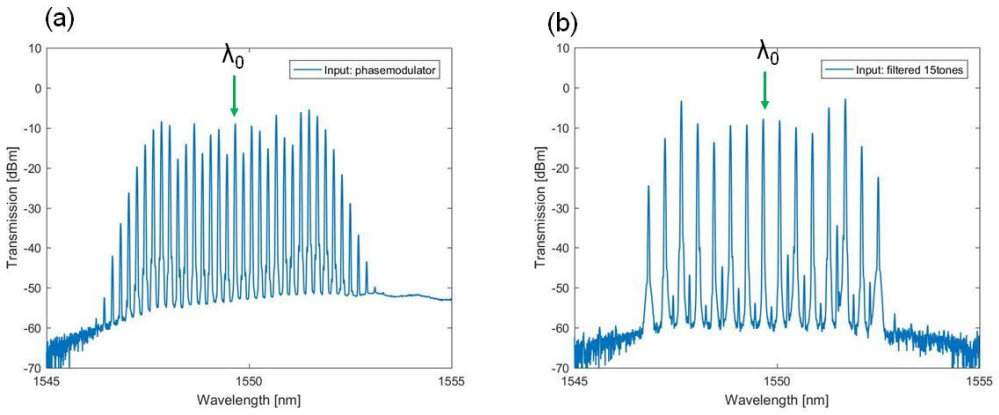

Figure 4.8 Example of filtering input tones by POS (a) 30 tones before filtering ~25GHz for spacing, (b) 15 tones after filtering for ~50GHz spacing

Filtering for the 15 tones follows the filtering number of tones. In this filtering, the amplitude and phase are optimized precisely for efficient FWM in the ring mixer. First,

the peak power is set to the same level those deviation is kept less than 2dB. Figure 4.8 shows the result of the tuning. This tuning will contribute the generation of the tones in the FWM in the ring with smooth gradient peaks. In addition, phase tuning of the input tones is executed dedicatedly. Figure 4.9 shows its comparison before/after of the phase tuning. As its mentioned, after the phase tuning, sidebands are generated next to the original 15 tones by improved phase-matching of the input tones. Further, its shape is smoothly graduated by well controlled peak power.

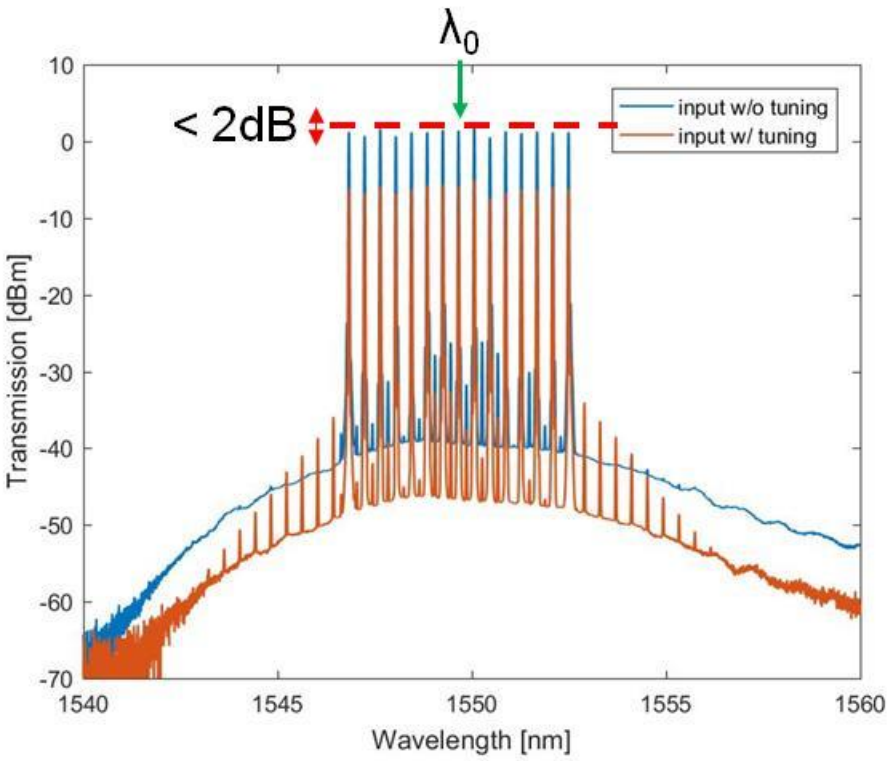

Figure 4.9 Example of filtering of input tones for 15 tones with 50GHz, with comparison before/after phase tuning. The deviation of peak is suppressed less than 2dB, and its sidebands are generated by phase-by-phase tuning.

Upon the tuning of input wave, tuning on the silicon mixer is implemented. For the silicon mixer, its tuning procedure is same as before discussed the former section. In this multiple tone scheme, the input power is high (>20dBm), and the increase of tones have a possible to burn the coupling between the tapered fiber from the input setup and the tapered waveguide for the silicon ring mixer. Then mediate optimization of the coupling and gradual increase of the input power until the target is necessarily in the experiment. Figure 4.10 demonstrates the result of output spectrum from the silicon ring mixer. For comparison, the output spectrums for the input, output without resonance (i.e., out of phase), and output within resonance (i.e., in phase), are plot in the figure. Even if the ring mixer is in the state without resonance, due to its fine FSR comparing to the spacing of input, smooth and broadband sidebands are generated besides the input tones (Figure 4.9(b)). However, the spectrum in the resonance generates further broadband spectrum due to the phase-matching in the silicon ring mixer (Figure 4.9(b)). The number of generated tones counts about eighty tones in the resonance state. The generated comb is stable in the minimum alignment of the phase tuning in case of the system is stable, such as the coupling between the fiber and the chip. For monitoring resonance mode of the ring, current from PIN structure (TPA current) is investigated. Typically, TPA current shows ~10mA with digital multimeter at out of resonance, and it increases with tuning into the resonance mode until ~15mA in the ring mixer. It is denoted that these TPA current can be varied from various factors, both device and experiment; for device characteristics, PIN structure, coupling loss of the chip, coupling ratio can be the factors, and for experiment, input power, pulse compression of the input tones can vary the TPA current.

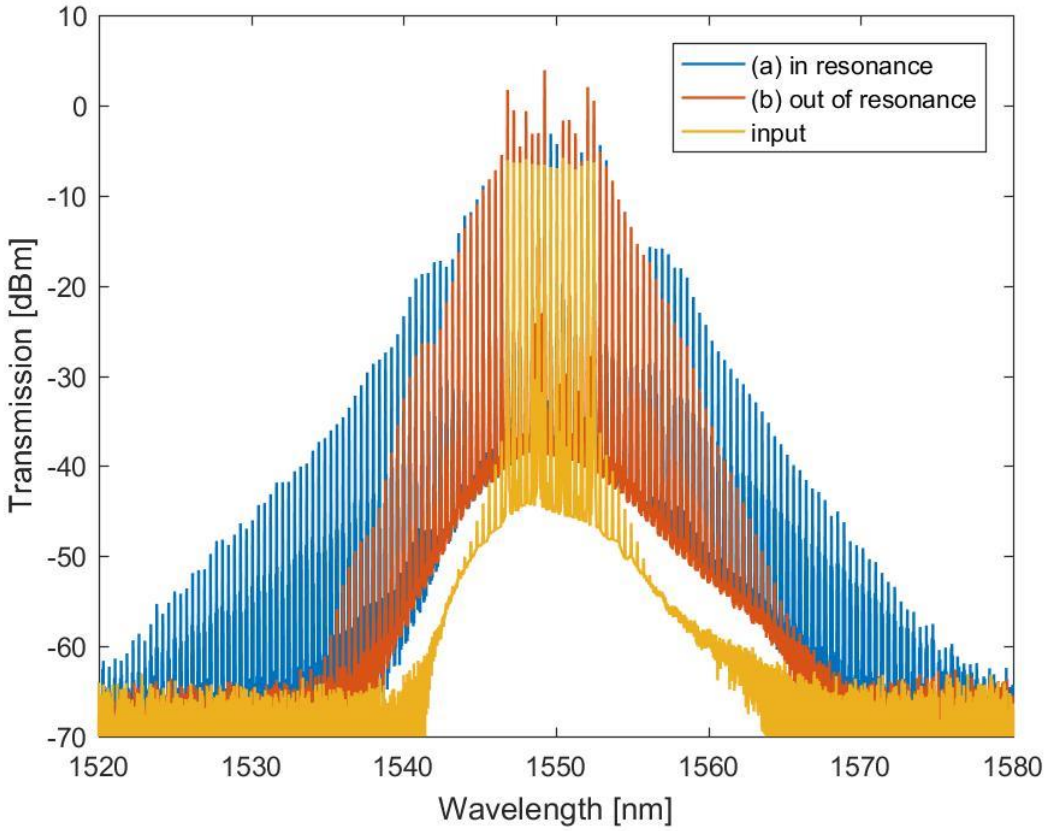

Figure 4.10 Output spectrum of the silicon mixer. The tuning condition is input power is 21dBm, RF frequency is 25.250GHz (i.e., Output frequency is 50.5GHz), and center frequency is 1549.4420nm.

For the further inspection on the condition of the comb generation, the comparison between different RF frequencies is investigated. Figure 4.11 shows the result of the experiment between the RF frequency from 25.217GHz and 25.275GHz. Again, the actual frequency of the output is doubled, because of the filtering from POS. In addition, for each frequency, the phase is tuned for optimization to gain highest efficiency in the FWM in the ring mixer. From this experiment, the frequency at 25.250 GHz and 25.255

GHz is gain highest efficiency in this scheme (Figure 4.11 (b), and (c)). This suggests that the phase matches well around the wavelength close to the input tones. Then the generated sidebands by FWM nearby the input contribute the generation of other sidebands apart from the input wavelengths. Then, these frequencies tell the optimized frequency to generate smooth and symmetrical comb that we targeted. For comparison, Figure 4.11 (a) shows the result in the lower frequency than optimized frequency. As it is shown, SNR of generated combs are higher in the shorter wavelengths than the longer ones. This indicates that the phase is matched in those shorter wavelengths and causes high efficiency in FWM, and vice versa in the longer wavelengths. This is considered to the dependence on frequency/wavelength for coupling ratio of the ring mixer. In the directional coupler for our silicon ring mixer, it inherently has frequency/wavelength dependence due to the nonlinearity of group index. Then, the dependence causes frequency/wavelength dependence on the phase matching condition, and efficiency of FWM. Figure 4.11(d) shows the lowest FWM efficiency in this figure. This indicates that the ring mixer has low phase-matching (i.e., out of resonance) around center frequency, and generates a few sidebands. As a result, it cannot other sidebands.

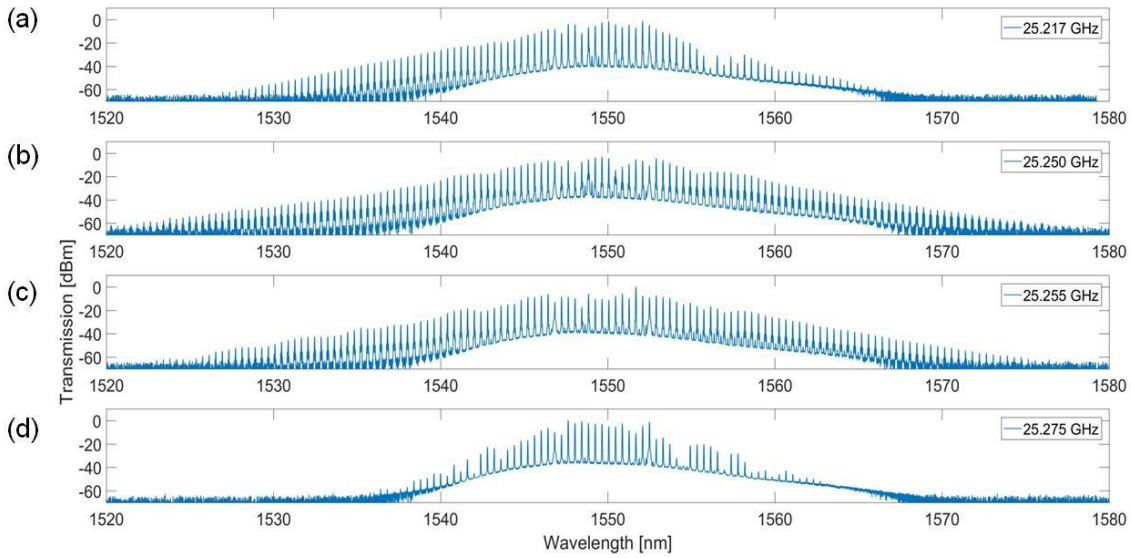

Figure 4.11 Comparison of different RF frequency for comb generation. (a) RF: 25.217GHz, (a) RF: 25.250GHz, (c) RF: 25.255GHz, and (d) RF: 25.275GHz.

4.7 Chapter summary

In this chapter, FWM in the ring resonator is experimentally demonstrated from single pump to multiple pump that 15 tones is a maximum. The chapter begin with the discussion of procedure and setup of the experiment to achieve tuned input peaks with a high power (~20dBm), coupled to the chip discussed in chapter 3. Due to diligent tuning of the input of the peaks, phases, and RF frequencies for input tones, plus tuning on the phase shifter fabricated in the ring, broadband spectrum is achieved between 1520 and 1580 nm at -65dBm noise floor.

Chapter 4, in part, is currently being prepared for submission for publication of the material. Motohiko Eto, Bill Ping-Piu Kuo, and Stojan Radic. The dissertation author was the primary investigator and author of this material.

Chapter 5

Dispersion dependence of comb generation

Chromatic dispersion measurement has an importance in the photonics system consists of not only optical fibers but also the silicon photonics for applications, such as telecommunications. In case of the optical communication system, chromatic dispersion affects the distortion of the optical pulse due to its chromatic dispersion. In the other case, such as silicon photonics, chromatic dispersion affects the nonlinear phenomena, such as four wave mixing (FWM), because of its contribution to phase matching condition.

5.1 Introduction

Chromatic dispersion measurement has an importance in the photonics system consists of not only optical fibers but also the silicon photonics for applications, such as telecommunications. In case of the optical communication system, chromatic dispersion affects the distortion of the optical pulse due to its chromatic dispersion. In the other case, such as silicon photonics, chromatic dispersion affects the nonlinear phenomena, such as four wave mixing (FWM), because of its contribution to phase matching condition [62,63].

One example of the measurement method is known as white light interferometry (WLI), which applies a broadband light source into a Mach-Zehnder interferometer (MZI) in the system or on a chip. In the case of the systems with an interferometer in a setup, most of them need the opt-mechanical system with dedicated alignment for optical paths,

with or without MZI [64-67]. On the other hand, in case of silicon photonics chip, they need to use MZI on a chip or ring resonator structure on a chip [68-70], and these structures potentially cause detailed attention in design and fabrication. In these measurements with MZI structure in the setup or a chip, typically a broadband source covering interested bandwidth such as a light emitting diode (LED) is applied and output spectrum is acquired with optical spectrum analyzer (OSA) [71-73]. However, due to the sweeping speed of OSA is not enough to remove the deviation caused by the time-varying fluctuation form the setup, such as fluctuation by temperature or air. Several methods are introduced to reduce this deviation with a feed-back loop, such as a phase-locked loop [74] or low-coherence technique [75]. However, these methods cast complexity on a system to achieve stable measurement. In this paper, we introduce the technique to measure chromatic dispersion applying a fast swept-source and MZI with optical fibers as a concise, robust, and optical alignment-free method. Swept source is commonly used in optical coherence tomography (OCT) known as swept-source optical coherence tomography (SS-OCT), due to its high-speed imaging [76, 77], and we implement its character of high-speed sweeping to measure interference from the MZI structure such as, WLI.

5.2 Theory and implementation

In our method, we applied swept source as an input source, and the output interferogram is similar in the WLI. Then, the interferogram in time-domain is described as,

$$I(t) = a^2 cos(\phi(t)) \quad (5.1)$$

where a is an amplitude of the interferogram. Because the fringes in the interferogram appear every 2π phase shift, we can plot unwrapped phase in time-domain. With λ-reference from the swept-source, the conversion from time-domain to frequency domain for the phase is executed. This is discussed in later part, Then, the propagation constant is described with the phase $\phi(f)$ as,

$$\phi(f) = \beta(f)*dL \tag{5.2}$$

where dL is a path length difference in the MZI. The propagation constant is expanded as a Taylor series for the central frequency f_0 as following,

$$\beta(f) = \beta_0(f_0) + (1/2!)\,\beta_1(f_0) + (1/3!)\,\beta_2(f_0) + \ldots \tag{5.3}$$

Upon the calculation of β, the chromatic dispersion is calculated with $\beta_2(f_0)$,

$$D(f) = -(2\pi c/\lambda^2)\,\beta_2(f_0). \tag{5.4}$$

5.3 Experimental procedures and post-processing

The setup, shown in Figure 5.1, has a swept-source as an input source, which the swept wavelength is between 1510-1610nm which covers C-band in telecommunication. Mach-Zehnder interferometer (MZI) with single-mode fibers consists of reference arm, which is connected to cascaded optical delay line (ODL) and compensates the interference length depending on the optical length of the sample arm, which connected to the fiber/device under test (FUT/DUT). The cascaded ODL covers total of 1530ps which covers the compensation of the FUT/DUT in our measurement. To maximize interference pattern in the measurement, polarization controller (PC) and variable optical attenuator (VOA) is connected at the end of each arm for optimization of the outputs from the arms. The two outputs from the arms are equalized in output power and

optimized polarization and coupled with 50/50 coupler and detected by a photodetector (PD). The outputs from PDs are measured by the oscilloscope. The other output from swept source is k-clock (A scan) with a rate of 19.7 kHz, which is used as the reference of the phase in the interference output measured in the oscilloscope.

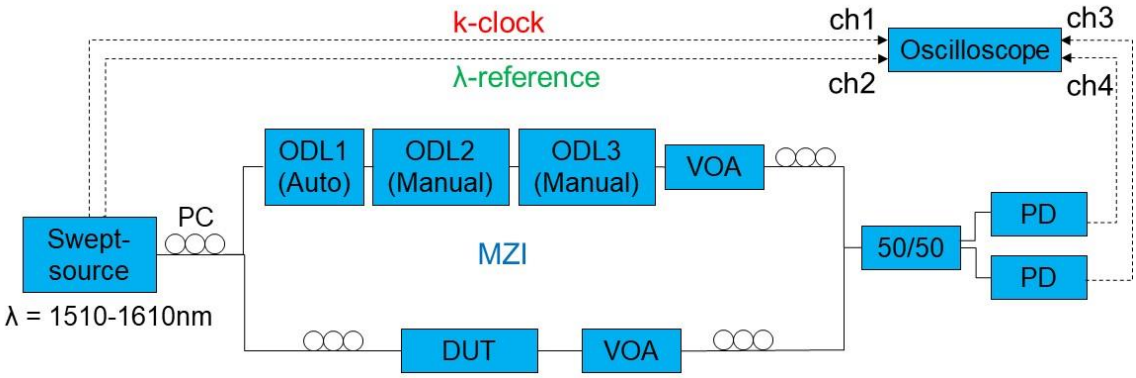

Figure 5.1. Setup of the measurement

Figure 5.2 shows the flowchart of the data processing in our dispersion measurement. In the measurement, we measure the interference from MZI with referencing k-clock from the swept-source as two separated detectors, with k-clock signal and λ-reference at 1530.1nm, directly from the swept-source, as shown in Figure 5.1. In the processing, analytic signal is acquired with Hilbert transform from the signals [78]. Then the unwrapped phase is calculated as an imaginary part of the analytic signal. For the unwrapped phase from the interference measurement part, the phase in nonlinear along the frequency domain, due to the relationship between the time-domain and frequency-domain of the interference pattern. Then, we execute conversion from time-domain to

frequency-domain with the λ-reference from the swept-source. Then, the phases are processed in frequency-domain to calculate chromatic dispersion.

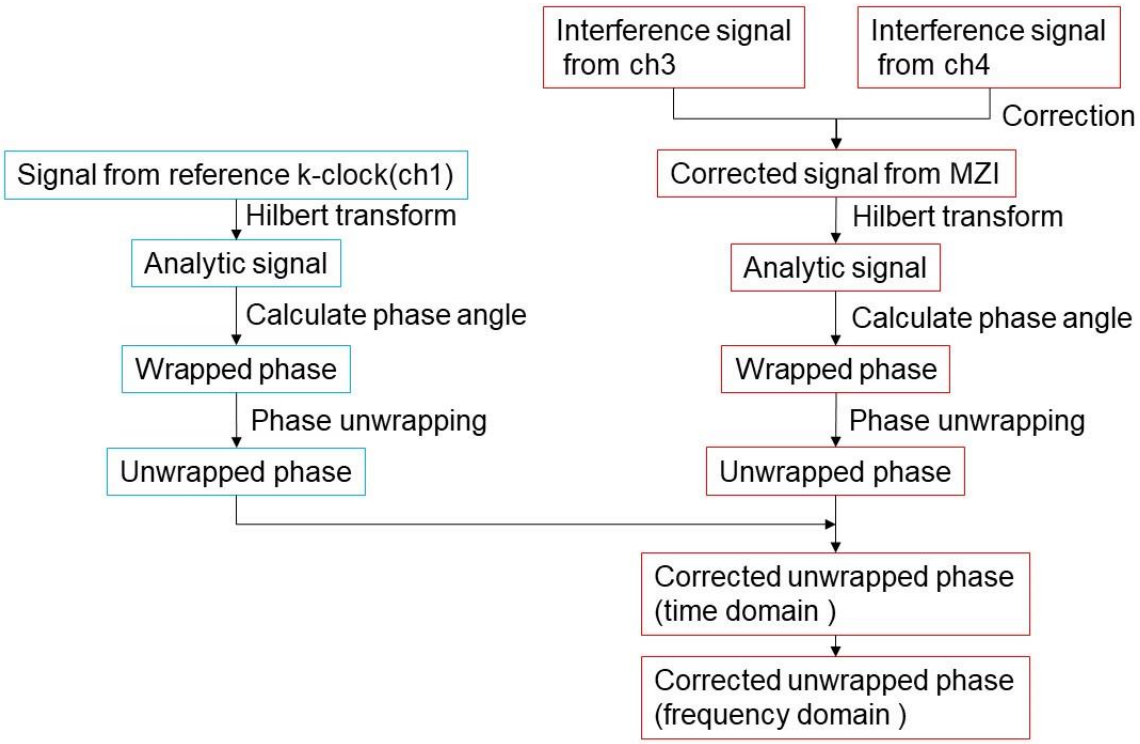

Figure 5.2. Flowchart of the measurement

5.4 Dispersion measurement for SMF-28

5.4.1 Interference measurement

We begin with interference measurement with the setup illustrated in Figure 5.1. First, interference from MZI and reference from k-clock is acquired as Figure 5.3 (a). Figure 5.3. (b) shows the expanded part at the same time-domain from Figure 5.3. (a). The single sweep from longer wavelength to short wavelength is plot as red. These

outputs are used in the post-processing, and they demonstrate clear interferograms shown in Figure 5.3. (b). Because the two interferograms from MZI, which third and fourth raw in the Figure 5.3, do not display apparent interferogram such as k-clock reference, these two interferograms are merged with dedicate alignment of each intensity. The fifth raw in Figure 5.3. shows the corrected interferogram from MZI. In the following processing, we apply this interferogram.

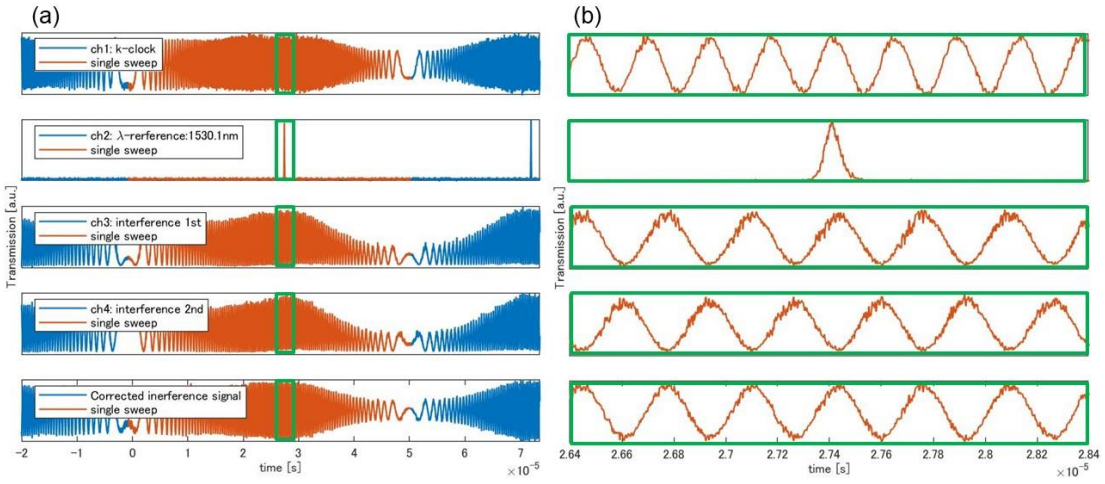

Figure 5.3. Output signals of interference measurement for SMF-28 with setup illustrated in Figure 5.1. (a) Output signals. From the top, reference of k-clock, λ-reference, two interferograms from MZI, and corrected signals derived from the two signals from MZI. (b) Expanded area from (a) with green-flamed areas from single sweep with plotted as red.

Then, the unwrapped phase is calculated from the interferogram as shown in Figure 5.4. At this time, the unwrapped phase has sinusoidal curvature due to its nonlinearity in the relationship between time-domain and frequency-domain, which is corrected in the conversion from time-domain to frequency domain, discussed in the next section.

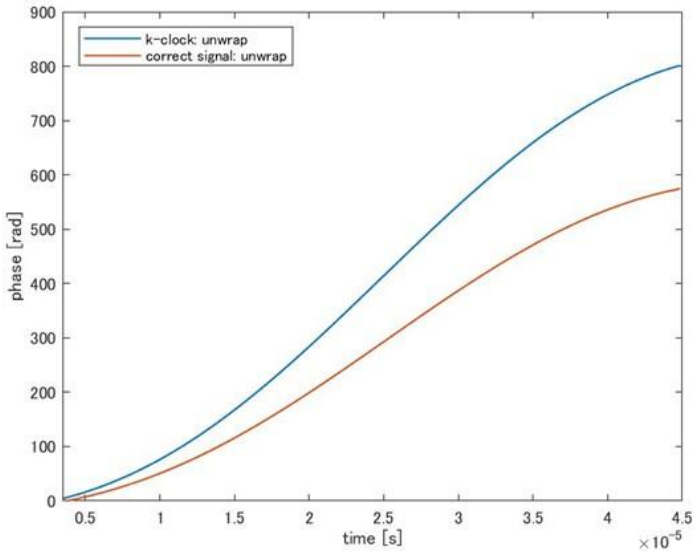

Figure 5.4. Unwrapped phase from the corrected interferogram for SMF-28.

5.4.2 Conversion from time-domain to frequency-domain

Upon the interference measurement discussed in the former section, to correct unwrapped phase with conversion from time-domain to frequency-domain, we used λ-reference from the swept-source. In our swept-source, its frequency shift Δf is 100GHz, and λ-reference is at 1530.1nm. Then its frequency is revealed as f_{ref} = 195.93Thz. In the interferogram, the peaks correspond to 2π shift in frequency-domain. Accordingly, the number of peaks n from the λ-reference is,

$$f = f_{ref} + n \cdot \Delta f. \tag{5.5}$$

Figure 5.5 shows the relationship between time-domain and frequency domain in this measurement, calculated from eq. (5.5). With this conversion, we applied the relationship between the time-domain and frequency-domain to the unwrapped phase for reference (i.e., without FUT/DUT) and sample (i.e., with FUT/DUT). From this conversion and

pitch of interference in Figure 5.8, resolution of this method is estimated as ~0.64nm. The unwrapped phases with conversion from time-domain into frequency-domain and plot along wavelength, is shown in the Figure 5.6.

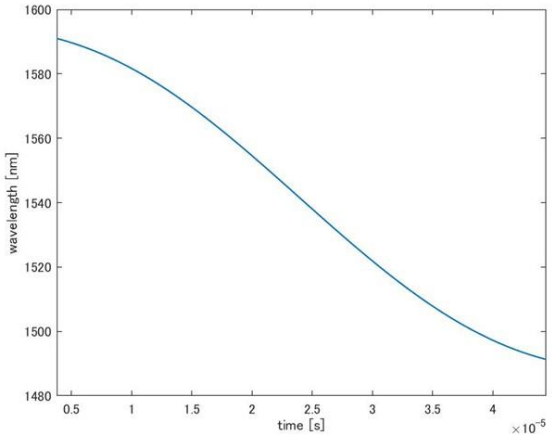

Figure 5.5. The relationship between time-domain and frequency domain which described as wavelength in the measurement.

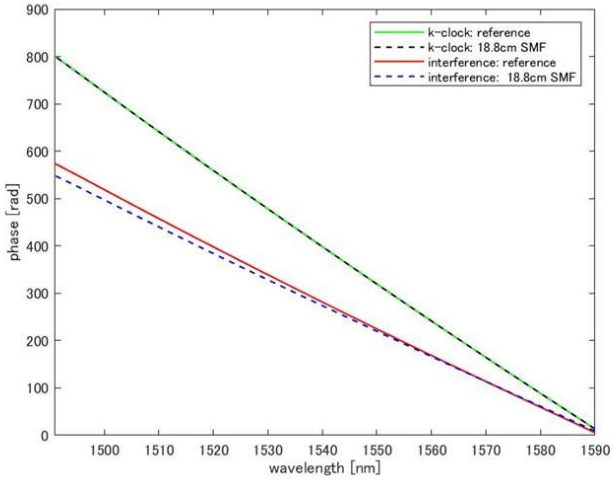

Figure 5.6. Unwrapped phase for SMF-28 with conversion from time-domain into frequency-domain and plot along wavelength.

5.4.3 Dispersion calculation

The dispersion calculation is calculated based on the aligned phase shown in the Figure 5.5. We applied the calculation discussed in the section 2 into the software of our own made with MATLAB®. Figure 5.7 shows the calculated chromatic dispersion and dispersion slope with comparison to datasheet, and it demonstrates the good agreement with the datasheet in the sample. In this measurement process, once the interference pattern is scanned in less than one sec, we can apply the calculation with semi-automated software developed by our own, and instantly acquires the dispersion data.

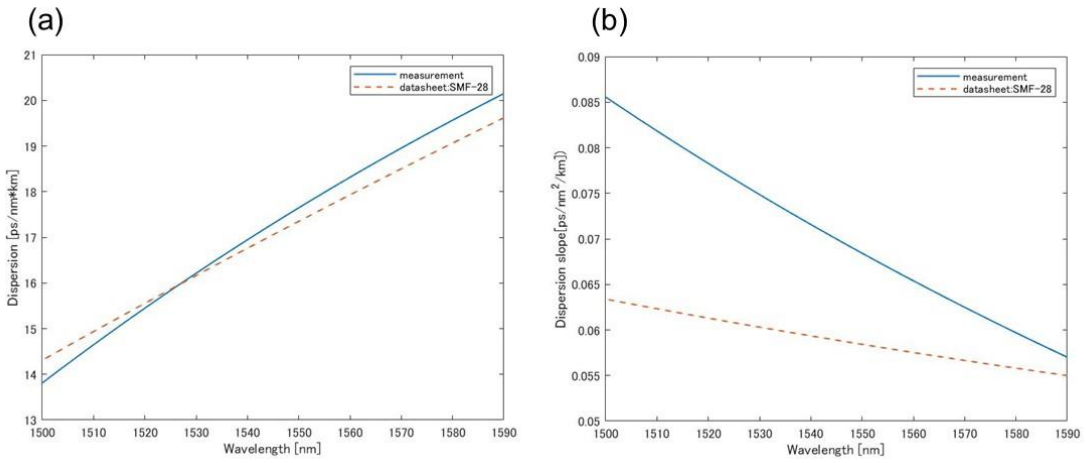

Figure 5.7. Chromatic dispersion and dispersion slope for SMF-28 with comparison to datasheet. (a) Chromatic dispersion (b) dispersion slope

5.5 Dispersion measurement for silicon waveguide

According to the measurement for single mode fiber, we implemented to the fabricated silicon waveguide as an example of application of our method to phonics devices. In the measurement, the method is basically the same for the case of SMF. However, the measurement for reference is executed for the short length of Si waveguide,

then the other measurement as a sample is executed for the additional length of Si waveguide. We used different length with 3.28cm, 5.36, and 7.44cm. The cross section is width of 460nm and thickness of 273nm with slab thickness of 55nm. Figure 5.8 shows the measurement for the Si waveguides from different slot with simulation is plot with dot line. Then the simulation shows good fitting against the measurement. Due to the tolerance in the fabrication, we could see variation of difference between ~100 and 900 [ps/(nm·km)]. For the samples with the dispersion between ~800-900 has much thicker thickness of slab/waveguide as different slots from Lot A, and these samples are useful to discuss the effect of chromatic dispersion in FWM in the ring mixer, discussed in the next section.

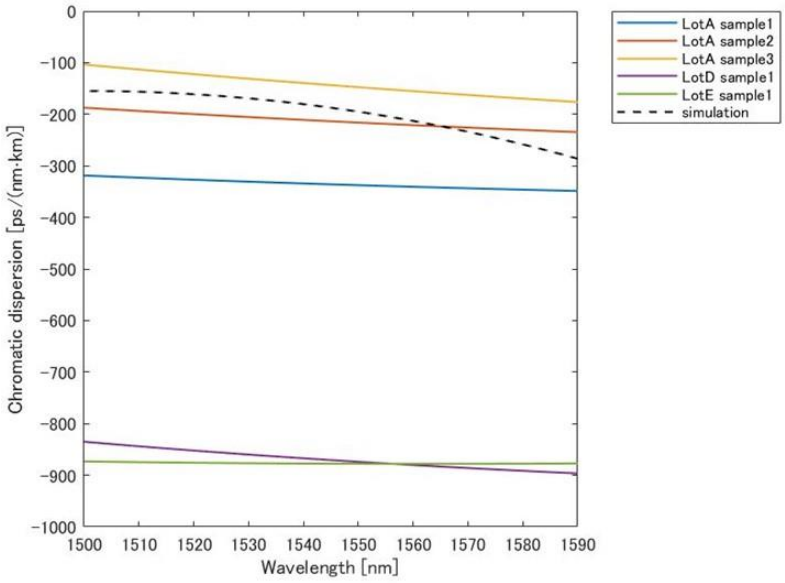

Figure 5.8. Dispersion for Si waveguides.

5.6 Dispersion dependence for comb generation

With the measurement of chromatic dispersion for Si waveguides, we are concerned with its contribution to the FWM in the ring mixer. Then, we demonstrated frequency comb generation measurement, with the same procedure demonstrated the former section. Ring mixers are fabricated on the same chips that we evaluated Si waveguides in the section 5.5. Except for the chromatic dispersion, we consider the power splitting ratio k of the coupler in the ring mixers will affect the output spectrum. Then, the power splitting ratio is also measured in the coupler part, also fabricated on each chip [79]. In this measurement, the input power is fixed as 21 dBm, and the phase is tuned with the phase shifter fabricated on each device. Figure 5.9 shows the output spectrum for 5 different samples that those dispersions are measured in the section 5. As we discussed before, this variation of dispersion is originated in the fabrication, mainly from the thickness of waveguides/slabs. Figure 5.9 (a) shows 7 tones are input source, and Figure 5.9 (c) shows 15 tones are input source. We denote dispersion and power splitting ratio for each sample at 1550nm. For Figure 5.9 (a) and (c), comparing each sample, both dispersion and power splitting ratio contribute to the smooth and broad spectrum as an output, i.e., high power splitting ratio (k = 0.84) and lower negative dispersion (D = -147 [ps/(nm·km)]) are suitable for smooth and broad spectrum. These parameters contribute to the better phase matching in FWM in the ring mixer, and as result, it generates smooth and broad spectrum. As a note, in Figure 5.9 (b), the spectrum from D = -216 [ps/(nm·km)] and -337 [ps/(nm·km)] show the process of generation in the primary sidebands discussed in other articles [80]. Then the cascaded FWM has enough phase-matching, the spectrum can be smoother and broader than those spectra, such as D

= -147 [ps/(nm·km)]. In addition, comparison between the spectrum from D = -337 [ps/(nm·km)] and -878 [ps/(nm·km)] show the effect of chromatic dispersion over the power splitting ratio, because even though spectrum D = -337 [ps/(nm·km)] has lower coupling (k = 0.68) than D = -878 [ps/(nm·km)] with k = 0.72, it shows broader spectrum. This indicates that coupling ratio is not enough to dominate the effect of chromatic dispersion to achieve phase-matching in the ring mixer. These trends are also shown in the simulation (Figure 5.9 (b), (d)) for both 15 tone and 7 tone inputs. The simulation is performed in the same engine described in the former sections. Figure 5.10 shows the -20 dB bandwidth (BW) for 15 tones in Figure 5.9. It shows the trend that the BW is larger in weak negative dispersion.

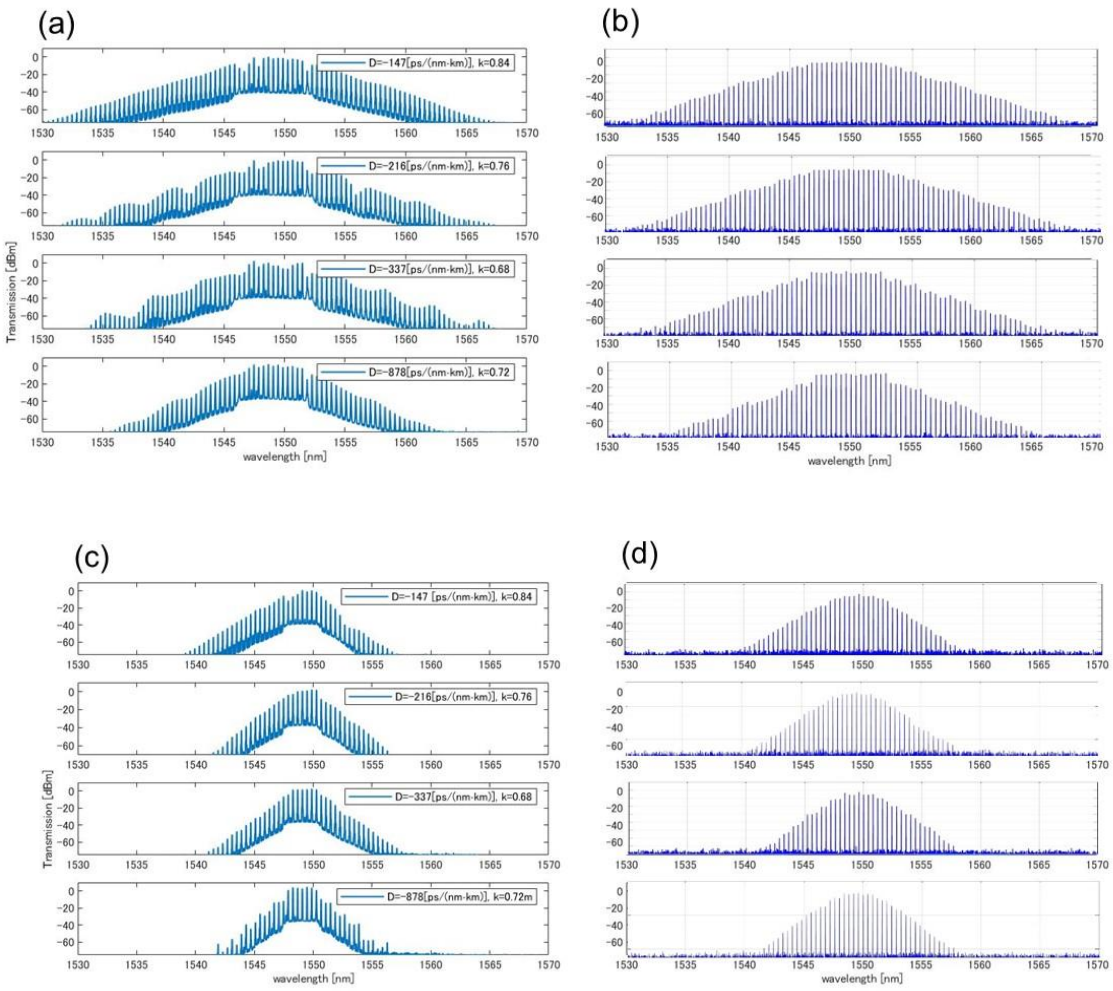

Figure 5.9 Output spectrum of comb generation for different devices according to chromatic dispersion D and power splitting ratio k at 1550nm. (a) Output from 15 tones input comb. (b) simulation for 15 tones. (c) Output from 7 tones input comb. (d) simulation for 7tones.

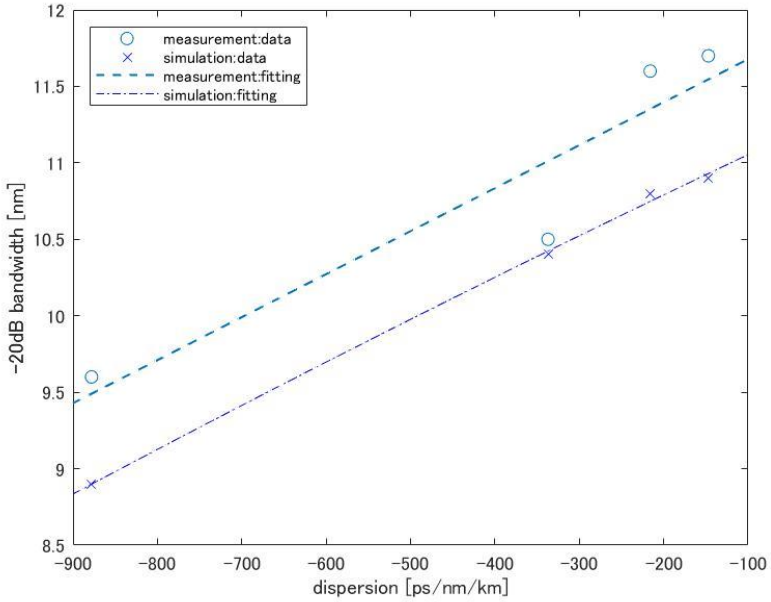

Figure 5.10 -20 bandwidth for 15 tones in Figure 5.9

5.7 Chapter summary

In this chapter, experimental evaluation for chromatic dispersion is demonstrated through the fiber-based setup, because its importance in the phase matching condition in FWM to generate broad spectrum in the nonlinear optics device including ring mixer. The validation of the method is evaluated through SMF-28 as a DUT, and its chromatic dispersion and dispersion slope is well matched to the datasheet.

Upon the verification of the measurement method, variety of chromatic dispersion for fabricated silicon waveguides, fabricated on the same chip with the ring mixer, is demonstrated with the relationship to spectrum with simulation/experiment. The data show that weaker negative dispersion (i.e. close to zero-dispersion, such as D = -147 [ps/nm/km]), performers broader spectrum due to better phase-matching condition than the strong negative dispersion.

Chapter 5, in part, is currently being prepared for submission for publication of the material. Motohiko Eto, Bill Ping-Piu Kuo, and Stojan Radic. The dissertation author was the primary investigator and author of this material.

Chapter 6

Low-Noise frequency comb generation in silicon ring mixer

Upon the former chapters, comb generation from silicon mixer is discussed. In this chapter, low-noise frequency comb is demonstrated for the application of telecommunication. In addition, the broadened spectrum due to the low-noise input is also demonstrated and measurement of device characteristics such as coupling ratio and chromatic dispersion discussed in Chapter 5.

6.1 Introduction

Low-phase noise frequency comb is important in variety of applications, such as metrology and communications [81,82], and phase noise in compact mixer is compared in other literature [83-85], and those mechanisms are investigated that those noise originated in variable factors [86], such as noise from pump lasers, thermal noise [87], and oscillators [88]. In this thesis, silicon mixer is pumped with cascaded phase modulator with RF generator, discussed in Chapter 4, that different from most of other compact ring mixer pumped by single mode lasers, then this causes complexity of causing source pf phase noise in the system.

To investigate phase noise through the silicon ring mixer, self-homodyne method is deployed with fiber-based frequency comb as an initial source. In this thesis, FWM in silicon ring mixer is processed through multiple tone inputs constructed as fiber-optic

systems, then the phase noise measurement is attentively investigated considering the effect from frequency comb source.

6.2 FWM from Fiber based comb source

6.2.1. Introduction

In this section, instead of cascaded phase modulator, fiber-based comb source is implemented to verify its effect on the broadband FWM in silicon ring mixer. In the last sections, considering the application of FWM thorough the silicon ring mixer in silicon photonics components, cascaded phase modulator is implemented to the measurement setup. However, those cascaded PMs are potentially containing electric phase noise due to RF generators, and they are not suitable for low phase noise measurement implement in this section. Then, in this section, part of input com source into the chip is changed to fiber-based systems. In addition to decrease phase noise from the input source, broadening output spectrum is also expected due to not only lower noise but also higher SNR than former setup.

6.2.2 Setup

The setup is shown in Figure 6.1, that based on self-heterodyne detection [84,85]. Comparing to the former chapters, the initial input source is changed from tunable single mode laser to low-noise frequency comb (Teratone TT-50 (RAM photonics)). In this setup, the wavelength is fixed ~1559nm, due to the specification of the comb source. The

optical seed from the comb source is send into the phase modulator (PM) with RF frequency around ~25GHz to generate input tones, and the output from the phase modulator is filtered with programmable optical processor (POS, waveshaper (Finisar)) to tune the phase to maximize FWM efficiency in the 100-meter HNLF by pumped thorough EDFA to generate input tones. It is denoted that in Chapter 4, the other phase modulator is used in this part, and this change from phase modulator to HNLF has contribution to low-noise input tones. After HNLF, the output is filtered with programmable optical processor and BF to tune and filter to generate flat-top 15tones and pumped with polarization maintain amplifier (PM amp, EAR-5K-C (IPG Photonics)) that processed in Chapter 4. The tuned 15 input tones are coupled to the chip and tuned its phase with the phase shifter on the chip that is discussed in Chapter 4.

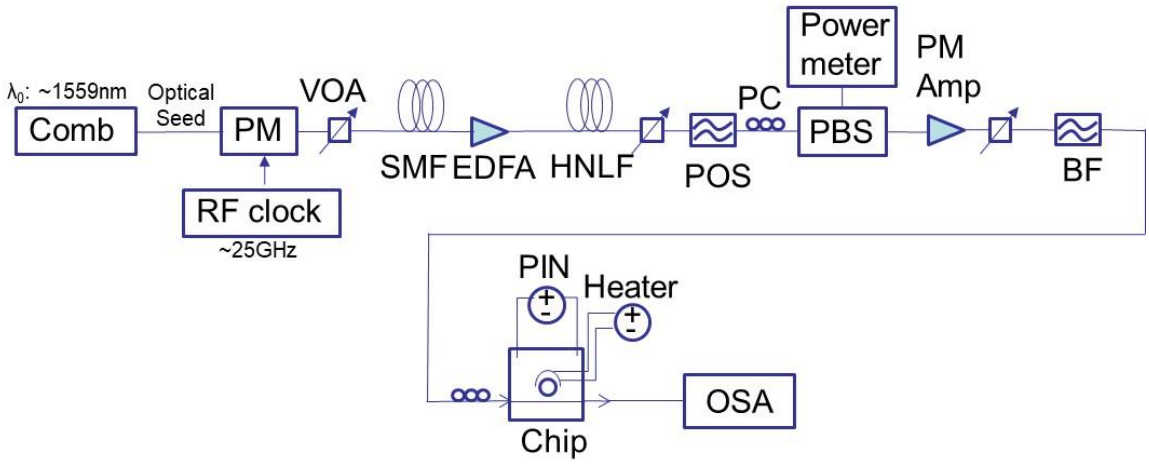

Figure 6.1 Setup of the measurement

6.2.3 Experimental results

As discussed in Chapter 4. In the setup, the peaks and phases are tuned as 15 tones. Figure 6.2 demonstrates the comparison between the tuning. Figure 6.2 shows the spectrum from HNLF in the middle of the setup and tuned 15tones after POS and BF. Due to the pulse compression, instead of phase tuning with POS in the setup from former chapter, and output from HNLF has broad spectrum in the C band centered on 1559nm, after amplification with a PM amplifier, filtering from BFs, and tunning of peaks and phases with POS, 15tones of flat-top peak that is the same procedure discussed in the Chapter 4.

Figure 6.3 and Figure 6.4 show the measured output spectrum from the chip in the setup described in Section 6.2. For this measurement, we have chosen the sample with the lower negative dispersion(~-200ps/nm/km) and overcoupling (power splitting ratio~0.75), and careful alignment of RF tuning. It can be seen in the input tones that those SNR drops more than 10 dB that indicates high conversion efficiency in FWM that contributes broad spectrum. As a best result the spectrum can be broaden between ~1525-1600nm at -75dBm noise floor (red circled in Figure 6.4 (a)).

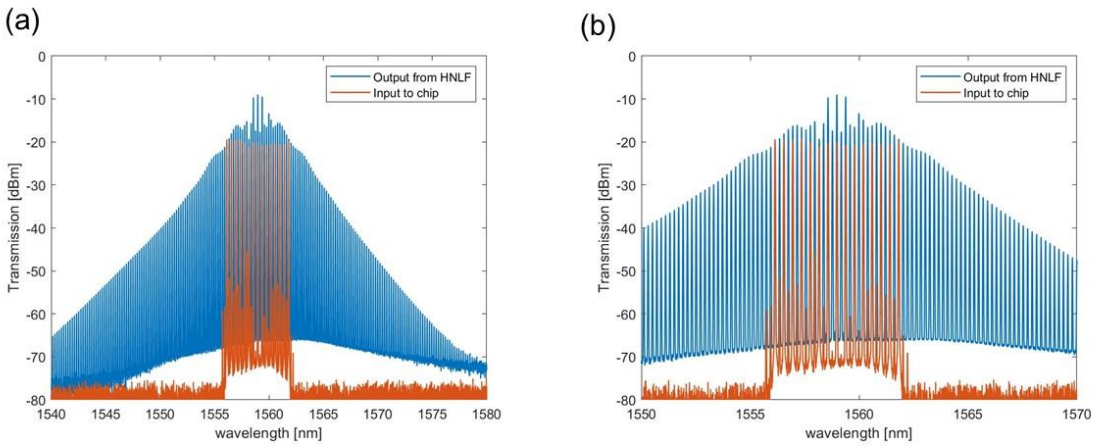

Figure 6.2 Output spectrum from parts of the setup for output from HNLF input to the chip (a) spectrum between 1540-1580nm. (b) spectrum between 1550-1570 for expansion.

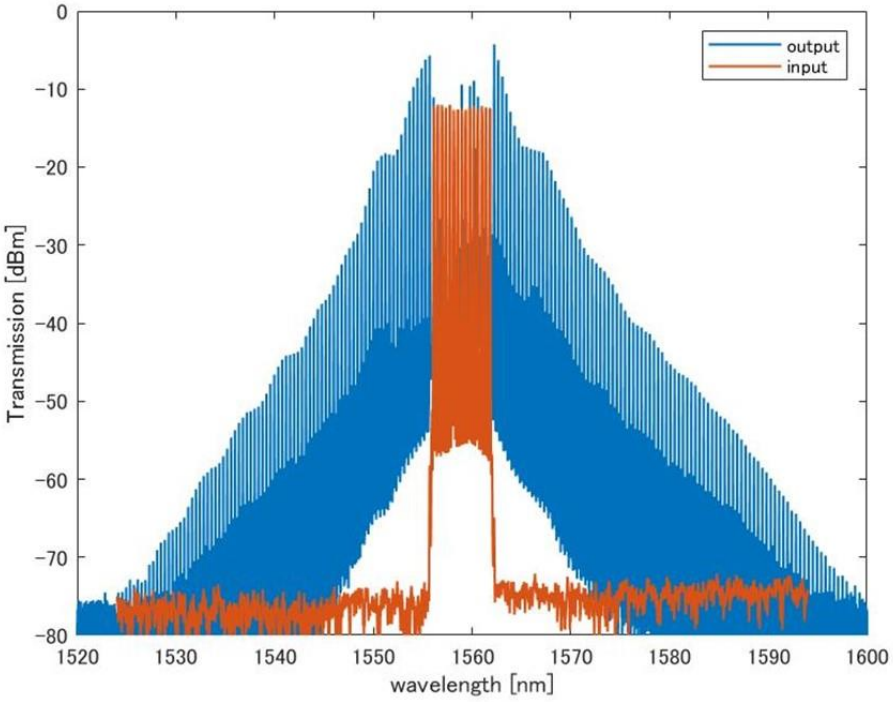

Figure 6.3 Input/Output spectrum from chip.

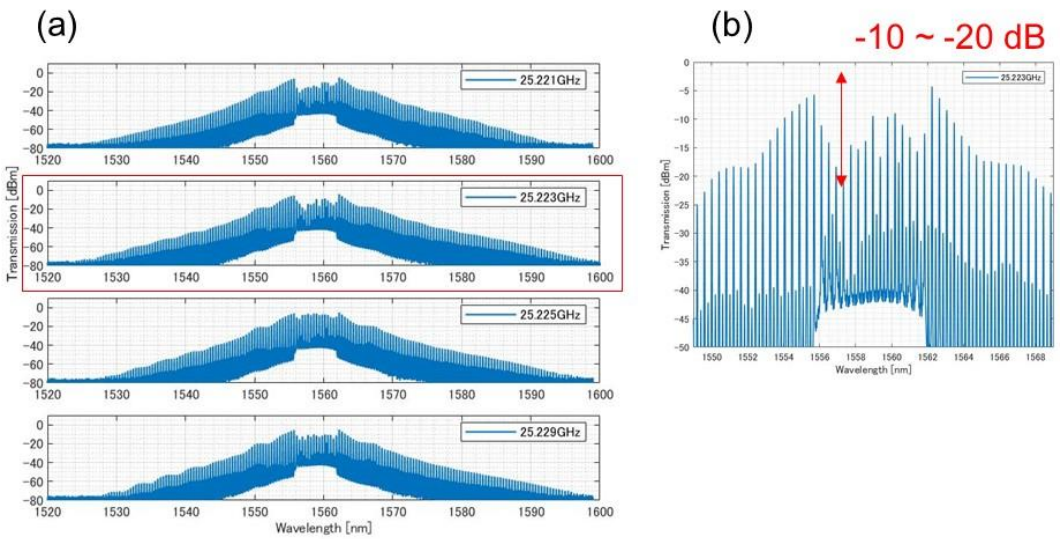

Figure 6.4 Output spectrum from the chip (a) comparison of spectrum between different RF. (b) expansion of input tones in the best effort in the (a) (red circled)

6.3 Phase noise

6.3.1 Introduction

Phase noise is evaluated single sideband (SSB) phase noise measured on oscilloscope and post-processed with discussion of phase noise level, and this is comparable to other material schemes [83, 89-91]. To investigate phase noise for different tones, PSD for mixing signals from nth tones from outside of input tones are demonstrated.

6.3.2 Setup

Figure 6.5 illustrates the setup for phase noise measurement. In this setup, comb source uses external clock to minimize RF noise, originated in using different clocks deployed former setup, and comb out is split into 50/50 coupler to the chip through

pumping and filtering similar to the former setups, and the other output is modulated with acousto-optic modulator (AOM) with pumping. ~87m SMF is added to match optical path to match at the input of the other 50/50 coupler for the homodyne measurement. The output from the chip is coupled with the comb out from the input comb source with 50/50 coupler and the two output of the beat note is send into the grating filter (TB-9P (JDS Uniphase)) to filter out to the single tone by each grating filter with separated tones. The two filtered output tones are detected by high-speed photodetectors, and the signals are measured by oscilloscope. Measured signals for nth tones are mixed and processed as PSD analysis as mutual phase noises.

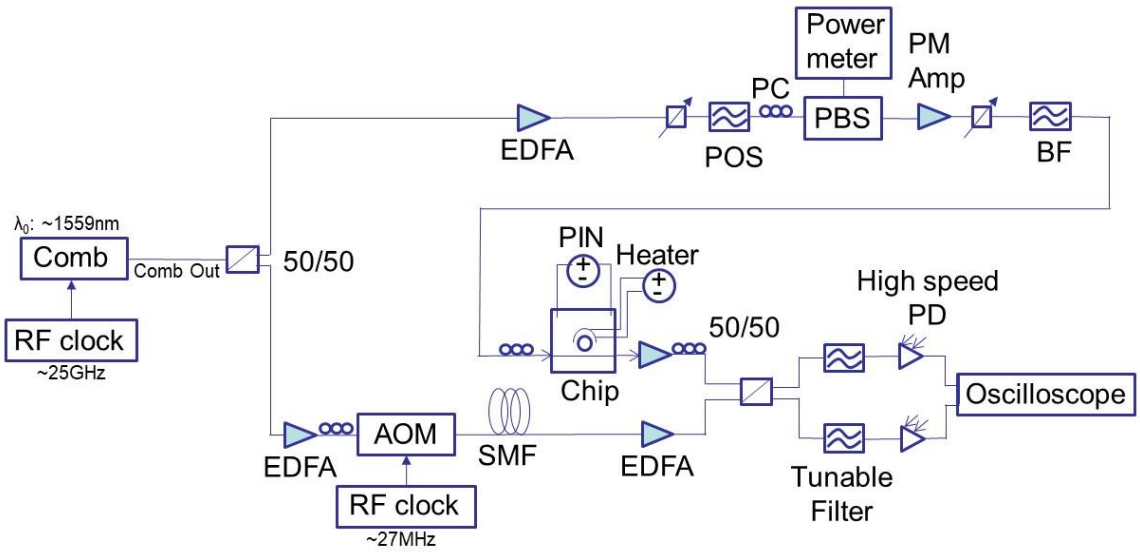

Figure 6.5 Setup for phase noise measurement

6.3.3 Experiment results

Figure 6.6 illustrates PSD for mixing signal for different tones between 1st and 10th. In these figures, as the number of tone increase (i.e., far from the input tones), the

peaks decrease due to phase mismatch in FWM mainly because chromatic dispersion (~-250ps/nm/km).

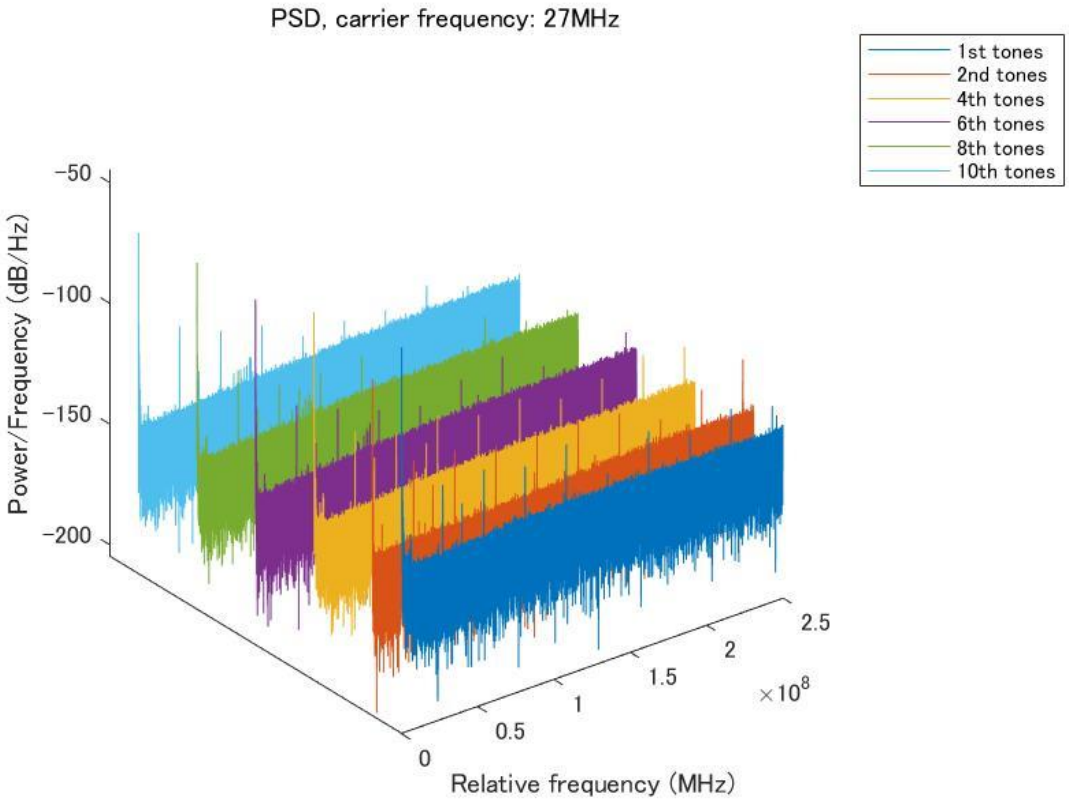

Figure 6.6 PSD for mixing signal for different tones between 1st to 10th bandwidth until 250MHz.

Figure 6.7 shows the SNR of carrier frequency between 1st and 10th. It clearly shows the SNR od carrier frequency decrease as the number of tone increase. Then, it is expected that SNR can be improved with the chromatic dispersion is close to zero, and these SNR can be increase due to higher FWM efficiency, with dispersion engineering.

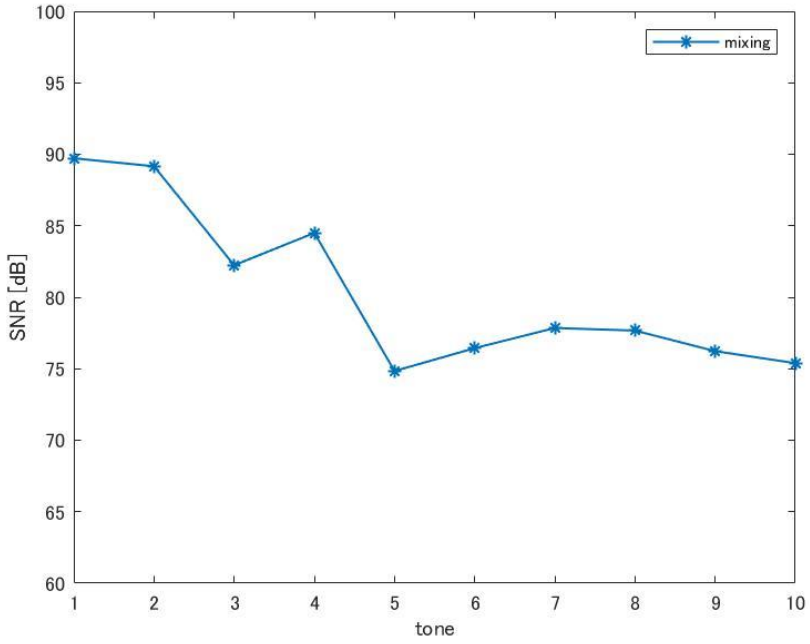

Figure 6.7 SNR of carrier frequency between 1st and 10th.

6.4 Chapter summary

In this chapter, the experimental demonstration of improvement of setup for FWM with a ring mixer and evaluation of phase noise is performed. For the improvement of the setup, input tones are generated by comb source, instead of cascaded phase modulators, that contribute higher SNR of input tone with lower noises, and as a result, broadened output spectrum between 1520 and 1600 nm at -75 dBm noise floor.

Chapter 6, in part, is currently being prepared for submission for publication of the material. Motohiko Eto, Bill Ping-Piu Kuo, and Stojan Radic. The dissertation author was the primary investigator and author of this material.

Chapter 7

Conclusion

7.1 Dissertation summary

Recently the demand for high-speed telecommunication is rising the demand for low-noise frequency comb source with compact and low energy consumption systems which is mainly based on fiber optic systems. This dissertation reaches for this application with silicon photonics technology for frequency comb generation through cascaded FWM in the silicon ring mixer for coherent optical sources.

In the optical parametric process in nonlinear optics, cascaded FWM is the key concept for the comb generation in this dissertation which detailed in Chapter 2. For the device side, Dispersion engineering derived from material and waveguide dispersion, and TPA which hinders efficiency of optical parametric process is discussed with ring resonator characteristics such as NLS for guided wave propagation, Q factor and finesse reveals the property of resonance mode. In the chapter 3, device characterization to meet the concept discussed in chapter 2 is investigated with device performances from experimental results such as waveguide loss and FSR. Photonic/electric simulation results are demonstrated in the manufacturing capability in the MPW service. In the photonic simulation, dispersion engineering is promoted to target -200 [ps/nm/km] to avoid mixing loss originated in phase mismatch. For electric simulation, PIN structure is investigated to compatible between low optical loss and capability of sweeping electron/hole. Upon the device simulations, simulation of comb generation in silicon ring mixer is demonstrated

to investigate output spectrum. In the Chapter 4, demonstration of comb generation in silicon ring mixer is described with its concept and procedure in the experiment. The multiple tone pump, which meticulous tuning of phase and peaks of input tones, enables efficient FWM and broad comb generation in the c-band between 1520-1580 nm at -65dBm noise floor in phase-locked state.

For further investigation of comb generation in the silicon ring mixer discussed in this thesis, chromatic dispersion is attentively discussed in chapter 5. To investigate chromatic dispersion of silicon waveguide, phase difference is measured in the setup based on optical fiber system with swept-source. This measurement is optical alignment-free except for the coupling to the silicon chip, and the robustness of measurement is verified with the measurement of SMF as DUT. The experimental data reveals the chromatic dispersion is between -100~-900 [nm/nm/km] in the samples that mainly caused from device thickness and its contribution to efficiency is discussed with experimental and theoretical results that low-negative dispersion with overcoupled sample demonstrates higher efficiency and broad spectrum. For the approach from system side, the setup for input tones is revised in chapter 6 to achieve broad and low-noise spectrum. It also demonstrates the spectrum between 1525-1600 nm at -75dBm noise floor covering C -L band in the telecommunication. Phase noise is also investigated by hetero detection technique that shows -107dBc/Hz for 8.7MHz carrier frequency from two output tones from the generated comb.

7.2 Future directions

In this dissertation, the frequency comb generation is demonstrated in C- L band with detailed design and construction, and experiment. However, there are multiple themes to be investigated to further possibility for the application. Following sections are for those possible themes to be investigated.

7.2.1 Broad spectrum source: cascaded ring mixer

In this dissertation, the mixing stage is performed as a single stage. However, to overcome broad spectrum within achievable a single mixer, multiple stage scheme is demonstrated in fiber system [91]. Figure 7.1 shows the example of setup of the multiple stage mixing using silicon ring mixer. For the setup until 1st stage on the chip is the similar construction in this thesis to generate spectrum. For the further broad spectrum capable on the single stage, pulse compression stage and 2nd stage are added after the 1st stage. As discussed in the chapter 4, for efficient FWM, the high compression of phase is important, in this construction, SMF has the role as a pulse compression stage. After the pulse compression, input source into the 2nd stage is pumped, due to the insertion loss cannot be negligible for broad FWM in the 2nd stage. In the 2nd stage, its phase is tuned to lock the phase in the resonance, operated in this dissertation.

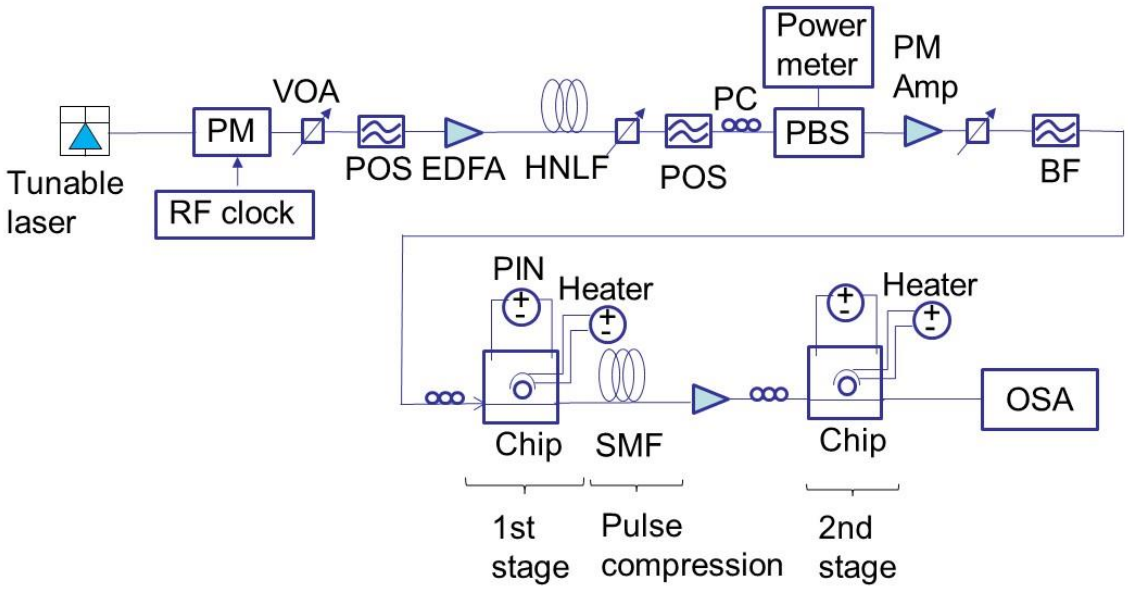

Figure 7.1 Example of a setup for cascaded ring mixer

7.2.2 Miniaturizing comb system on a silicon chip

Miniaturizing fiber system on a silicon chips is one has already demonstrated [93-96]. and application of a comb generation via silicon photonics [97-99]. However, for comb generation, it is not performed on silicon device in telecommunication band. This dissertation focusses on those application, due to its material is silicon fabricated in CMOS compatible process.

[Bibliography]

1. Cisco, “Cisco Annual Internet Report (2018-2023)”, Cisco (2020).

2. L. Lundberg, M. Mazur, A. Mirani, B. Foo, J. Schroder, V. T.-Company, M. Karlsson, and P. A. Anderkson, “Phase-coherent lightwave communications with frequency combs”. *Nat Commun* **11,** 201 (2020).

3. J. Pfeifle, , V. Brasch, , M. Lauermann, Y. Yu, D. Wegner, T. Herr, K. Hartinger, P. Schindler, J. Li, D. Hillerkuss, R. Schmorgow, C. Weinmann, R. Holzwarth, W. Freude, J. Leuthold, T. J. Kippenberg, “Coherent terabit communications with microresonator Kerr frequency combs”. *Nature Photon* **8,** 375–380 (2014).

4. Picqué, N., Hänsch, T.W. “Frequency comb spectroscopy”. *Nature Photon* **13,** 146–157 (2019).

5. S. B. Papp, K. Beha, P. Del’Haye, F. Quinlan, H. Lee, K. J. Vahala, and S. A. Diddams, "Microresonator frequency comb optical clock," *Optica* **1**, 10-14 (2014).

6. J. Riemensberger, A. Lukashchuk, M. Karpov, W. Weng, E. Lucas, J. Liu, and T. J. Kippenberg, “Massively parallel coherent laser ranging using a soliton microcomb”. *Nature* **581,** 164–170 (2020).

7. R. A. Soref, "Silicon-based optoelectronics", *Proceedings of the IEEE*, vol. **81**, no. 12, pp. 1687-1706 (1993)

8. B. Jalali, S. Yegnanarayanan, T. Yoon, T. Yoshimoto, I. Rendina and F. Coppinger, "Advances in silicon-on-insulator optoelectronics," in *IEEE Journal of Selected Topics in Quantum Electronics*, vol. **4**, no. 6, pp. 938-947, (1998).

9. B. Jalali, and S. Fathpour, “Silicon photonics”, *IEEE. J. Light. Technol.* **24**(12), 4600-4615 (2006).

10. R. Soref, "The Past, Present, and Future of Silicon Photonics," in *IEEE Journal of Selected Topics in Quantum Electronics*, vol. 12, no. 6, pp. 1678-1687, (2006).

11. S. Fathpour, “Emerging heterogeneous integrated photonic platforms on silicon”, *Nanophotonics*, **4**(2), 143-165 (2015).

12. X. Chen M. M. Milosevic, S. Stankovic, S. Reynolds, T. D. Bucio, K. Ki, D. J. Thomson, F. Gardes, and G. T. Reed, "The Emergence of Silicon Photonics as a Flexible Technology Platform," in *Proceedings of the IEEE*, vol. 106, no. 12, pp. 2101-2116 (2018).

13. A. Novack, M. Streshinsky, R. Ding, Y. Liu, A. E.-J. Kim, G.-Q. Lo, T. B.-Jones, and M. Hochberg, "Progress in silicon platforms for integrated optics", *Nanophotonics*, **3**(4-5), 205-214 (2014).

14. Z. Fang, and C. Z. Zhao, "Recent progress in silicon photonics: A Review", *International Scholarly Research Notices*, vol. **2012**, Article ID 428690 (2012).

15. T. J. Kippenberg, R. Holzwarth, and S. A. Didadams, "Microresonator-based optical frequency combs", *Science*, **332**, 555-559 (2010).

16. P. Trocha, M. Karpov, D. Ganin, M. H. P. Pfeiffer, A. Kordts, S. Wolf, J. Krockenberger, P. Martin-Palomo, C. Weimann, S. Randel, W. Freude, T. J. Kippenberg, and C. Koos, "Ultrafast optical ranging using microresonator soliton frequency combs", *Science*, **359**, 887-891 (2018).

17. G. Lin, A. Coillet, and Y. K. Chembo, "Nonlinear photonics with high-Q whispering-galley-mode resonators", *Adv. Opt. Photon*. **9**, 828-889 (2017).

18. J. Pfeifle, V. Brasch, M. Lauermann, Y. Yu, D. Wegner, T. Herr, K. Hartinger, P. Schindler, J. Li, D. Hillerkuss, R. Schmogrow, C. Weimann, R. Holzwarth, W. Freude, J. Leuthold, T. J. Kippenberg, and C. Koos, "Coherent terabit communications with microresonator Kerr frequency combs", *Nat. Photon*. **8**, 375-380 (2014).

19. D. T. Spencer, T. Drake, T. C. Briles, J. Stone, L. C. Sinclair, C. Frederik, Q. Li, D. Westly, B. R. Ilic, A. Bluestone, N. Volet, T. Komljenvic, L. Chang, S. H. Lee, D. Y. Oh, M.-G., Suh, K. Y. Yang, M. H. P. Pfeiffer, T. J. Kippenberg, E. Norberg, L. Theogarajan, K. Vahala, N. R. Newbury, K. Srinvasan, J. E. Bowers, S. A. Diddams, and S. B. Papp, "An optical-frequency synthesizer using integrated photonics", *Nature*, **557** 81-85 (2018).

20. B. P. -P. Kuo, E. Myslivets, V. Ataie, E. G. Temprana, N. Alic, and S. Radic, "Wideband parametric frequency comb as coherent optical carrier", *J. Light. Technol*, **31**, 3414-3419 (2013).

21. J. Leuthold, C.Koos, and W. Freude, "Nonlinear silicon photonics", *Nat. Photon*. **4**. 535-544 (2010).

22. A. G. Griffith, R. K. W. Lau. J. Cardenas, Y. Okawachi, A. Mohanty, R. Fain, Y. H. D. Lee, M. Yu, C. T. Phare, C. B. Poitras, A. L. Gaeta, and M. Lipson, "Silicon-chip mid-infrared frequency comb generation", *Nat. Commun*. **6**, 6229 (2015).

23. M. Yu, Y. Okawachi, A. G. Griffith, M. Lipson, and A. L. Gaeta, "Mode-locked mid-infrared frequency combs in a silicon microresonator", *Optica*. **3**, 854-860 (2016).

24. I. Demirtzioglou, C. Lacava, K. R. H. Bottrill, D. J. Thomson, G. T. Reed, D. J. Richardson, and P. Petropoulos, "Frequency comb generation in a silicon ring resonator modulator", *Opt. Lett.* **26**, 790-797 (2018).

25. R. Boyd, "Nonlinear optics", Academic Press, (2008).

26. D. Dimitropoulos, R. Claps, Y. Han, and B. Jalali, "Nonlinear optics in silicon waveguides: Stimulated Raman scattering and two-photon absorption,", *Proc. SPIE*, vol. **4987**, 140–148 (2003).

27. V. V.Raghunathan, R. Claps, D. Dimitropoulos, and B. Jalali, "Parametric Raman wavelength conversion in scaled silicon waveguides", *J. Light. Techn*ol, **23**(6) 2094(2005).

28. C.J. Krückel, A. Fülöp, T. Klintberg, J. Bengtsson, P.A. Andrekson, and V. T.-Company, **"**Linear and nonlinear characterization of low-stress high-confinement silicon-rich nitride waveguides", *Opt. Exp*. **23**(20), 25827-25837(2015).

29. S. Coen, H. G. Randle, T. Sylvestre, and M. Erkintalo, "Modeling of octave-spanning Kerr frequency combs using a generalized mean-filed Lugiato-Lefever model", *Appl. Phys. Lett*, **86** 071115(2005).

30. G.P. Agrawal, "Nonlinear fiber optics", Ch2. Elsevier (2013).

31. W. Bogaerts, P. DeHeyn, T. V. Vaerenbergh, K. DeVos, S. KumarSelvaraja, T. Claes, P. Dumon, P. Bienstman, D. VanThourhout, and R. Baets, "Silicon microring resonators", *Las. Photon*. **6**, 47-73(2012).

32. J. Heebner, R. Grover, and T. A. Ibrahim, "Optical microresonators: Theory fabrication and applications", Springer (2008).

33. N. Shibata, R. Braun, and R. Waarts, "Phase-mismatch dependence of efficiency of wave generation through four wave- mixing in a single-mode optical fiber", J. Quantum. Electron, 23(7) 1205 (1987).

34. D.Dimitropoulos, R. Jahveri, R. Claps, J. C. S. Woo, and B. Jalali, "Lifetime of photogenerated carriers in silicon-on-insulator rib waveguides", *Appl. Phys. Lett*, **86**, 071115 (2005).

35. R. Soref, and B. Bennett, "Electrooptical Effects in Silicon", IEEE, J. Quant. Elec. **23**(1) 123 - 129(1987).

36. L. Chrostowski, and M. Hochberg, “silicon photonics design from devices to systems”, Cambridge University press (2015).

37. IPKISS (Luceda photonics) https://www.lucedaphotonics.com/en/product/ipkiss

38. X. Xue, Y. Xuan, Y. Liu, P.-H. Wang, S. Chen, J. Wang, D. E. Leaird, M. Qi, and A. M. Weiner, “Mode-locked dark pulse Kerr combs in normal-dispersion microresonators”, *Nat. Photon*. **9**, 594-600 (2015).

39. S.-W. Huang, H. Liu, J. Yang, M. Yu, D.-L. Kwong, and C. W. Wong, “Smooth and flat phase-locked Kerr frequency comb generation by higher order mode suppression”, *Sci. Rep*. **6**, 26255 (2016).

40. W. Boggaerts, P. D. Heyn, T. V. Varrenbergh, K. D. Vos, S. K. Selvaraja, T. Claes, P. Dumon, P. Bienstman, D. Van Thourhout, and R. Baets, “Silicon microring resonators”, *Laser, & Photon*. Rev. **6**(1), 47-73 (2012).

41. Y. Liu, Y. Xuan, X. Xue, P.-H. Wang, S. Chen, A. J. Metcalf, J. Wang, D. E. Leaird, M. Qi, A. M. Weiner, “Investigation of mode coupling in normal dispersion silicon nitride microresonators for Kerr frequency comb generation”, *Optica*, **1**. 137-144(2014).

42. X. Xue, M. Qi, and A. M. Weiner, “Normal-dispersion microresonator Kerr frequency combs”, *Nanophotonics*, **5**, 244-262 (2016).

43. A. G. Griffith, R. K. W. Lau. J. Cardenas, Y. Okawachi, A. Mohanty, R. Fain, Y. H. D. Lee, M. Yu, C. T. Phare, C. B. Poitras, A. L. Gaeta, and M. Lipson, “Silicon-chip mid-infrared frequency comb generation”, *Nat. Commun*. **6**, 6229 (2015).

44. T. J. Kippenberg, R. Holzwarth, and S. A. Didadams, “Microresonator-based optical frequency combs”, *Science*, **332**, 555-559 (2010).

45. P. Trocha, M. Karpov, D. Ganin, M. H. P. Pfeiffer, A. Kordts, S. Wolf, J. Krockenberger, P. Martin-Palomo, C. Weimann, S. Randel, W. Freude, T. J. Kippenberg, and C. Koos, “Ultrafast optical ranging using microresonator soliton frequency combs”, *Science*, **359**, 887-891 (2018).

46. G. Lin, A. Coillet, and Y. K. Chembo, “Nonlinear photonics with high-Q whispering-galley-mode resonators”, *Adv. Opt. Photon*. **9**, 828-889 (2017).

47. J. Pfeifle, V. Brasch, M. Lauermann, Y. Yu, D. Wegner, T. Herr, K. Hartinger, P. Schindler, J. Li, D. Hillerkuss, R. Schmogrow, C. Weimann, R. Holzwarth, W. Freude, J. Leuthold, T. J. Kippenberg, and C. Koos, “Coherent terabit communications with microresonator Kerr frequency combs”, *Nat. Photon*. **8**, 375-380 (2014).

48. D. T. Spencer, T. Drake, T. C. Briles, J. Stone, L. C. Sinclair, C. Frederik, Q. Li, D. Westly, B. R. Ilic, A. Bluestone, N. Volet, T. Komljenvic, L. Chang, S. H. Lee, D. Y. Oh, M.-G., Suh, K. Y. Yang, M. H. P. Pfeiffer, T. J. Kippenberg, E. Norberg, L. Theogarajan, K. Vahala, N. R. Newbury, K. Srinvasan, J. E. Bowers, S. A. Diddams, and S. B. Papp, "An optical-frequency synthesizer using integrated photonics", *Nature*, **557** 81-85 (2018).

49. B. P. -P. Kuo, E. Myslivets, V. Ataie, E. G. Temprana, N. Alic, and S. Radic, "Wideband parametric frequency comb as coherent optical carrier", *J. Light. Technol*, **31**, 3414-3419 (2013).

50. J. Leuthold, C.Koos, and W. Freude, "Nonlinear silicon photonics", *Nat. Photon*. **4**. 535-544 (2010).

51. A. G. Griffith, R. K. W. Lau. J. Cardenas, Y. Okawachi, A. Mohanty, R. Fain, Y. H. D. Lee, M. Yu, C. T. Phare, C. B. Poitras, A. L. Gaeta, and M. Lipson, "Silicon-chip mid-infrared frequency comb generation", *Nat. Commun*. **6**, 6229 (2015).

52. M. Yu, Y. Okawachi, A. G. Griffith, M. Lipson, and A. L. Gaeta, "Mode-locked mid-infrared frequency combs in a silicon microresonator", *Optica*. **3**, 854-860 (2016).

53. I. Demirtzioglou, C. Lacava, K. R. H. Bottrill, D. J. Thomson, G. T. Reed, D. J. Richardson, and P. Petropoulos, "Frequency comb generation in a silicon ring resonator modulator", *Opt. Lett*. **26**, 790-797 (2018).

54. J. Yu, Z. Dong, J. Zhang, X. Xiao, H.-C. Chien, and N. Chi, "Generation of coherent and frequency-locked multi-carriers using cascaded phase modulators for 10 Tb/s optical transmission system", *J. Light. Technol*. **30**, 458-465 (2012).

55. A. Gajda, L. Zimmermann, J. Bruns, B. Tillack, and K. Petermann, "Design rules for p-i-n diode carriers sweeping in nano-rib waveguides on SOI", *Opt. Exp*. **19**, 9915-9922 (2011).

56. V. Ataie, E. Myslivets, B. P.-P. Kuo, N. Alic, and S. Radic, "Spectrally equalized frequency comb generation in multistage parametric mixer with nonlinear pulse shaping", *J. Light. Technol*. **32**, 840-846 (2014).

57. P. P. Kuo and S. Radic, "Generation of ultra-low noise optical parametric combs", *Proc. SPIE*, **9731** 9731-1 – 9731-9 (2016).

58. T. Herr, K. Hartinger, J. Riemensberger, C. Y. Wang, E. Gavartin, R. Holzwarth, M. L. Gorodetsly, and T. J. Kippenberg, "Universal formation dynamics and

noise of Kerr-frequency combs in microresonators", *Nat. Photon*. **6**, 480-487 (2011).

59. Y. Okawachi, M. Yu, K. Luke, D. O. Carvalho, S. Ramelow, A. Farsi, M. Lipson, and A. L. Gaeta, "Dual-pumped degenerate Kerr oscillator in a ring silicon nitride microresonator, *Opt. Lett*. **22**, 5267-5270 (2015).

60. C. Bao, P. Liao, A. Kordts, L. Zhang, M. Karpov, M. H. P. Pfeiffer, Y. Cao, Y. Yan, A. Almaiman, G. Xie, A. Mohaherin-Ariaei, L. Li, M. Ziyadi, S. R. Wilkinson, M. Tur, T. J. Kippenberg, and A. E. Willner, "Dual-pump generation of high-coherence primary Kerr combs with multiple sub-lines", *Opt. Lett*. **42**. 595-598 (2017).

61. W. Wang, S. T. Chu, B. E. Little, A. Pasquazi, Y. Wang, L. Wang, W. Zhang, L. Wang, X. Hu, G. Wang, H. Hu, Y. Su, F. Li, Y. Liu, and W. Zhao, "Dual-pump Kerr micro-cavity optical frequency comb with varying FSR spacing", *Sci. Rep*. **6**. 28501 (2016).

62. H. K. Tang, C. S. Wong, T. K. Liang, I. E. Day, S. W. Robberts, A. Harpin, J. Drake, and M. Asghari, "Optical dispersion, two-photon, absorption and self-phase modulation in silicon waveguides at 1.5μm wavelength", *Appl. Phys. Lett*. **80**(3), 416-418 (2002).

63. A. C. Foster, C. Manolatou, B. S. Schmidt, M. Lipson, M. A. Foster, J. E. Sharping and A. Gaeta, "Tailored anormalous group-velocity dispersion in silicon channel waveguide", *Opt. Exp*. **14**(10), 4357-4362 (2006).

64. P. Merritt, R. P. Tatam, and D.A. Jackson, "Interferometric chromatic dispersion measurements on short lengths of monomode optical fiber", *J. Light. Technol*, **7**(4), 703-716 (1989).

65. J. M. Chavez Boggio, D. Bodenmüller, T. Fremberg, R. Haynes, M. M. Roth, R. Eisermann, M. Lisher, L. Zimmermann, and M. Böhm, "Dispersion engineered silicon nitride waveguides by geometrical and refractive-index optimization", *J. Opt. Soc. Am*. B **31**(11), 2846-2857 (2014).

66. C. Baker, Y. Lu, and X. Bao, "Chromatic-dispersion measurement by modulation phase-shift method using a Kerr phase interferometer", *Opt. Exp*. **22**(19), 22314-22319 (2014).

67. M. A. Galle, W. Mohammed, L. Qian, and P. W. E. Smith, "Single-arm three-wave interferometer for measuring dispersion of short lengths of fiber", *Opt. Exp*. **15**(25), 16896-16908 (2007).

68. R. Marchetti, V. Vitali, C. Lacava, I. Cristiani, B. Charbonnier, V. Muffato, M. Fournier, and P. Minzioni, “Group-velocity dispersion in SOI-based channel waveguides with reduced-height”, *Opt. Exp*. **25**(9), 9761-9767 (2017).

69. A. S. Raja, A. S. Voloshin, H. Guo, S. E. Agafonova, J. Liu, A. S. Gorodnitskiy, M. Karpov, N. G. Pavlov, E. Lucas, R. R. Galiev, A. E. Shitkov, J. D. Jost, M. L. Gorodetsky, and T. J. Kippenberg, “Electrically pumped photonic integrated soliton microcomb”, *Nat. Commn*. **10**. 680 (2019).

70. E. Dulkeith, F. Xia, L. Schares, W. M. J. Green, and Y. A. Vlasov, “Group index and group velocity dispersion in silicon-on-insulator photonic wires”, *Opt. Exp*. **14**(9), 3853-3863 (2006).

71. J. Y. Lee and D.Y. Kim, “Versatile chromatic dispersion measurement of a single mode fiber using spectral white interferometry”, *Opt. Exp*. **14**(24), 11608-11615 (2006).

72. F. Leo, U. Dave, S. Keyvaninia, B. Kuyken, and G. Roelkens, “Measurement and tuning of the chromatic dispersion of a silicon photonic wire around the half band gap spectral region”, *Opt. Lett*. **39**(3), 711-714 (2014).

73. D. W. Kim, S. H. Kim, S. H. Lee, K. H. Kim, J-M. Lee, and E-H. Lee, “A new method of measuring localized chromatic dispersion of structured nanowaveguide devices using white-light interferometry”, *J. Light. Technol*. **30**(1), 43-48 (2012).

74. S. Mas, J. Matres, J. Marti, and C. J. Oton, “Accurate chromatic dispersion characterization of photonic integrated circuits”, *IEEE. Photonics J*. **4**(3), 825-831 (2012).

75. S. D. Dyer, K. B. Rochford, and A. H. Rose, “Fast and accurate low-coherence interferometric measurements of fiber Bragg grating dispersion and reflectance”, *Opt. Exp*. **5**(11), 262-266 (1999).

76. S. Moon, and Z. Chen, “Phase-stability optimization of swept-source optical coherence tomography”, Biomed. *Opt. Exp,* **9**(11), 5280-5295 (2018).

77. J. Xi, L. Huo, J. Li, and X. Li, “Generic real-time uniform K-space sampling method for high-speed swept-Source optical coherence tomography”, *Opt. Exp*. **18**(9) 9511-9517 (2010).

78. S. H. Lee, S. H. Kim, K. H. Kim, M. H. Lee, and E.-H. Lee, “A novel method for measuring continuous dispersion spectrum of electro-optic coefficients of nonlinear materials”, *Opt. Exp*. **17**(12), 9828-9833 (2012).

79. G.F.R. Chen, J.R. Ong, T.Y.L. Ang, S.T. Lim, C. E. Png, and D.T.H. Tan, "Broadband Silicon-On-Insulator directional couplers using a combination of straight and curved waveguide sections". *Sci Rep* **7,** 7246 (2017).

80. T. Herr, K. Hartinger, J. Riemensberger, C. Y. Wang, E. Gavartin, R. Holzwarth, M. L. Gorodetsky, and T. J. Kippenberg, "Universal formation dynamics and noise of Kerr-frequency combs in microresonators". *Nature Photon* **6,** 480–487 (2012).

81. L. Mercade, L. L. Martin, A. Griol, D. Navarro-Uris, and A. Martines, "Microwave oscillator and frequency comb in a silicon optmechanical cavity with a full photonic bandgap" *Nanophotonics*, **9**(11), 3535-3544 (2020).

82. X. Xue, and A. M. Weiner, "Microwave photonics connected with microresonator frequency combs" *Front. Optelectron*, **9**(2), 238-248 (2016).

83. Liang, W., Eliyahu, D., Ilchenko, A. A. Savchenkov, A. B. Matsko, D. Seidel, and L. Maleki, "High spectral purity Kerr frequency comb radio frequency photonic oscillator". *Nat Commun* **6,** 7957 (2015).

84. T. Okoshi, K. Kikuchi, and A. Nakayama, "Novel method for high resolution measurement of laser output spectrum", *Electron. Lett*. **16**, 630(1980).

85. H. Ludvigsen, M. Tossavainen, and M. Kaivola, "Laser linewidth measurements using self-homodyne detection with short delay", *Opt. Commn,* **155** 180-186 (1998).

86. P. Del'Haye, T. Herr, E. Gavartin, M. L. Gorodetsky, R. Holzwarth, and T. J. Kippenberg, "Octave spanning tunable frequency comb from a microresonator", *Phys. Rev. Lett.* **107**, 063901 (2011).

87. V. B. Braginsky, M. L. Gorodetsky, and S. P. Vyatchanin, "Thermodynamical fluctuations and photo-thermal shot nise in gravitational wave antennae", *J. Opt. Soc. Am.* B **22**, 459 (2005).

88. A.Demir,A.Mehrotra,andJ.Roychowdhury, "Phasenoiseinoscillators: aunifying theory and numerical methods for characterization," *IEEE Trans. Circuits Syst. I*, Fundam. Theory Appl., vol. **47**, no. 5, pp. 655–674, (2000).

89. S. Tallur, S. Sridaran, and S. A. Bhave, "A monolithic radiation-pressure driven, low phase noise silicon nitride opto-mechanical oscillator," *Opt. Express*, vol. **19**, no. 24, pp. 24522–24529, (2011).

90. J. Li, H. Lee, and K. J. Vahala, "Microwave synthesizer using an on-chip Brillouin oscillator," *Nat. Commun.*, vol. **4**, no. 1, p. 2097, (2013).

91. I. Ghorbel, R. Zhu, D. Dolfi, G. Lehoucq, A. Martin, G. Moille, L. Morvan, R. Braive, S. Combrie, and A. D. Rossi, "Optomechanical gigahertz oscillator made of a two photon absorption free piezoelectric III/V semiconductor," *APL Photon*., vol. **4**, no. 11, p. 116103, (2019).

92. L. Lundberg, M. Mazur, A. Mirani, B. Foo, J. Schroöder, V. T.-Company, M. Karlsson, and P. A. Andrekson, "Phase-coherent lightwave communications with frequency combs" *Nat Commun* **11,** 201 (2020).

93. M. R. Khanzadi, "Phase noise in communication systems Modeling, compensation, and performance analysis", PhD Thesis, Chalmars University of Technology (2015).

94. B. P.-P. Kuo, E. Myslivets, N. Alic, S. Radic, "Wavelength Multicasting via Frequency Comb Generation in a Bandwidth-Enhanced Fiber Optical Parametric Mixer", *J. Light. Technol*. **29**(23), 3515-3522 (2011).

95. A. Gaeta, M. Lipson, and T. J. Kippenberg, "Photonic-chip-based frequency combs", *Nature Photon* **13,** 158–169 (2019).

96. K.Y. Yang, D.Y. Oh, S.H. Lee, Q.-F. Yang, X. Yi, B. Shen, H. Wang, and K. Vahala, "Bridging ultrahigh-*Q* devices and photonic circuits". *Nature Photon* **12,** 297–302 (2018).

97. N. Singh, M. Xin, N. Li, D. Vermeulen, A. Ruocco, E. S. Magden, K. Shtyrkova, E. Ippen, F. X. Kartner, and M. Watts, "Silicon photonics optical frequency synthesizer", *Laser Photonics Rev*. **14**, 1900449 (2020).

98. D.T. Spencer, T. Drake, T.C. Briles, J. Stone, L. C. Sinclair, C. Fredrick, Q. Li, D. Westly, B. R. Ilic, A. Bluestone, N. Volet, T. Komljenovic, L. Chang, S. H. Lee, D. Y. Oh, M.-G. Suh, K. Y. Tang, M. H. P. Pfeiffer, T. J. Kippenberg, E. Norberg, L. Theogarajan, K. Vahala, N. R. Newbury, K. Srinivasan, J. E. Bowers, S. A. Diddams, and S. B. Papp, "An optical-frequency synthesizer using integrated photonics". *Nature* **557,** 81–85 (2018).

99. B. Shen, L. Chang, J. Liu, H. Wang, Q.-F. Yang, C. Xiang, R. N. Wang, J. He, T. Liu, W. Xie, J. Guo, D. Kinghorn, L. Wu, Q.-X., Ji, T. J. Kippenberg, K. Vahala, and J. E. Bowers "Integrated turnkey soliton microcombs", *Nature*, **582**, 365-369 (2020).

100. B. Stern, X. Ji, Y. Okawachi, A. L. Gaeta, and M. Lipson, "Battery-operated integrated frequency comb generator". *Nature* **562**, 401–405 (2018).

101. A. S., Raja, A. S. Voloshin, H. Guo, S. E. Agafonova, J. Liu, A. S. Gorodnitsky, M. Karpov, N. G. Pavlov, E. Lucas, R. R. Galiev, A. E. Shitikov, J. D. Jost, M. L. Gorodetsky, and T. J. Kippenberg, “Electrically pumped photonic integrated soliton microcomb”. *Nat. Commun.* **10**, 680 (2019); correction **10**, 1623 (2019).